Radio Galaxies as the Origin of Ultra-High-Energy Cosmic Rays

[1]Jeongbhin Seo, [1]Dongsu Ryu , and [2]Hyesung Kang

[1]Department of Physics, College of Natural Sciences, UNIST, Ulsan 44919, Republic of Korea

[2]Department of Earth Sciences, Pusan National University, Busan 46241, Republic of Korea

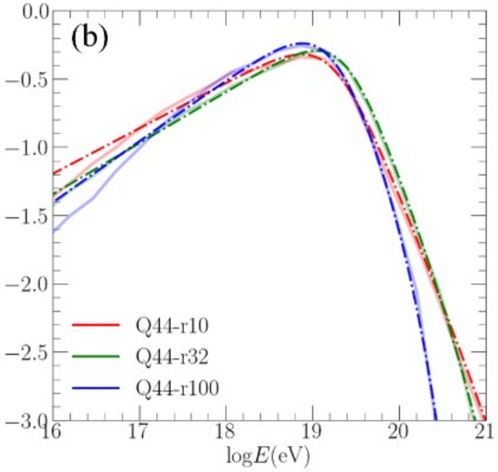

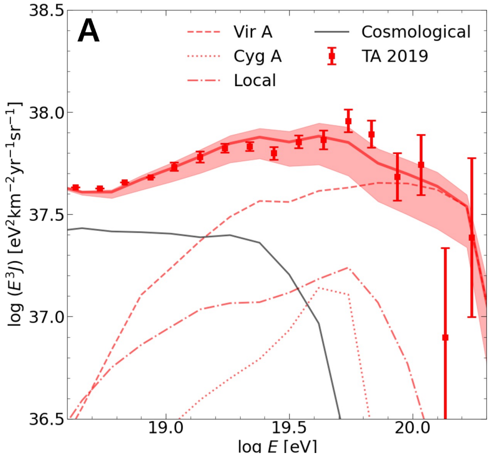

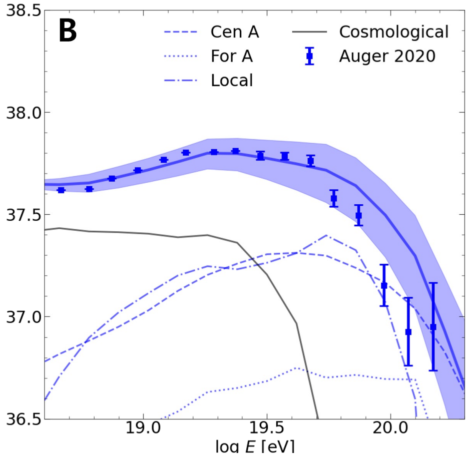

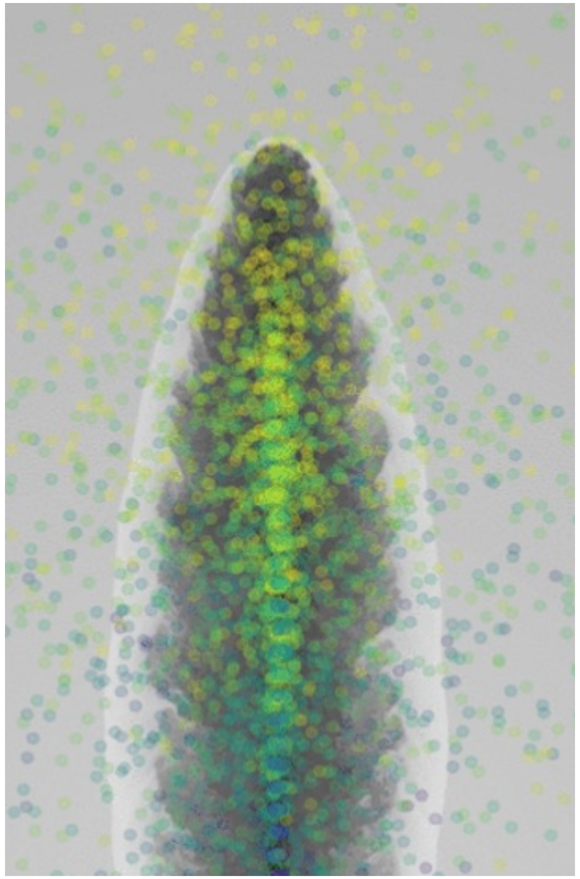

Observation of ultra-high energy cosmic rays (UHECRs)

Flux

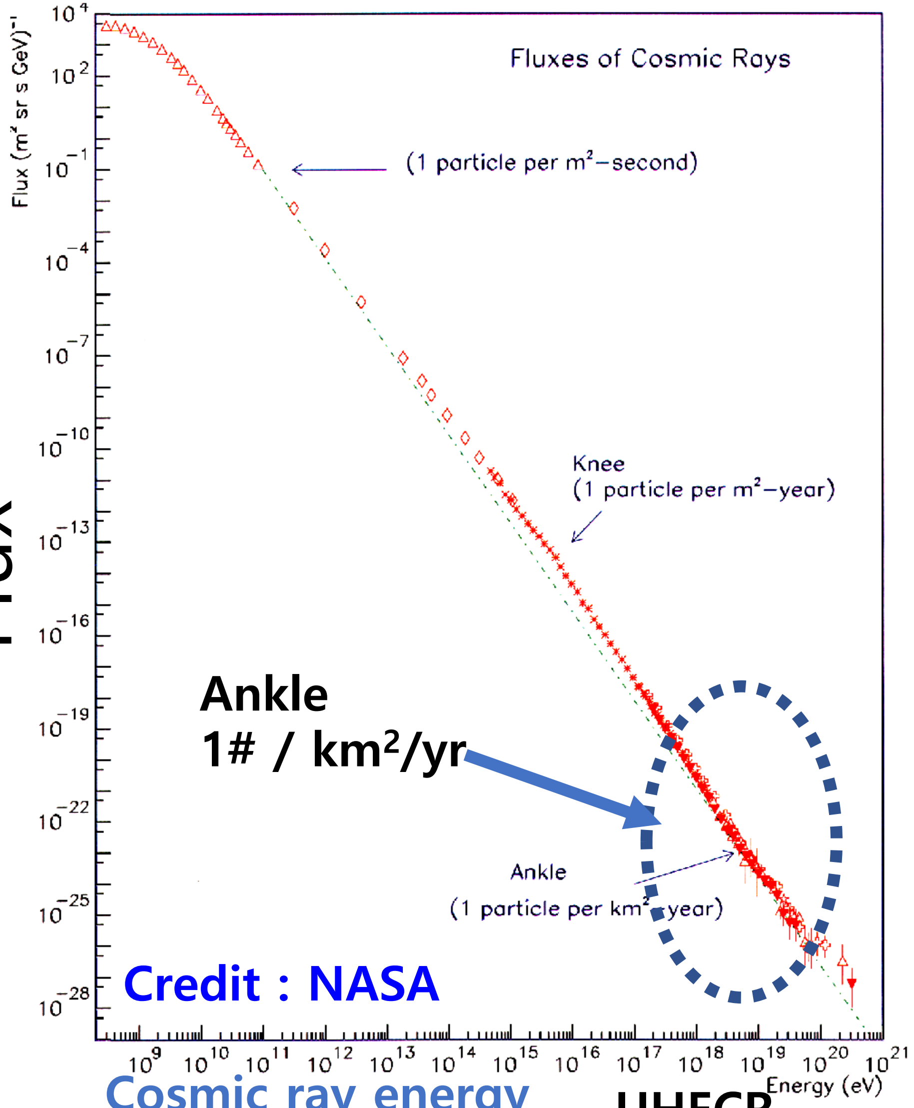

Ankle
1# / km²/yr

Credit : NASA

Cosmic ray energy spectrum

UHECR
$\geq 10^{18}$eV(EeV)

UHECRs observatories

Telescope Array

Pierre Auger observatory

Discrepancies in Auger and TA observations

Energy spectrum

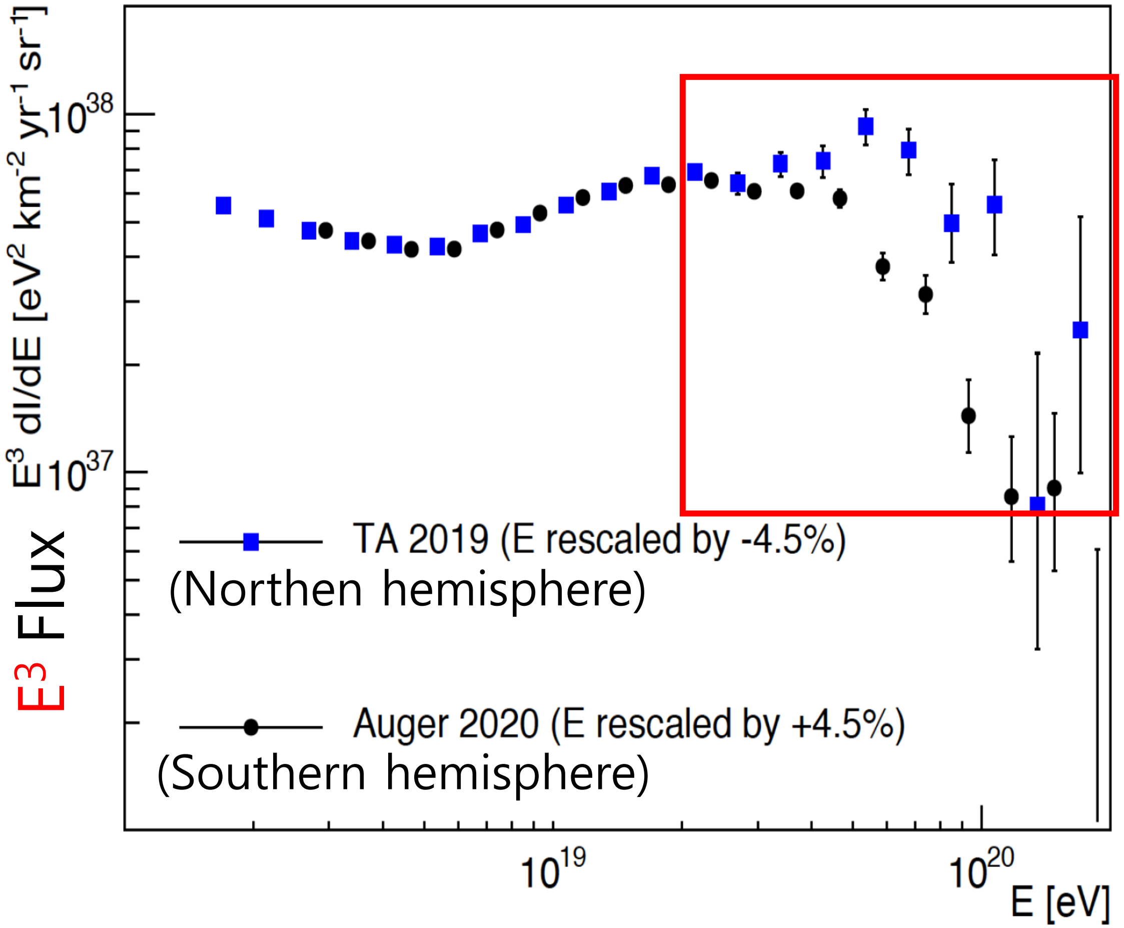

Tsunesada 2021 (ICRC 2021)

Mass Composition

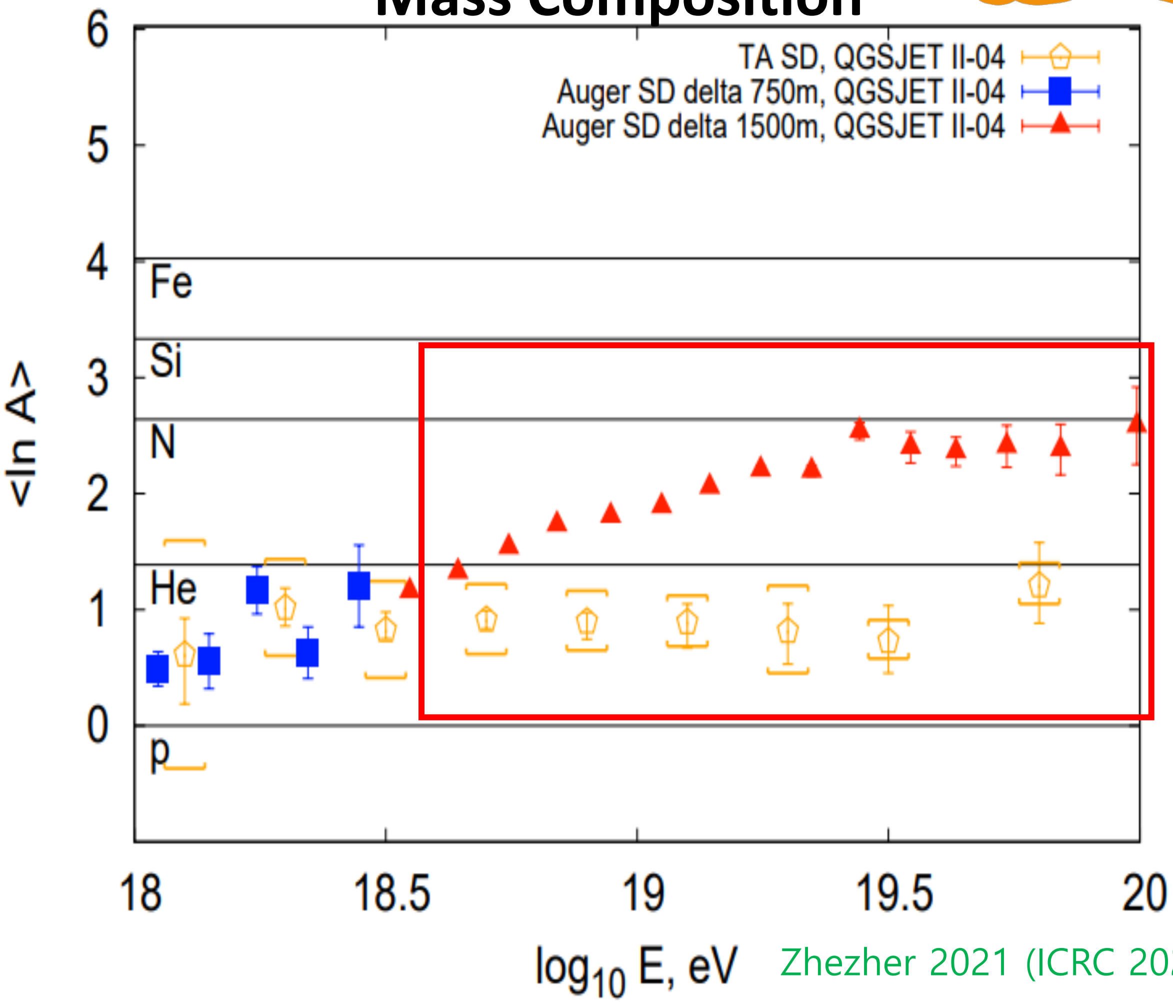

Zhezher 2021 (ICRC 2021)

Radio galaxies: possible astrophysical sources of UHECRs

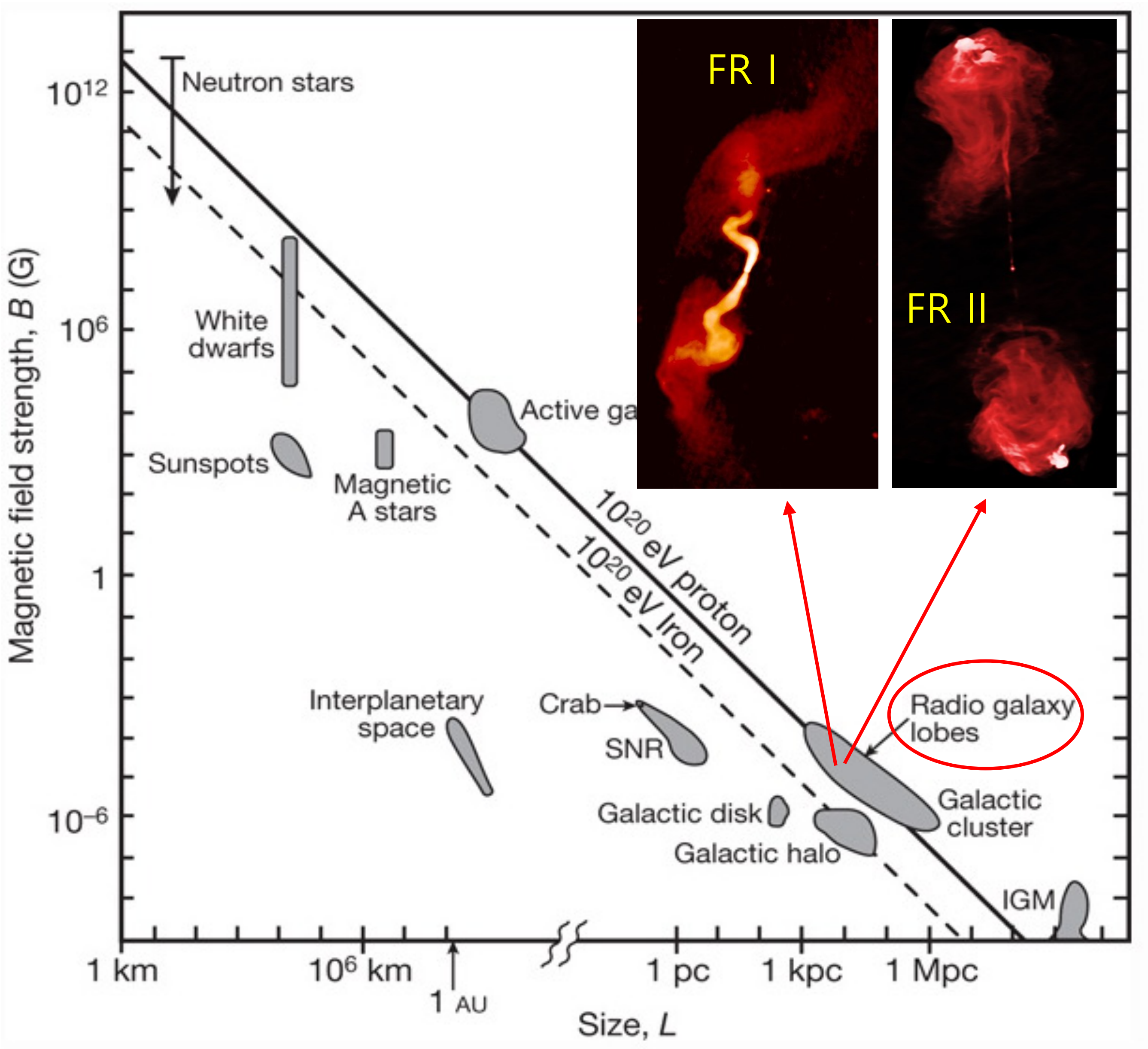

Confinement condition ← Hillas criteria

Particles should be confined within accelerator in order to be accelerated. $r_g \leq L$

$$E_{Hillas}(EeV) \leq \beta_a \cdot B_{\mu G} L_{kpc}$$ for proton

$$E_{Z_i,Hillas} = Z_i E_{Hillas}$$

Z_i charge $\quad \beta_a = V_a/c \quad B_{\mu G} = \frac{B}{1\mu G} \quad L_{kpc} = \frac{L}{1kpc}$

Radio Galaxies (RGs):

FR-I : mildly relativistic jet, two-sided, plume-like

FR-II : highly relativistic jet, brighter lobed (hot spot), often one-sided (relativistic beaming)

Most promising candidate for UHECR sources ?

(Blandford et al. 2019; Rieger 2019; Hardcastle & Croston 2020; Matthews et al. 2020, + many previous studies)

Radio galaxy jets: Lorentz factor ~ 1-10 for 1~100kpc jets, B~10-100μG

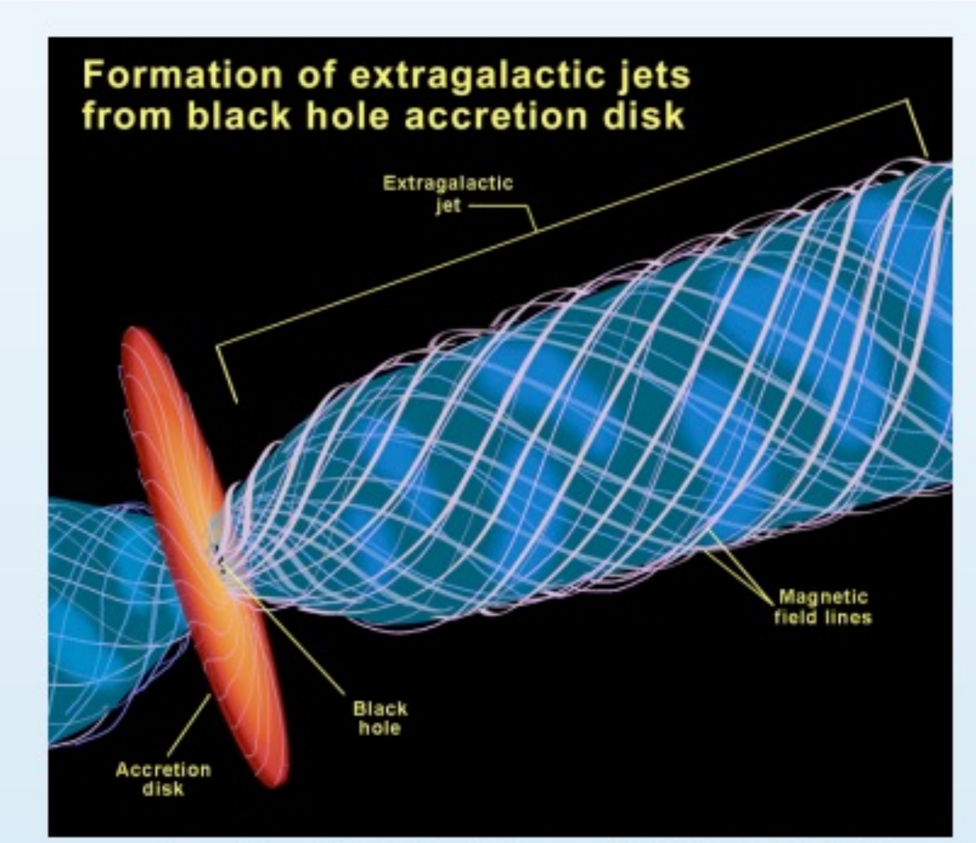

Credit: NASA / Ann Field (STScI)

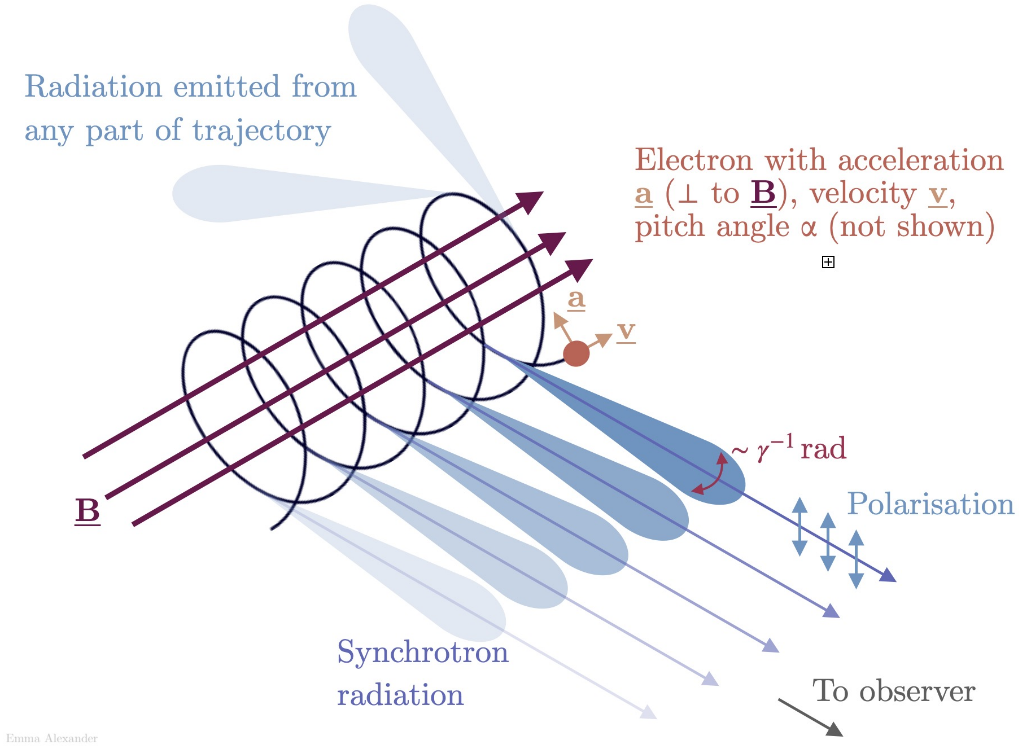

Radio jets emit strong radio due to synchrotron radiation from cosmic ray (non-thermal) electrons.

Morphological Dichotomy of Jets: Fanaroff-Riley Classification

FR-I : center bright

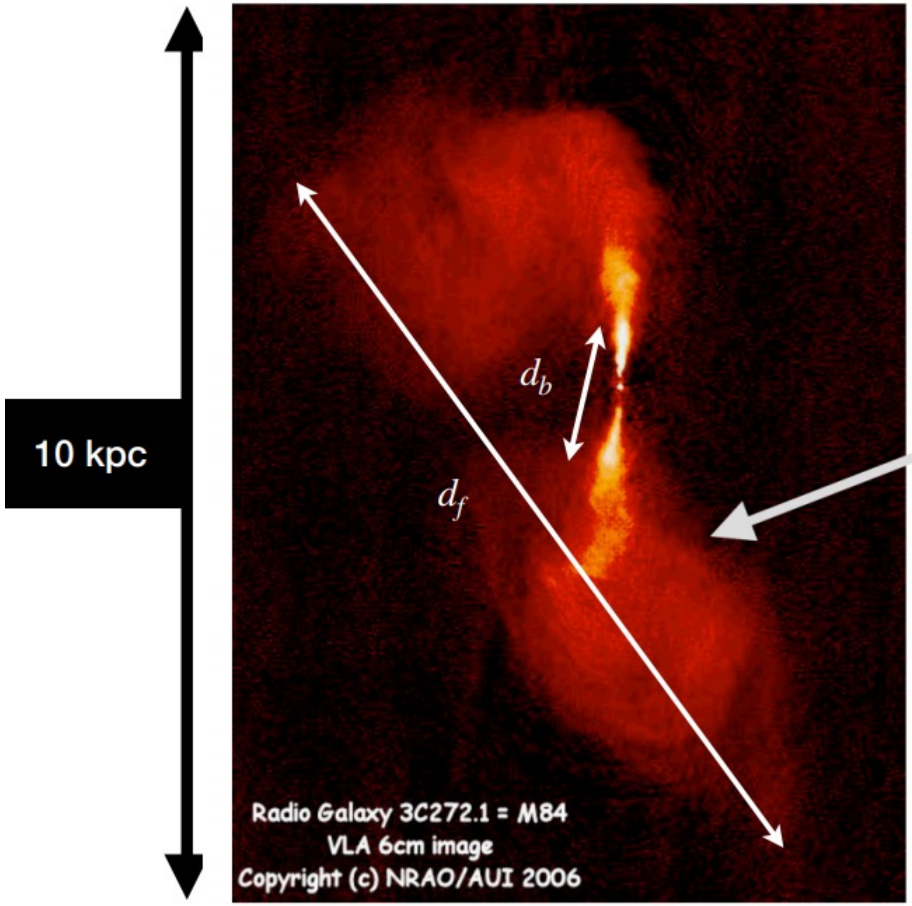

$$\frac{d_b}{d_f} < 0.5, \text{FR-I}$$

FR-II : edge bright

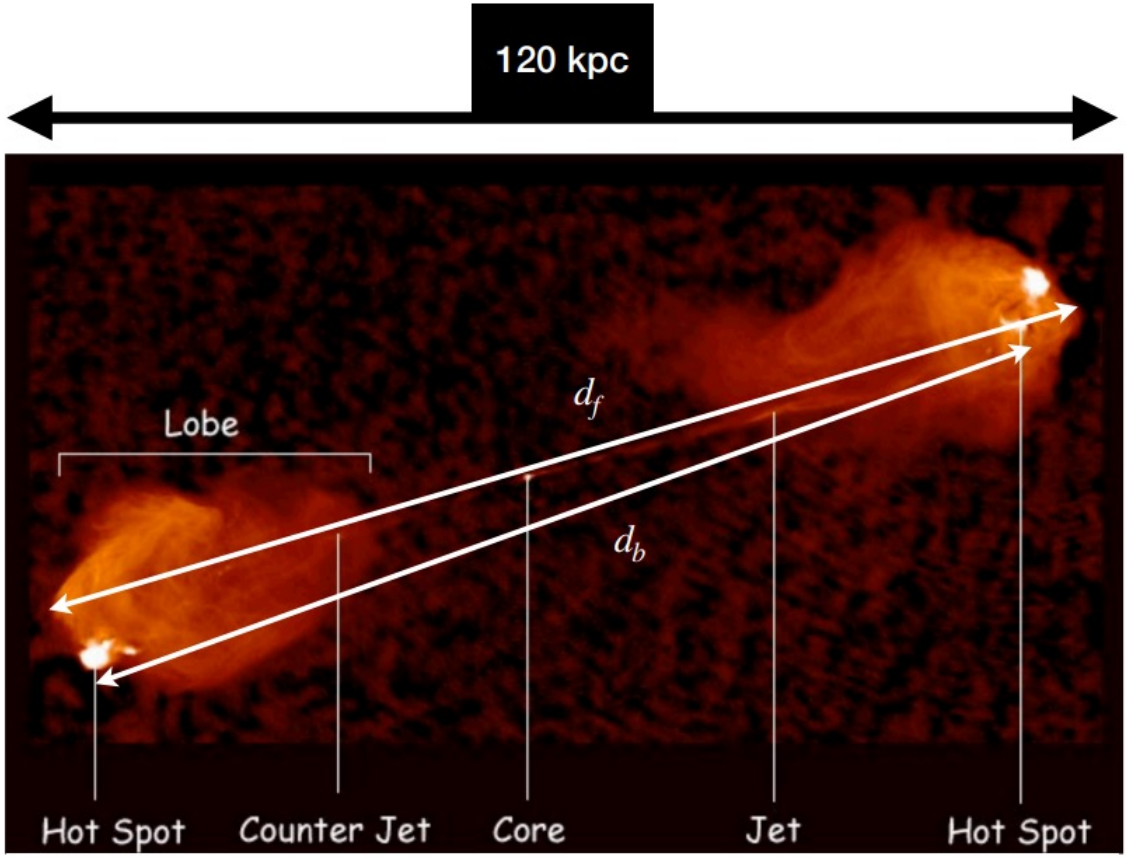

Radio galaxy **Cygnus A** at 5 GHz , d ~ 220 Mpc, (z=0.056), extension ~120 kpc (credits: NRAO/AUI, A. Bridle)

$$\frac{d_b}{d_f} > 0.5, \text{FR-II}$$

Image Credits: Frank M. Reiger

Various shape of radio jets

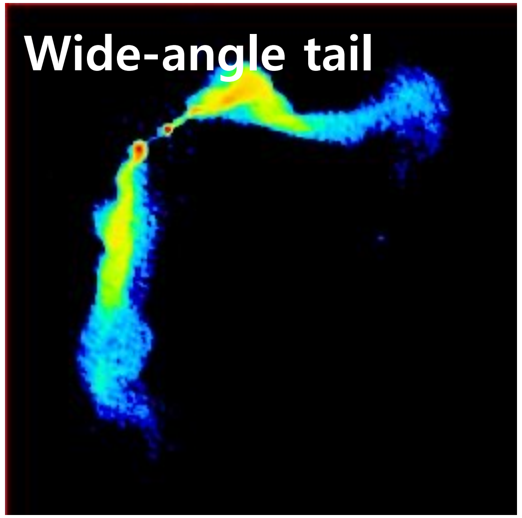

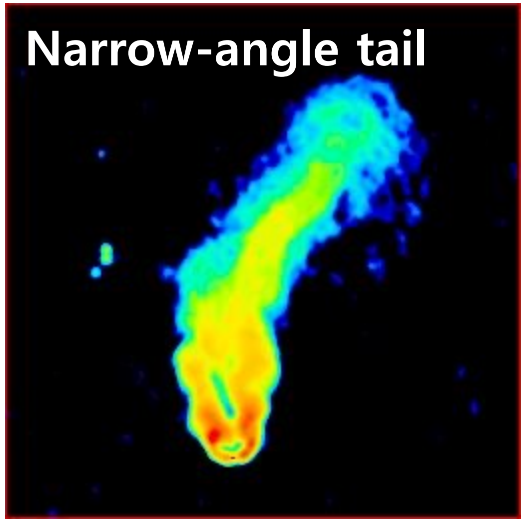

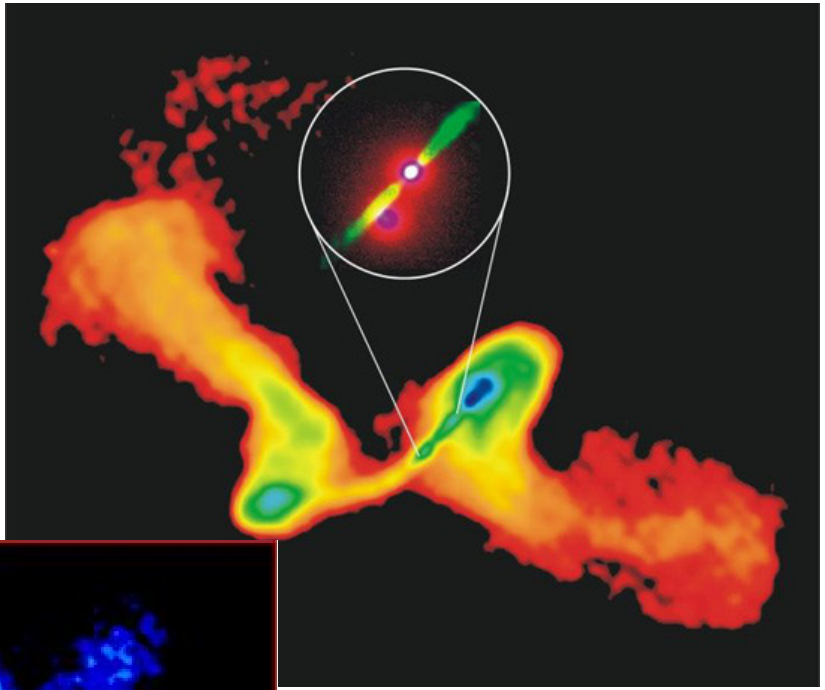

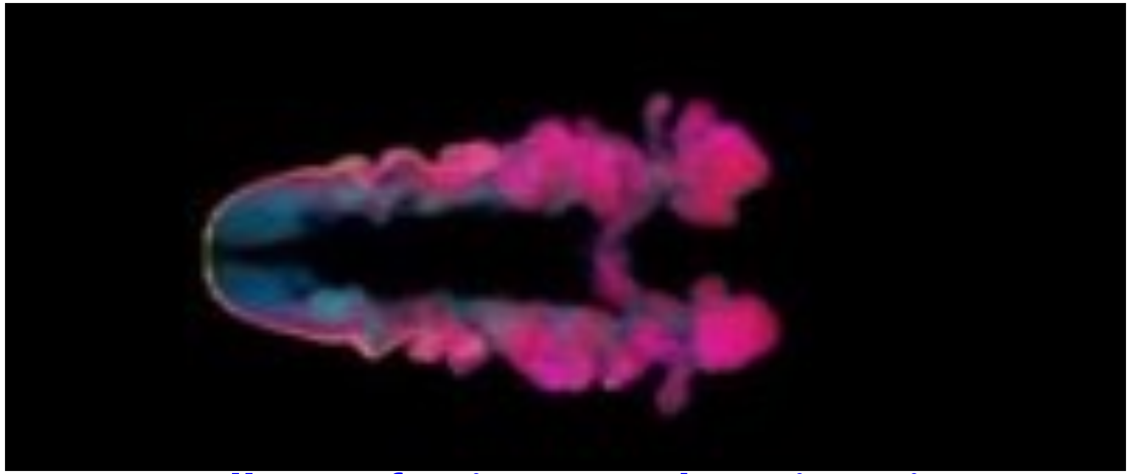

College of Science and Engineering, UMN

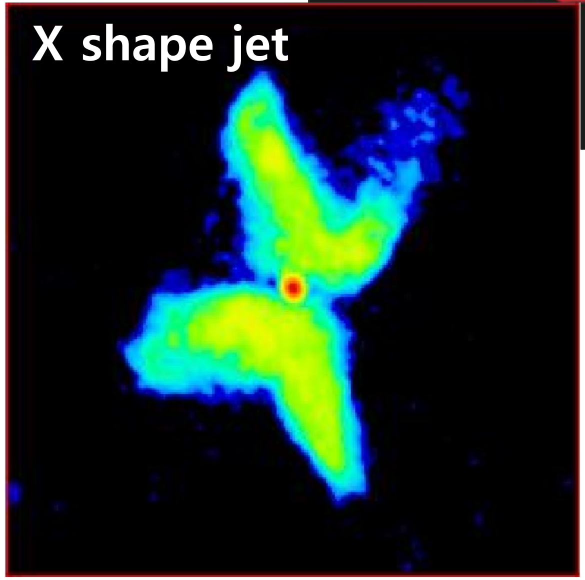

interaction with an intracluster medium?
large precession angle?

Interaction between radio relic and radio jet

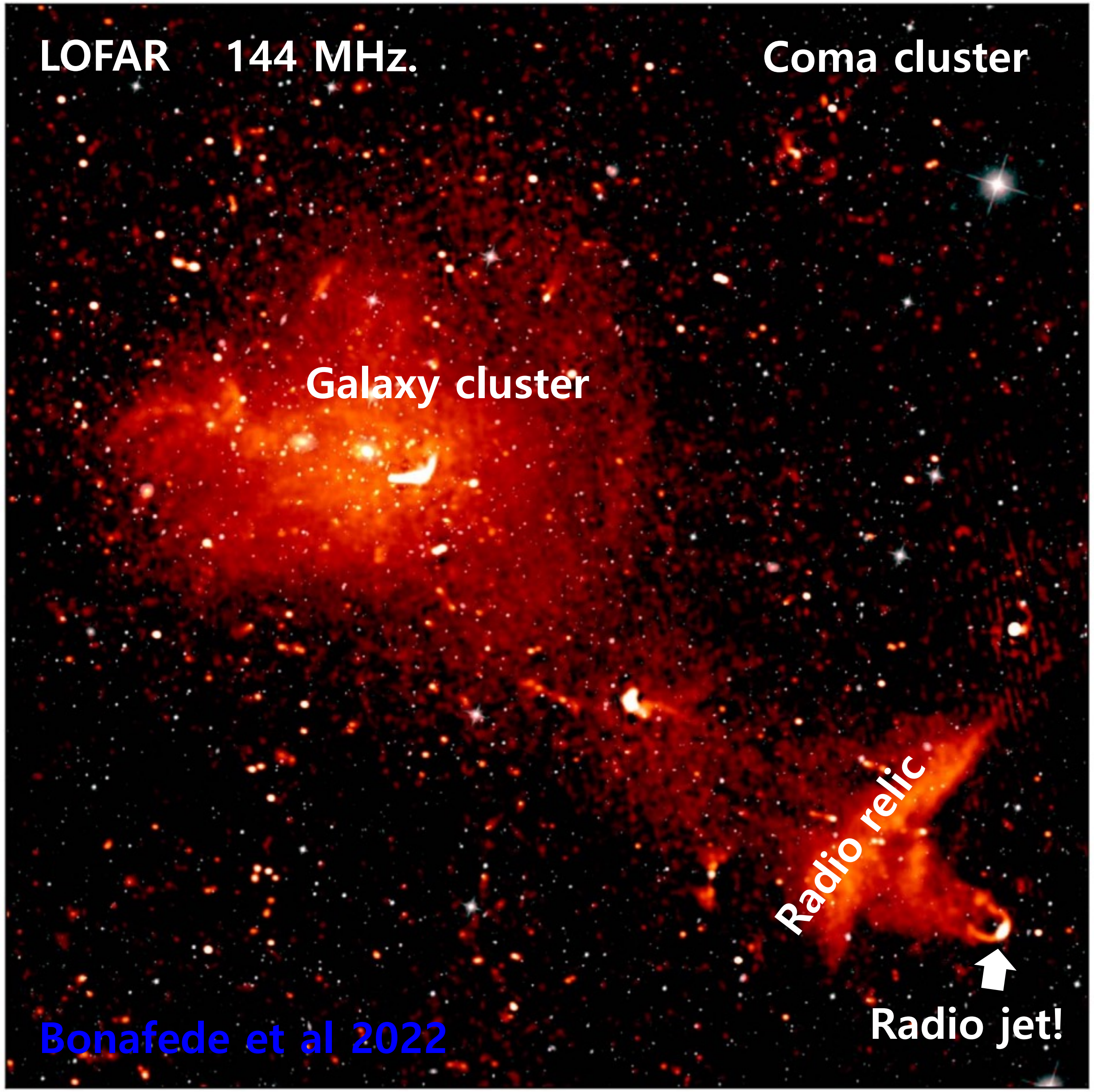

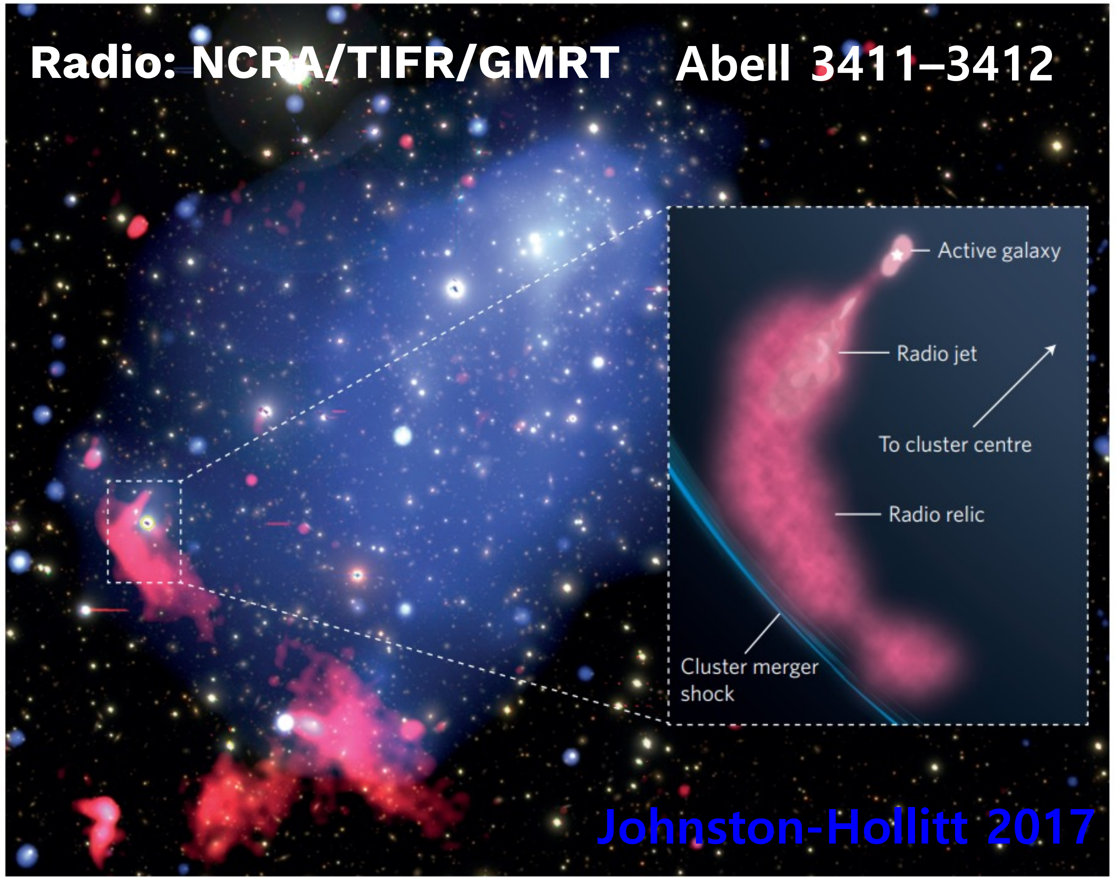

Radio jets will play important role in radiation, and dynamics in ICM environment

Previous study of the UHECRs acceleration in Radio galaxy jet

Matthews et al 2019

- **Diffusive shock acceleration**
- Performed **RHD** simulation (PLUTO code)
- **Hillas energy** of the backflow shocks is presented (~10^{19}eV for proton)
- **Figure :** Shock surface they found, within the jet (cyan), within backflow (orange)

Kimura et al 2018 &
Ostrowski et al 1998

- **Discrete shear acceleration**
- Performed **Monte-Carlo** simulations with simple cylindrical configuration
- **Energy spectrum** of accelerated particles is presented
- **Figure :** schematic picture of shear acceleration in a jet- cocoon system of an AGN.

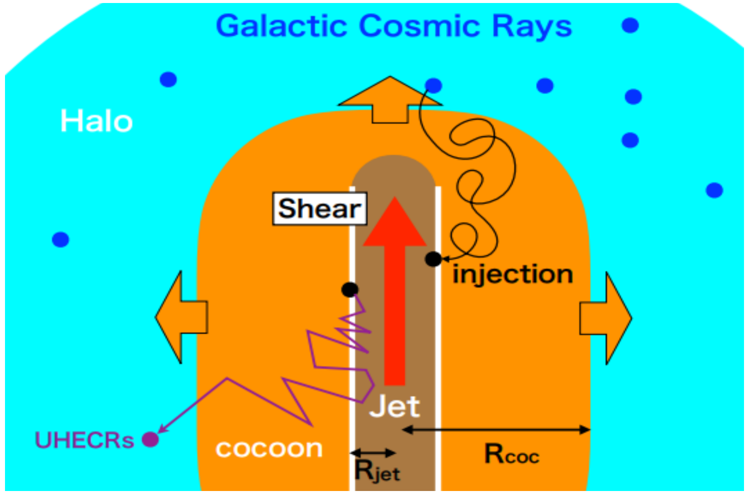

Caprioli 2018 &
Mbarek et al 2019, 2021

- **"expresso" acceleration**
- Performed **Monte-Carlo** simulations using simulated MHD jet configuration
- **Energy spectrum** of acceleration particle is presented
- **Figure :** Schematic trajectory of a galactic CR reaccelerated by a relativistic jet

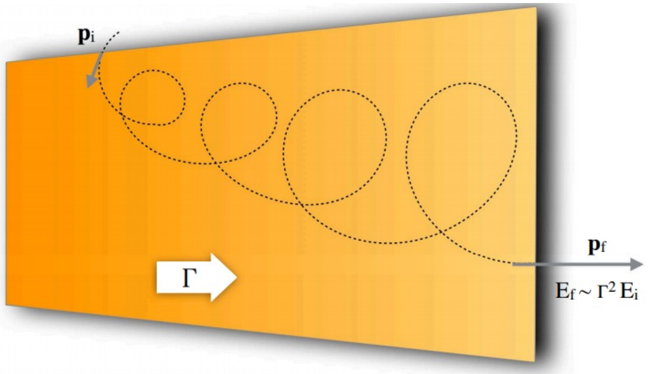

Flow chart of this study

Title of the study

Development of a new code for Relativistic Hydrodynamics (RHD)

Simulations of jets: Structures and Dynamics

Monte Carlo Simulations for CR acceleration, using simulated jets

Main topic

- Develop high order RHD code
- 5^{th} order WENO + 4^{th} order SSPRK
- Adopt Realistic equation of state
- Perform various code test

- Perform RHD jet simulation
- Study parameter dependency of the morphology and energetics of the jet
- Analyze non-linear structures

- Develop Cosmic ray transport code
- Analyze the acceleration process that occurred inside the jets
- Present UHECRs spectrum accelerated through jets

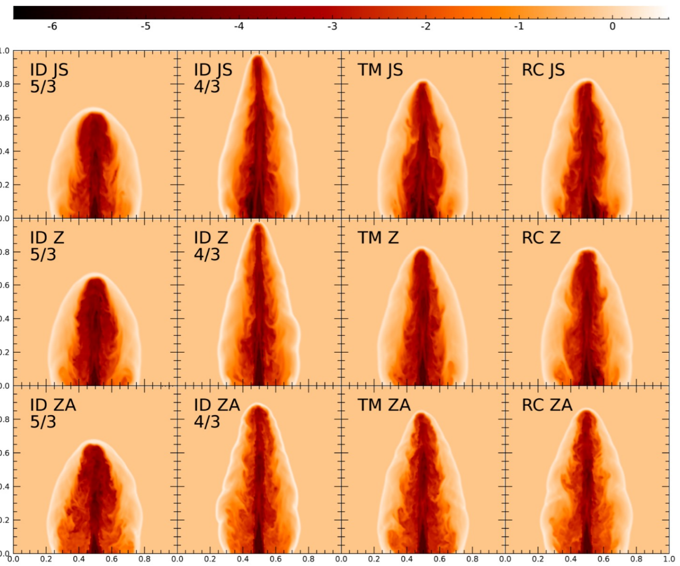

Developing Realistic and accurate RHD code

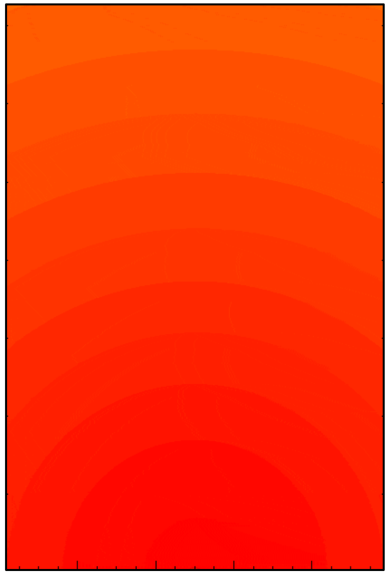

RHD jet simulation

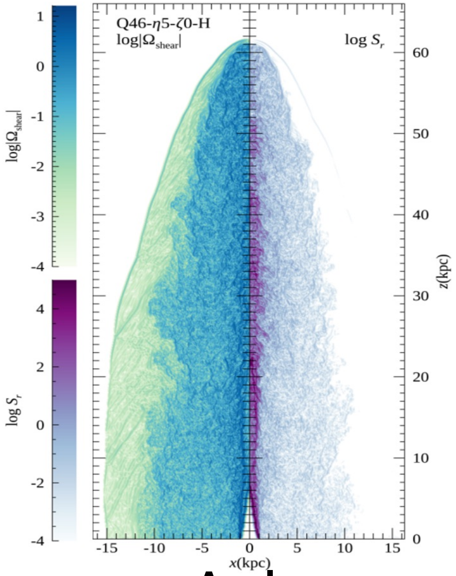

Analyze non-linear structures

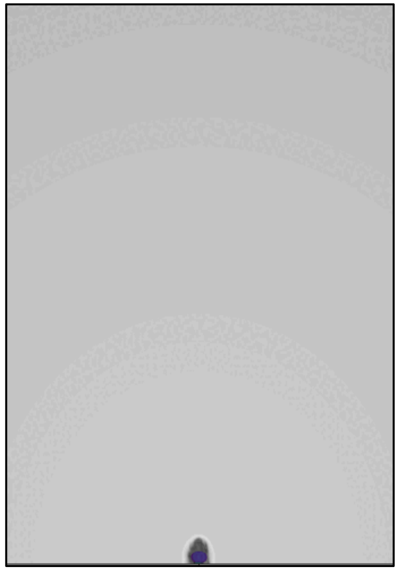

Monte-Carlo simulation

Structures generated in the jet-induced flow

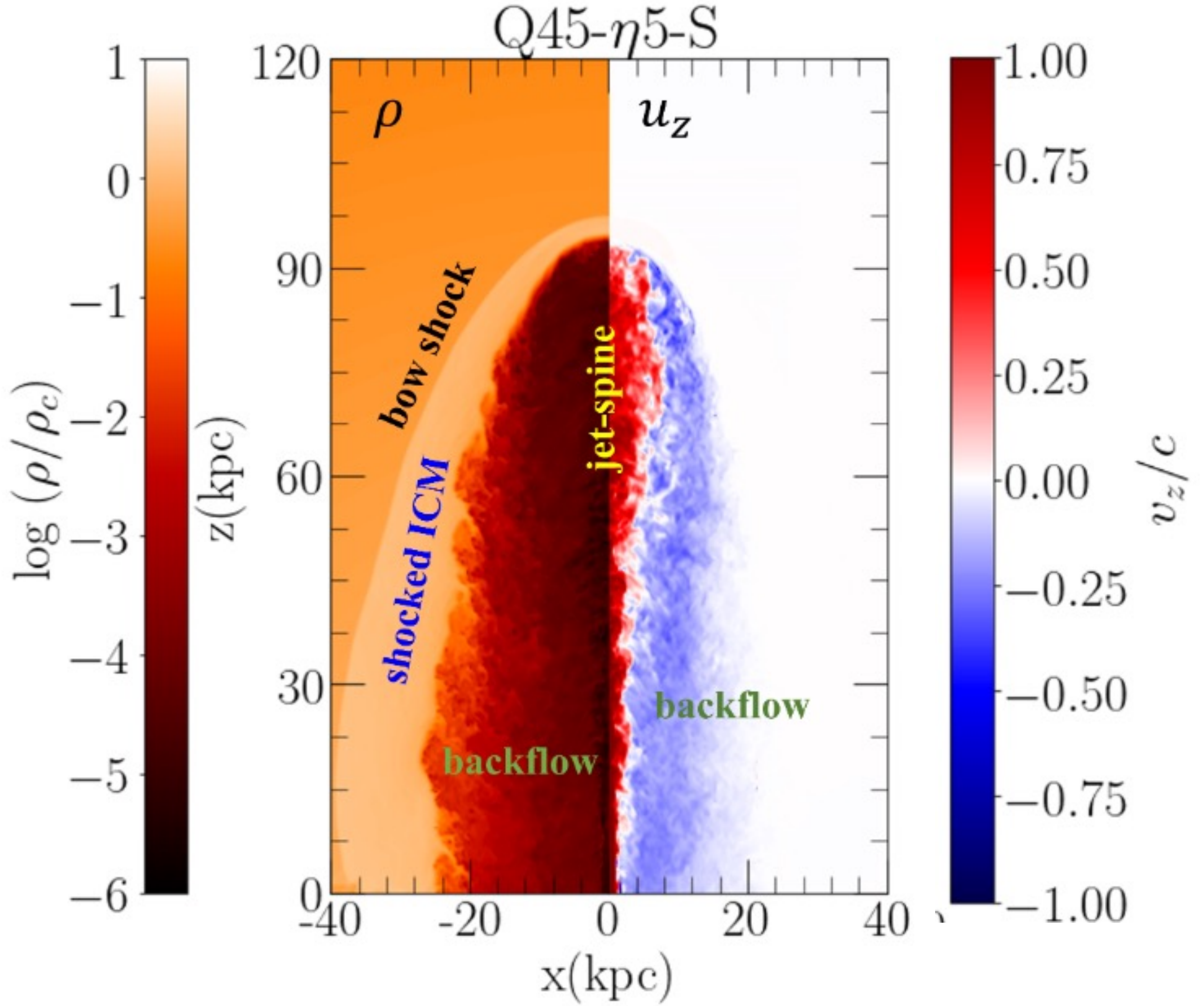

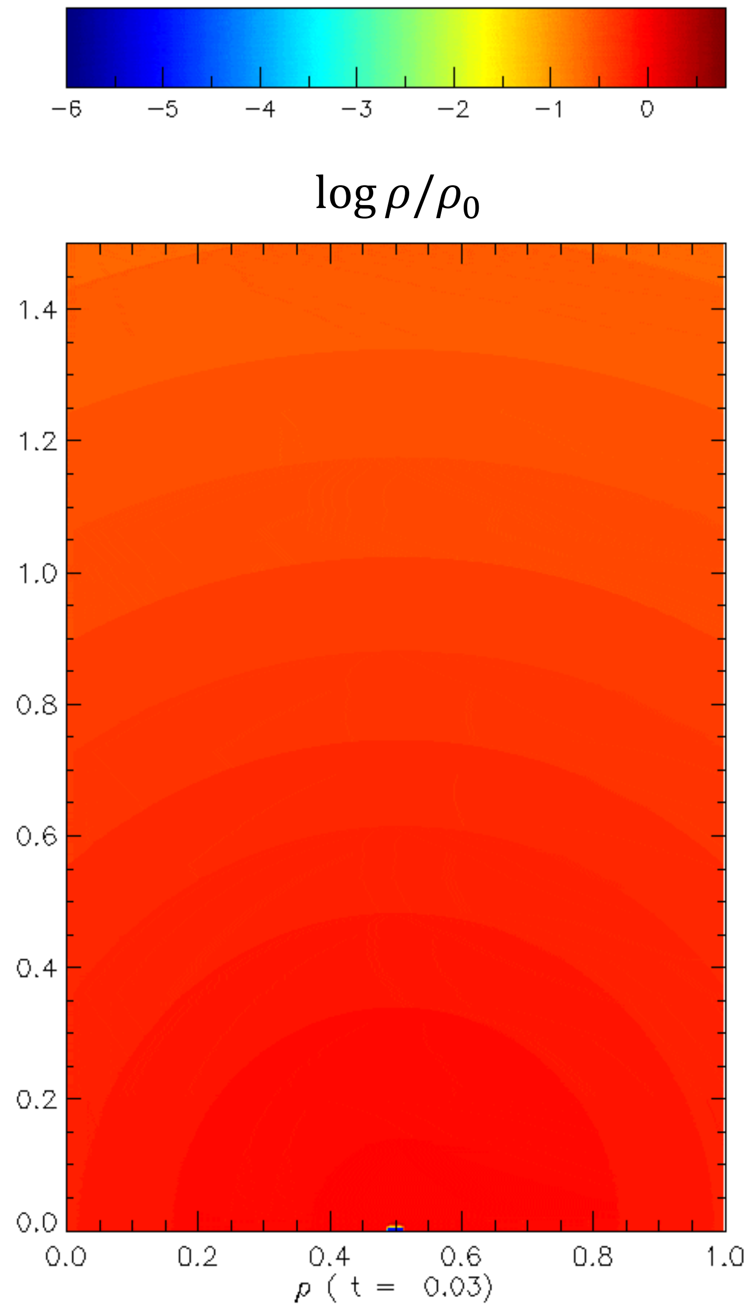

The jet is halted at the **termination shock**, while the backflow forms a **cocoon/lobe** that encompasses the **jet spine.**

Step 1. Development of a new code for Relativistic Hydrodynamics (RHD)

Summary of HOW-RHD code

To simulate **accurate** and **realistic** relativistic flow, we adopt the following schemes

1. **5th order accurate WENO scheme (Jiang & Shu 1996, Jiang & Wu 1999)** for spatial integration

2. **Strong stability preserving Runge-Kutta (SSPRK) scheme (Spiteri & Ruuth 2002)** for time integration

3. **Realistic equation of state (RC, Ryu et al 2006)** to treat the flow with γ=4/3 - 5/3

4. **Transverse-flux averaging** for multi-dimensional flows **(Buchmüller et al. 2016)**

5. **Modification of eigenvalues for Suppression of Carbuncle Instability (Fleischmann et al. 2020)**

RHD equations

$$\frac{\partial D}{\partial t} + \frac{\partial}{\partial x_j}(D v_j) = 0$$

$$\frac{\partial M_i}{\partial t} + \frac{\partial}{\partial x_j}(M_i v_j + p\delta_{ij}) = 0$$

$$\frac{\partial E}{\partial t} + \frac{\partial}{\partial x_j}[(E + p) v_j] = 0$$

(1) Mass conservation
(2) Momentum conservation
(3) Energy conservation

$D = \rho\Gamma$: mass density
$M_i = \Gamma^2 h \rho v_i$: momentum density
$E = \Gamma^2 h\rho - p$: energy density

ρ : proper rest mass density Γ: Lorentz factor h : specific enthalpy
v_i : fluid three vector p : isotropic gas pressure

Equation of state (EOS)

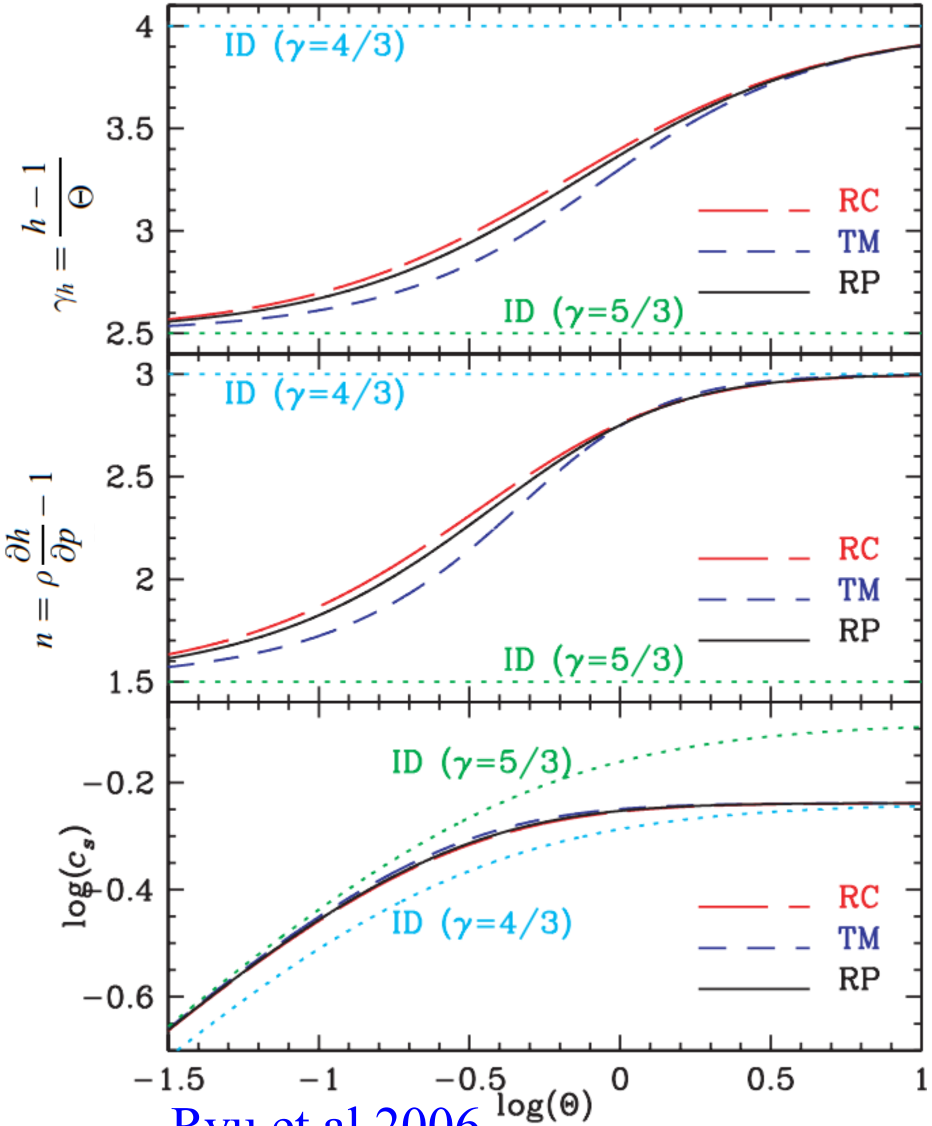

Ryu et al 2006

For relativistic flows with thermal speed of particles ~ c, the following EOSs that approximate the EOS of single-component perfect in relativistic regime (RP) is used:

$$\text{RP:}\quad h(p,\rho) = \frac{K_3(1/\Theta)}{K_2(1/\Theta)},\ \text{(K's – Bessel functions)}$$

$\Theta = p/\rho$ is a temperature-like variable.

(RP is too expensive to be implemented in numerical codes).

$$\text{RC:}\quad h = 2\frac{6\Theta^2 + 4\Theta + 1}{3\Theta + 2}.$$

(Ryu et al 2006)

Weighted Essentially Non-Oscillatory (WENO) scheme

Calculating the physical flux using a **5th order accurate finite-difference (FD) WENO reconstruction.**

$$q'_{i,j,k} = q_{i,j,k} - \frac{\Delta t}{\Delta x}\left(F_{i+\frac{1}{2},j,k} - F_{i-\frac{1}{2},j,k}\right) - \frac{\Delta t}{\Delta y}\left(G_{i,j+\frac{1}{2},k} - G_{i,j-\frac{1}{2},k}\right) - \frac{\Delta t}{\Delta z}\left(H_{i,j,k+\frac{1}{2}} - H_{i,j,k-\frac{1}{2}}\right),$$

$$\begin{aligned} F_{i+\frac{1}{2}} = & \frac{1}{12}\left(-F_{i-1} + 7F_i + 7F_{i+1} - F_{i+2}\right) \\ & + \sum_{s=1}^{5}\Big[-\varphi_N\left(\Delta F^{s+}_{i-\frac{3}{2}}, \Delta F^{s+}_{i-\frac{1}{2}}, \Delta F^{s+}_{i+\frac{1}{2}}, \Delta F^{s+}_{i+\frac{3}{2}}\right) \\ & + \varphi_N\left(\Delta F^{s-}_{i+\frac{5}{2}}, \Delta F^{s-}_{i+\frac{3}{2}}, \Delta F^{s-}_{i+\frac{1}{2}}, \Delta F^{s-}_{i-\frac{1}{2}}\right)\Big] R^s_{i+\frac{1}{2}}, \end{aligned}$$

$$\varphi_N(a, b, c, d) = \frac{1}{3}\omega_0(a - 2b + c) + \frac{1}{6}\left(\omega_2 - \frac{1}{2}\right)(b - 2c + d).$$

$$\omega_0 = \frac{\delta_0}{\delta_0 + \delta_1 + \delta_2}, \quad \omega_2 = \frac{\delta_2}{\delta_0 + \delta_1 + \delta_2}.$$

Tests for three different WENO weight functions,

1. WENO JS (Jiang & Shu 1996),
2. WENO Z (Borges et al. 2008),
3. WENO ZA (Liu et al. 2018).

WENO-Z is both **accurate** and **robust.**

→ **Selected as the default scheme**

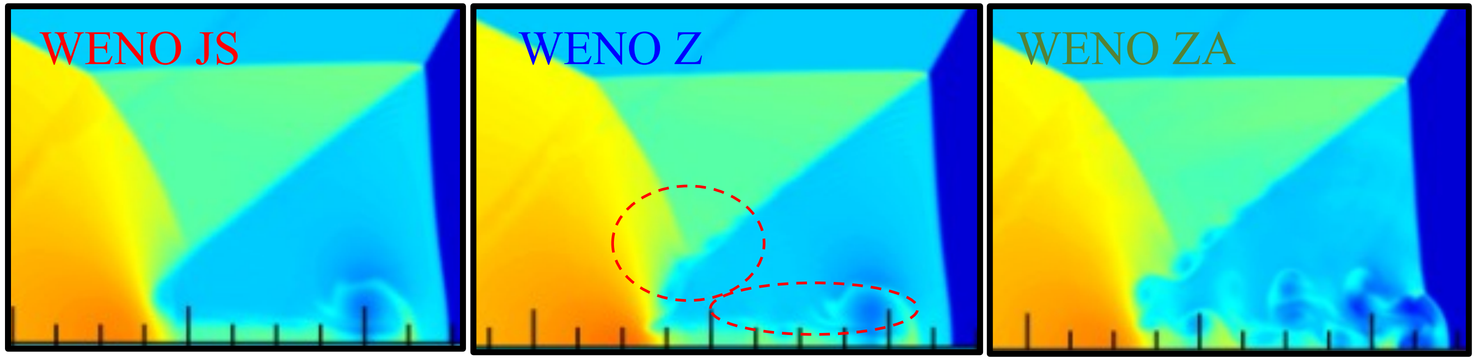

Relativistic double-Mach reflection problem with an inclined shock

$$\delta_r^{JS} = \frac{C_r}{(\epsilon + IS_r)^2}, \quad r = 0, 1, 2, \qquad \text{WENO JS}$$

$$\delta_r^{Z} = C_r\left(1 + \left(\frac{\tau_5}{\epsilon + IS_r}\right)^2\right), \quad r = 0, 1, 2, \qquad \text{WENO Z}$$

$$\delta_r^{ZA} = C_r\left(1 + \frac{A \cdot \tau_6}{\epsilon + IS_r}\right), \quad r = 0, 1, 2, \qquad \text{WENO ZA}$$

Strong stability preserving Runge–Kutta (SSPRK)

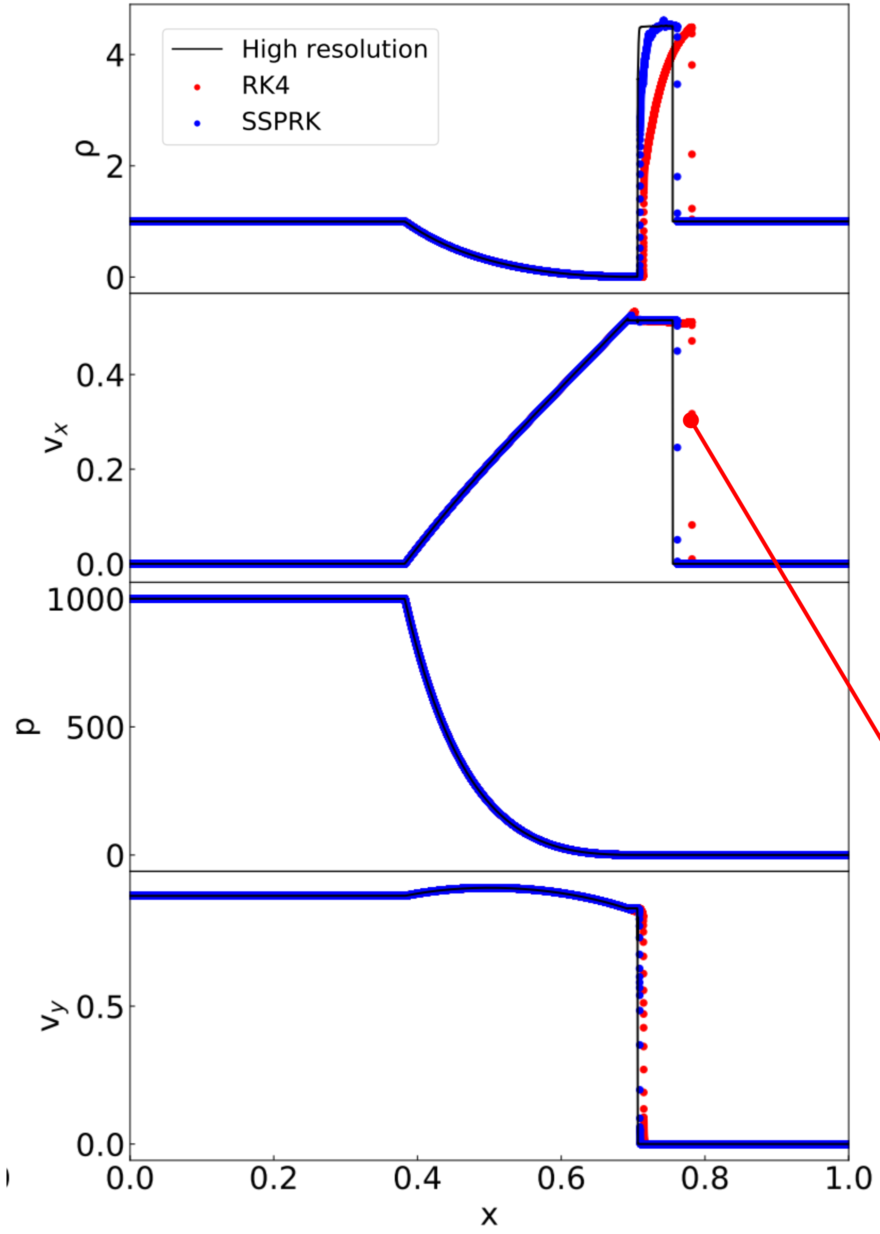

(Spiteri & Ruuth 2002)

$$\boldsymbol{q}^{(0)} = \boldsymbol{q}^n, \qquad \boldsymbol{q}^{(l)} = \sum_{m=0}^{l-1} (\chi_{lm}\boldsymbol{q}^{(m)} + \Delta t \beta_{lm} \boldsymbol{\mathcal{L}}^{(m)}), \quad l = 1, 2, \cdots, 5, \qquad \boldsymbol{q}^{n+1} = \boldsymbol{q}^{(5)}.$$

$\rho = 1$ $v_x = 0$ $v_y = 0.9c$ $p = 10^3$	$\rho = 1$ $v_x = 0$ $v_y = 0$ $p = 10^{-2}$

Initial condition of this shock tube test

- **Most of the code with WENO uses 4th order Runge-Kutta (RK4) scheme for time integration.**
- **In RHD simulation, shock with transverse flow is hard to simulate.**
- **In such cases, even shock positions cannot be followed properly. It is a well-known problem in RHD simulations.**
- **With the SSPRK method, the code can simulate harsh conditions with strong stability.**

Treatment for multi-dimensional problems

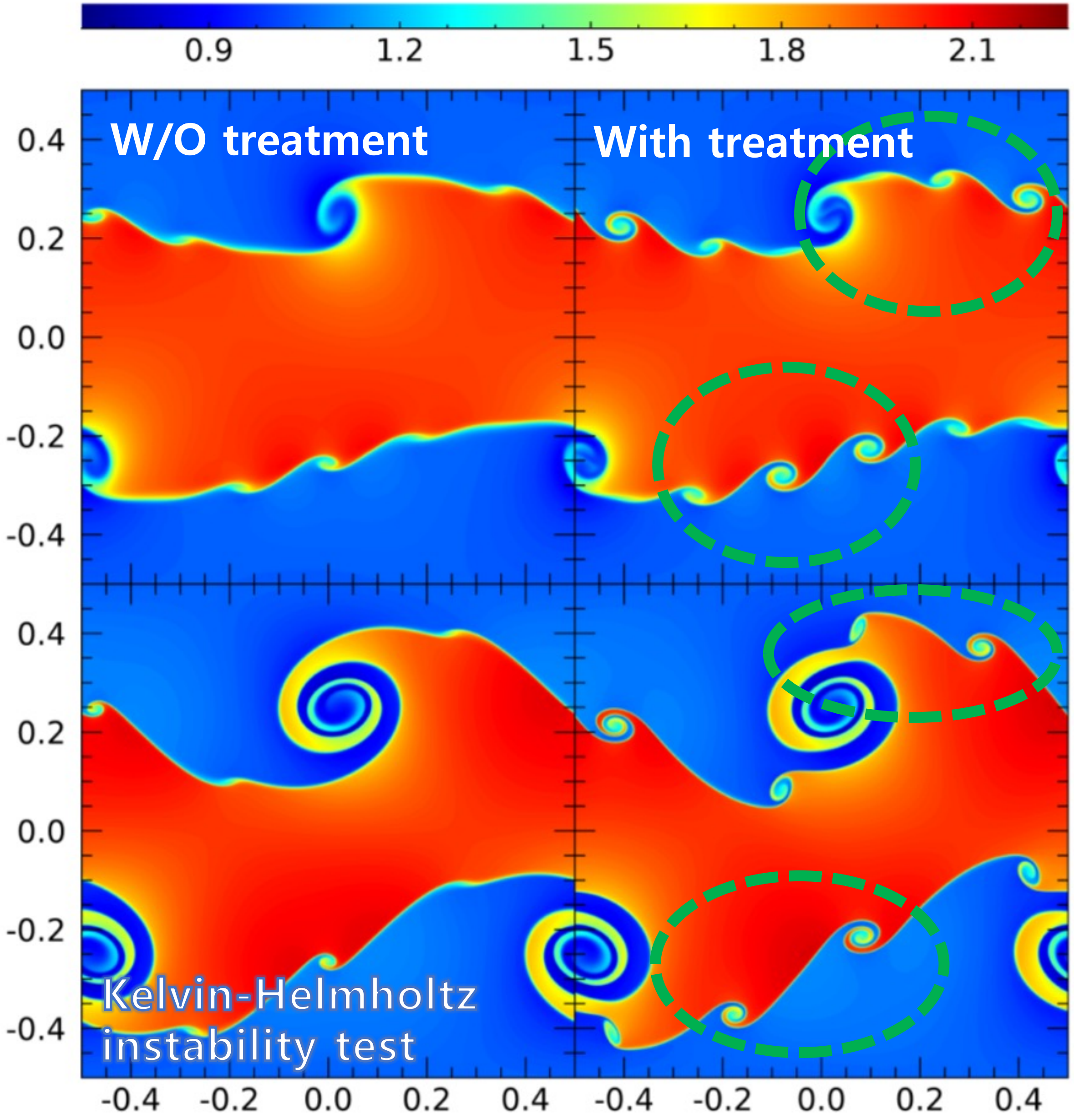

$$\bar{q}_{i,j,k} = q_{i,j,k} - \frac{1}{24}\left(q_{i,j-1,k} - 2q_{i,j,k} + q_{i,j+1,k}\right) - \frac{1}{24}\left(q_{i,j,k-1} - 2q_{i,j,k} + q_{i,j,k+1}\right),$$

$$\bar{F}_{i\pm\frac{1}{2},j,k} = F_{i\pm\frac{1}{2},j,k} + \frac{1}{24}\left(F_{i\pm\frac{1}{2},j-1,k} - 2F_{i\pm\frac{1}{2},j,k} + F_{i\pm\frac{1}{2},j+1,k}\right) + \frac{1}{24}\left(F_{i\pm\frac{1}{2},j,k-1} - 2F_{i\pm\frac{1}{2},j,k} + F_{i\pm\frac{1}{2},j,k+1}\right).$$

- **Transverse flux averaging scheme is proposed as a modified dimension-by-dimension method for FV WENO schemes, which leads to high order accuracies for smooth solutions** (Buchmüller et al. 2016).

- **By bringing this scheme to our FD WENO scheme, we improve the accuracies for multi-dimensional flows.**

Treatment for carbuncle instability

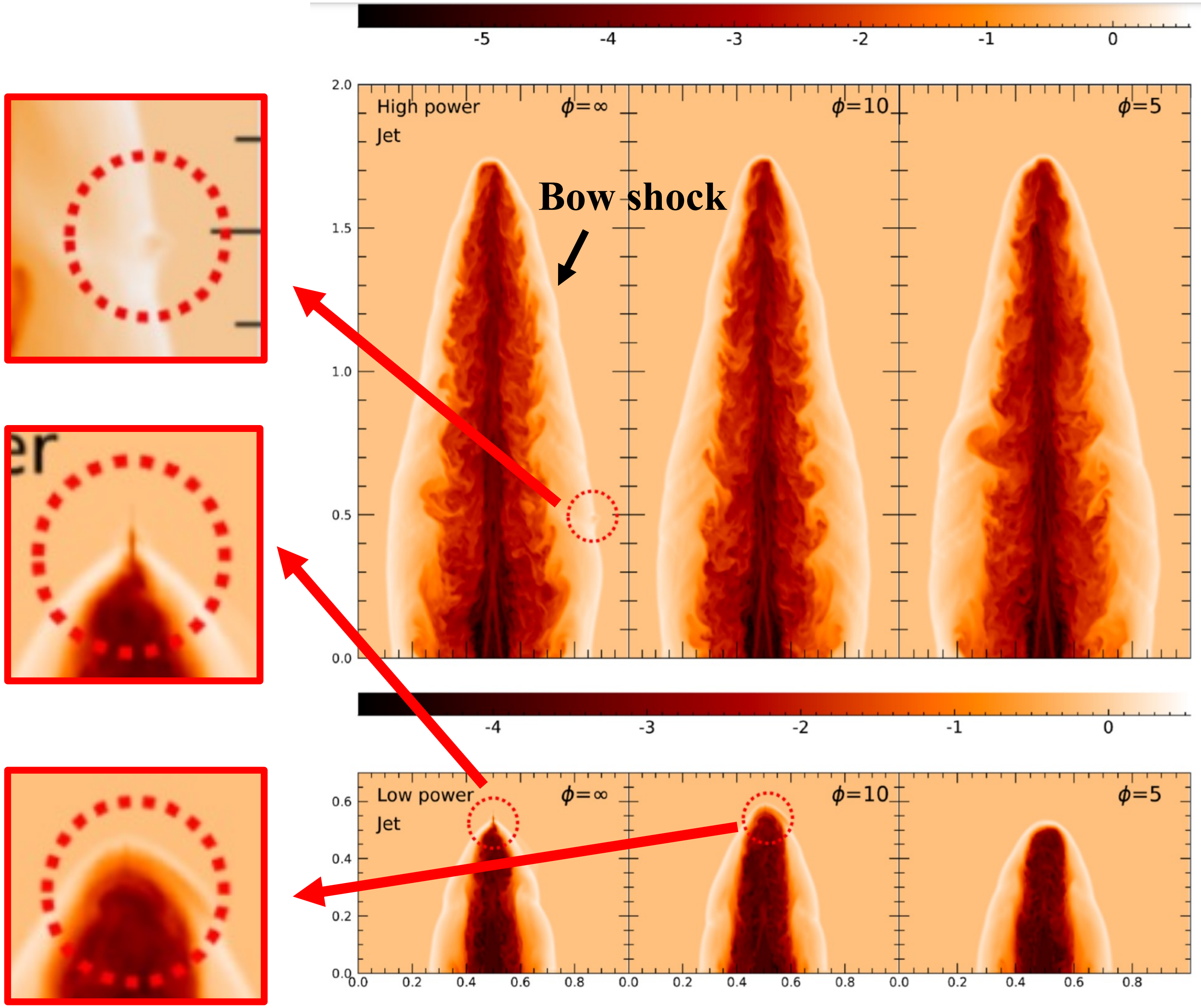

Unphysical structures due to carbuncle instability

- **Carbuncle instability arises at slow-moving grid-aligned shocks, e.g., bow shock of the jet.**
- **modified eigenvalues for RHD**

$$c'_s = \min(\phi|v_x|, c_s),$$

(Fleischmann et al. 2020)

$$\lambda'_{1,5} = \frac{(1 - c'^2_s)v_x \mp c'_s/\Gamma\sqrt{Q}}{1 - c'^2_s v^2},$$

$$\lambda'_{2,3,4} = v_x,$$

$$Q = 1 - v_x^2 - c'^2_s(v_y^2 + v_z^2)$$

ϕ is a tunable parameter

➔ **This can effectively suppress Carbuncle instability**

Step 2. Simulations of jets:
Structures and Dynamics

Relativistic hydrodynamic simulations of relativistic jets

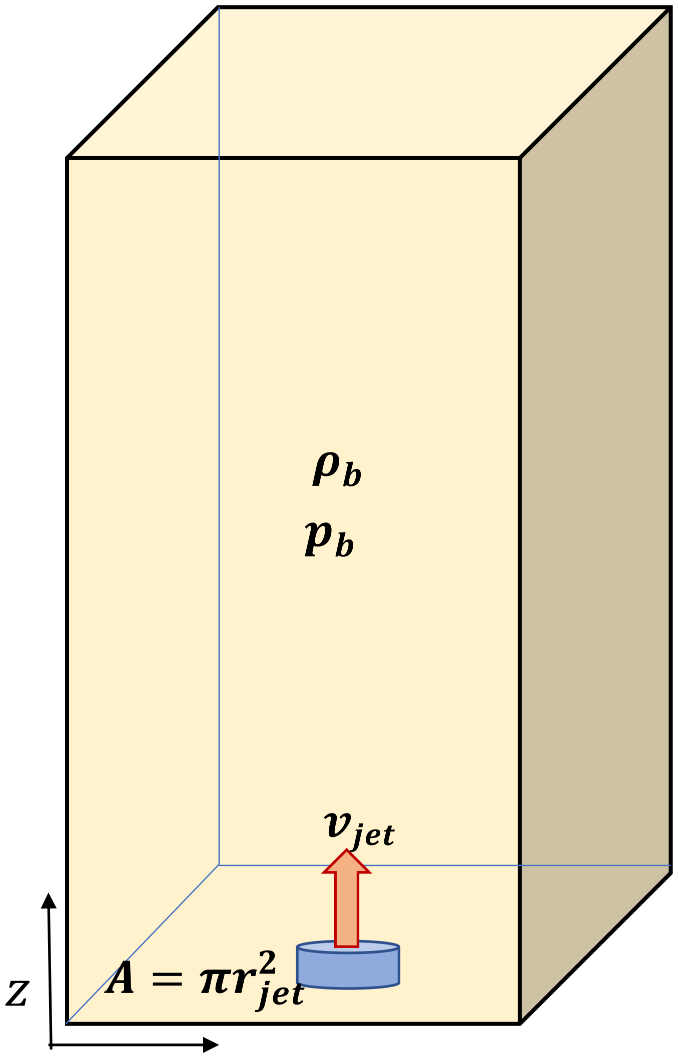

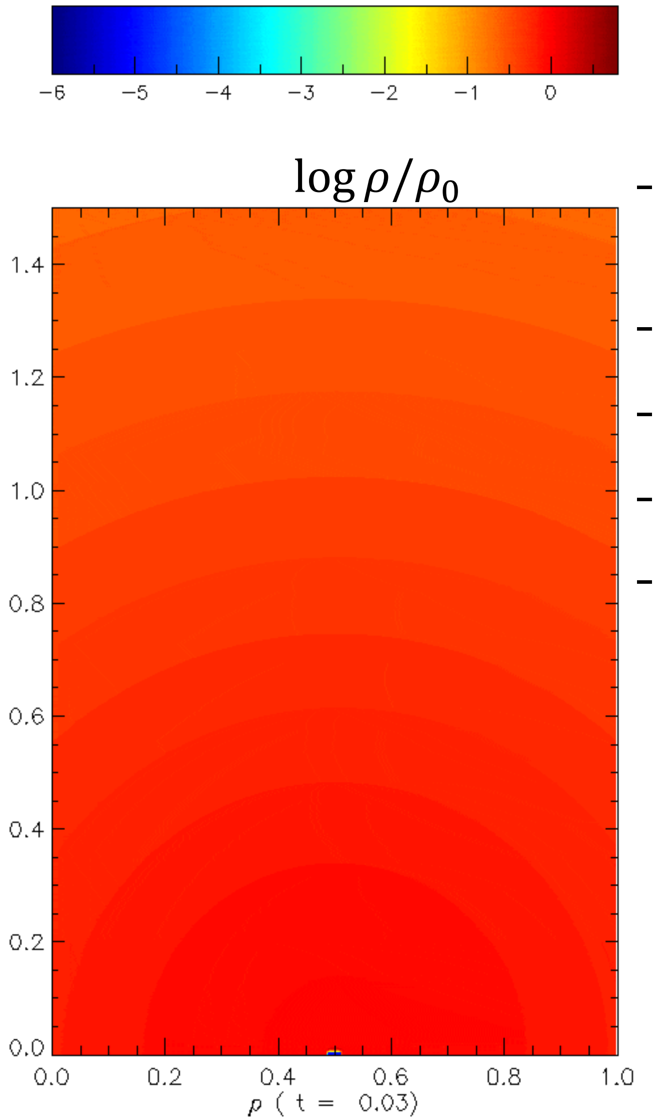

Seo, Ryu, & Kang 2021b
Seo, Ryu, & Kang 2023a, b

- Relativistic HD simulations using a new state-of-art RHD code (HOW-RHD)
- Range of the jet power : $10^{42} - 10^{47}$ erg/s
- Range of the jet length : 0.5-200 kpc
- Dynamical timescale : 1kyr~100 Myr
- Background profile
  (Intergalactic medium/Intracluster medium)

$$\rho(r) = \rho_0 \left[1 + \left(\frac{r}{r_c}\right)^2\right]^{-3\beta/2}$$

r : distance from the center of the cluster
r_c : core radius, 1.2-50kpc
β: 0.5-0.73

Flow structures of radio galaxy jets

Seo, Ryu, & Kang 2023a, b

High-power jet
→ small deceleration
of the jet flow

well-maintained jet-spine,
large boosting due to the
relativistic beaming of
the jet flow

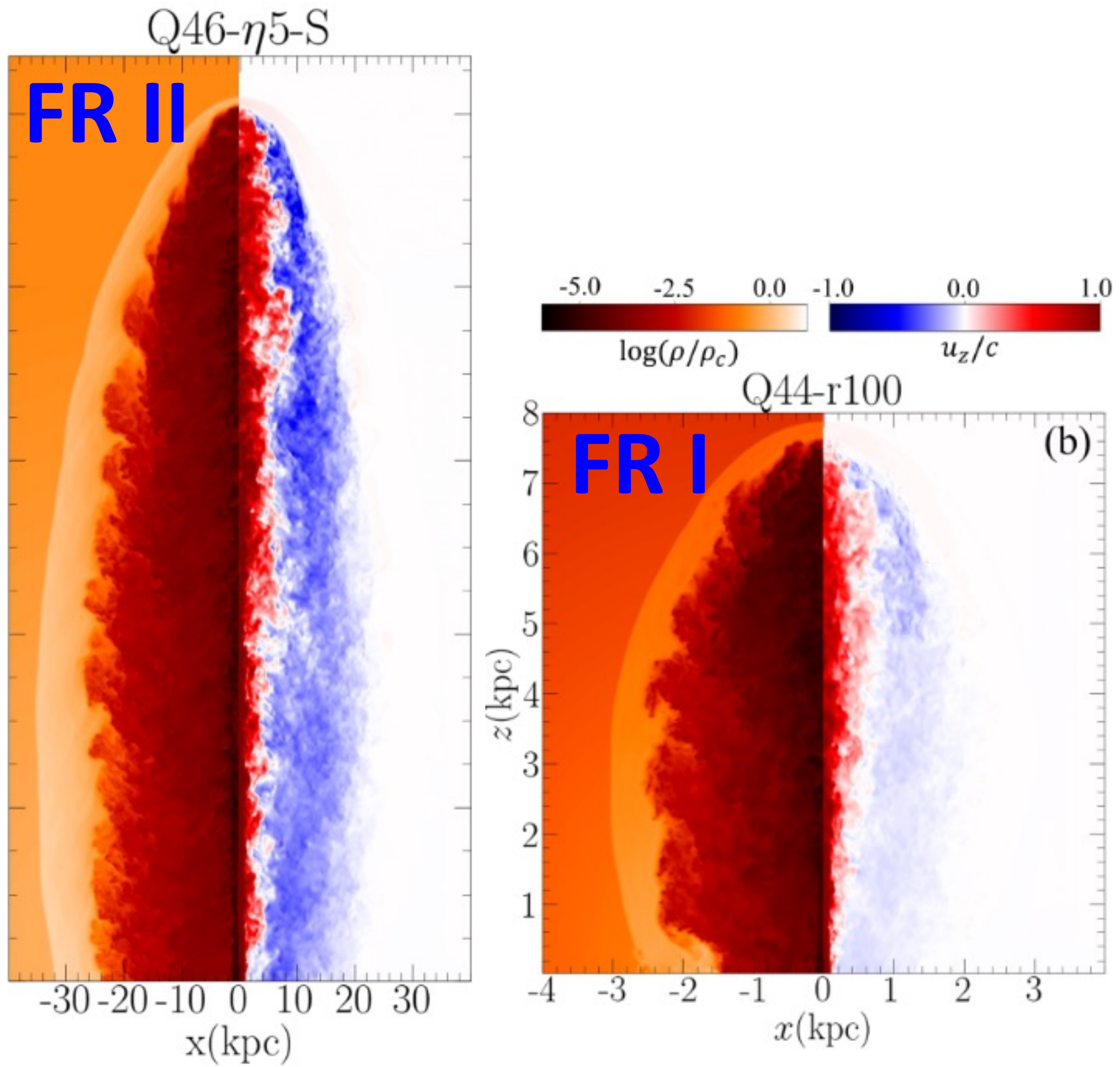

Low-power jet
→ significant deceleration
of the jet flow

well developed cocoon,
mildly relativistic jet

Properties of Shocks

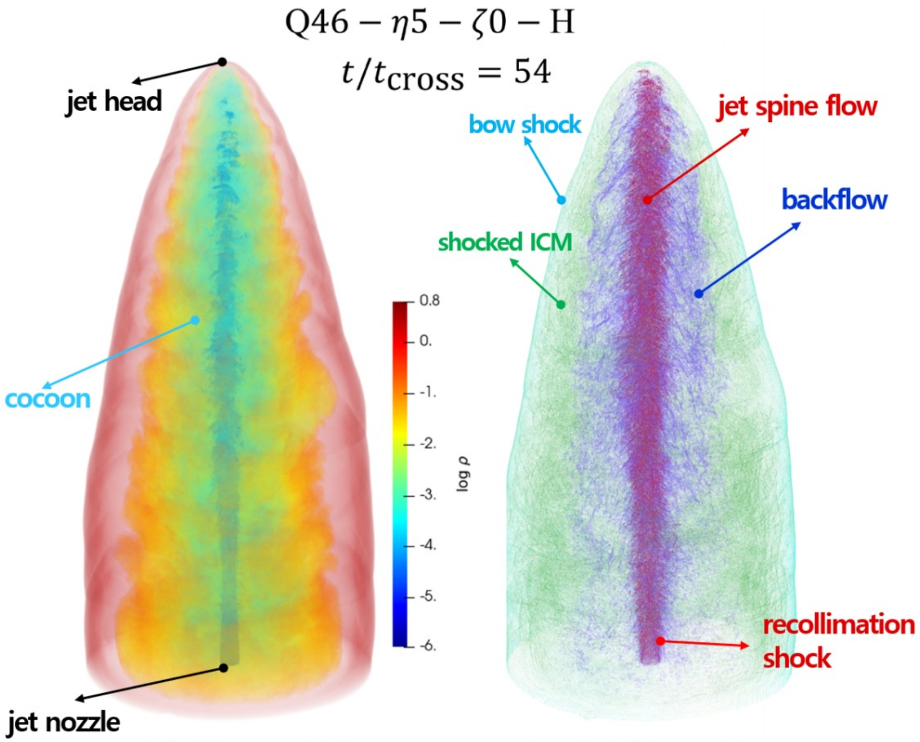

(a) density (b) shock locations

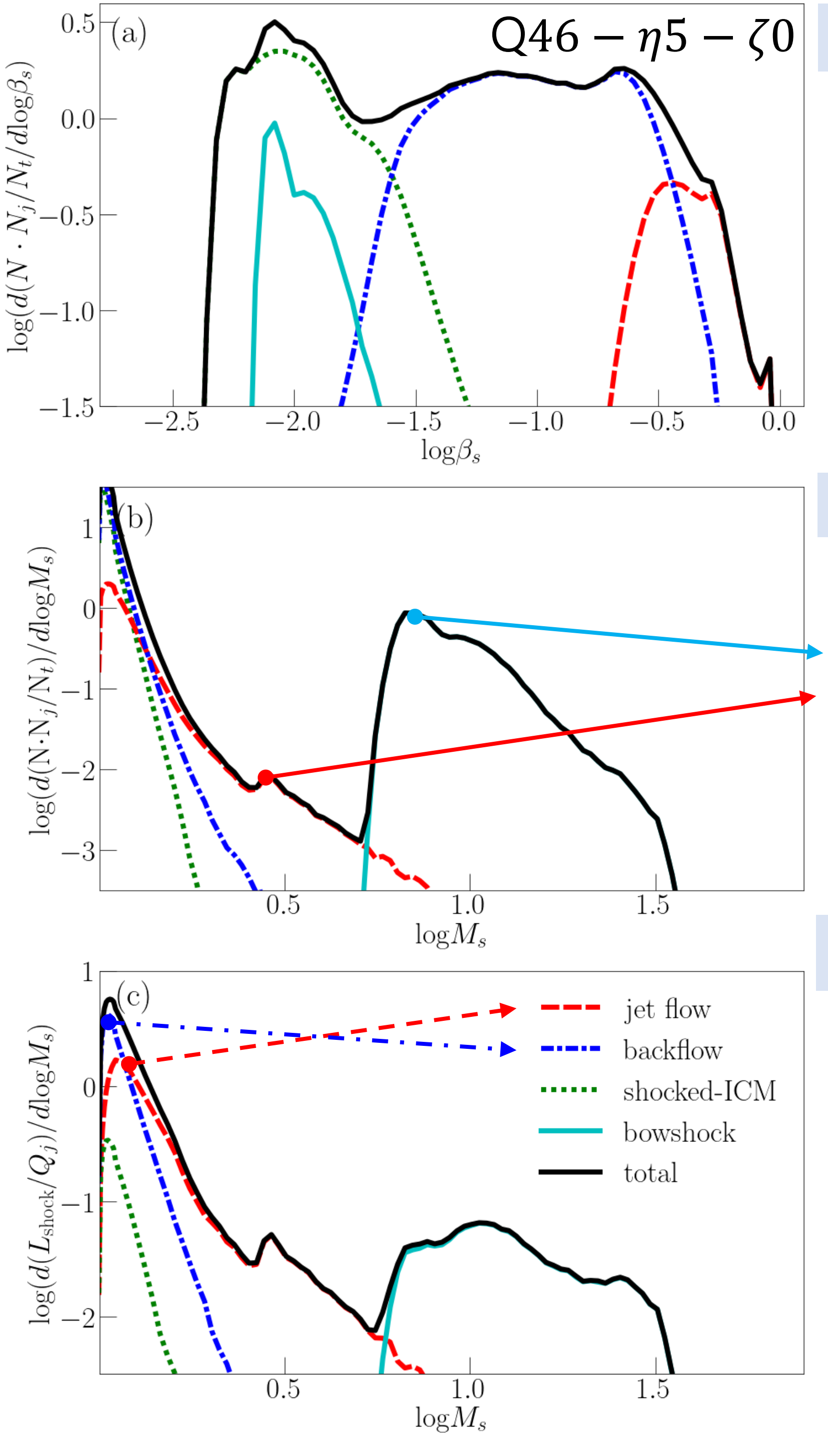

Shock speed

Range of $\boldsymbol{\beta_s = v_s/c}$

($\boldsymbol{v_s}$: shock velocity)

jet flow : 0.2-1.0

Backflow : 0.01-0.4

Bowshock &

Shocked-ICM : < 0.005-0.05

Mach number

Peaks of $N(M_s)$ occur at

-M_s~6.5 for the bow shock

-M_s~3 for the recollimation shock

Other shocks have power-law PDF, $N(M_s) \propto M_s^{-5\sim-13}$

Kinetic energy dissipation rate

$$\Delta\Phi_{\rm shock} \equiv \Gamma_1(\Gamma_1-1)\rho_1 c^2 v_1 - \Gamma_2(\Gamma_2-1)\rho_2 c^2 v_2$$

$$L_{\rm shock}(M_s) = \sum_{\log M_s}^{\log M_s + d\log M_s} \Delta\Phi_{\rm shock} A_{\rm shock},$$

Shocks in jet flow & backflow have high kinetic energy dissipation rates.

Properties of Shear and Turbulence

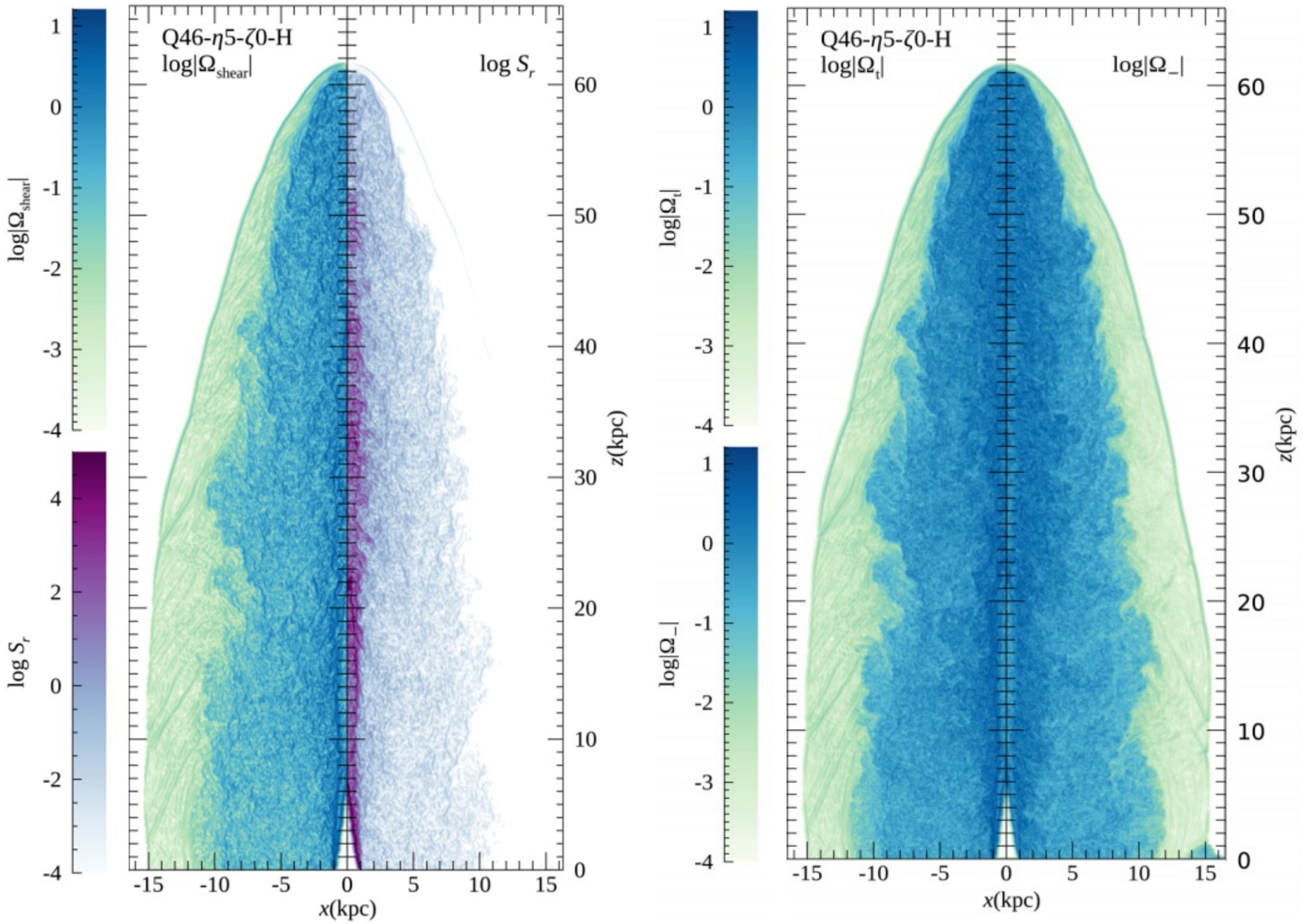

Shear

$$\Omega_{\rm shear} \equiv |\partial v_z/\partial r|$$

Relativistic shear coefficient

$$\mathcal{S}_r = \frac{\Gamma_v^4}{15}\left(\frac{\partial v_z}{\partial r}\right)^2,$$ (Rieger 2019)

Shear is strongest at jet-cocoon boundary and inside the jet flow

S_r is largest in the jet flow.

Total vorticity

$$\boldsymbol{\Omega}_t = \boldsymbol{\nabla} \times \boldsymbol{v}$$

Vorticity excluding shear

$$\boldsymbol{\Omega}_- = \boldsymbol{\Omega}_t + \frac{\partial v_z}{\partial r}\hat{\boldsymbol{\theta}},$$

Backflow has large vorticity due to Turbulence

Distribution of non-linear structures in FR-I jet

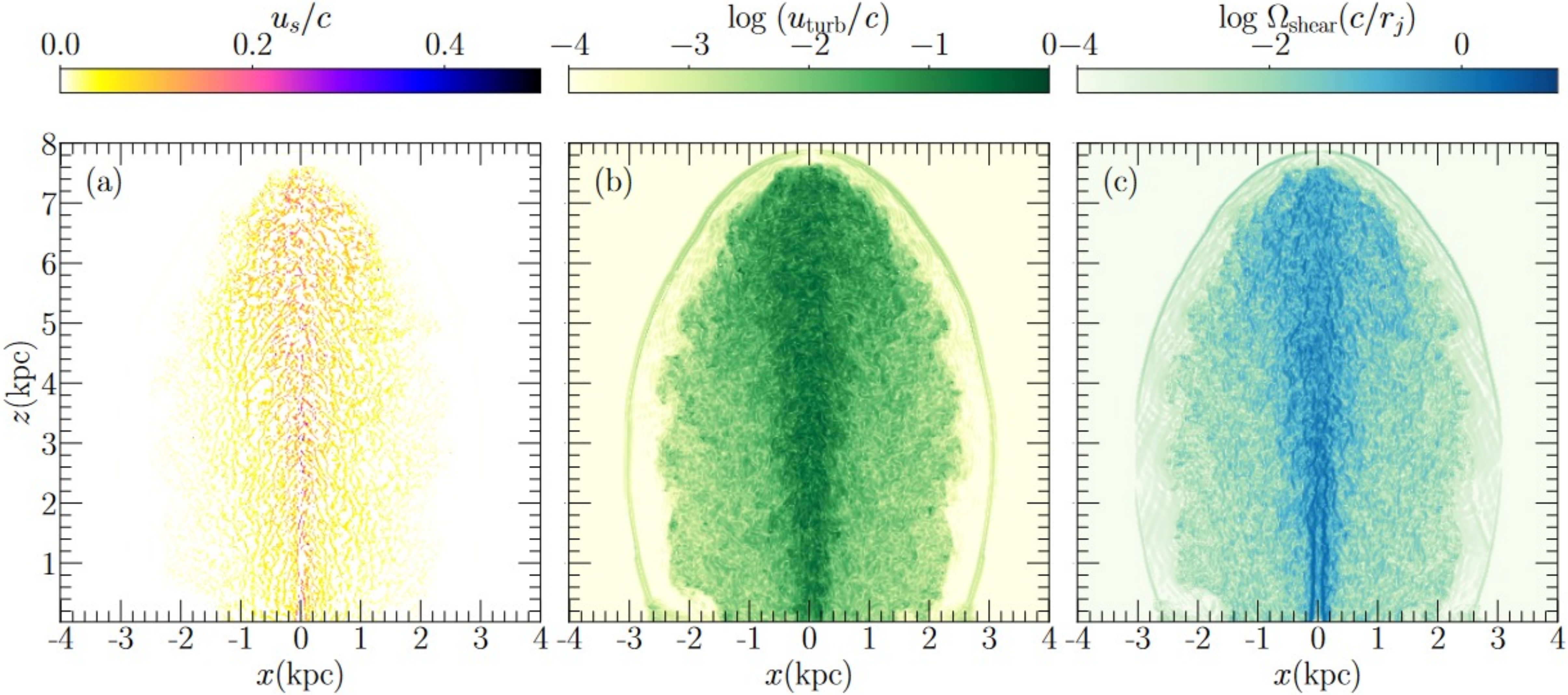

Shock energy dissipation rate

$$\mathcal{L}_{\rm shock} = \int_{M_{\rm min}} L_{\rm shock}(M_s)\, d\log M_s,$$

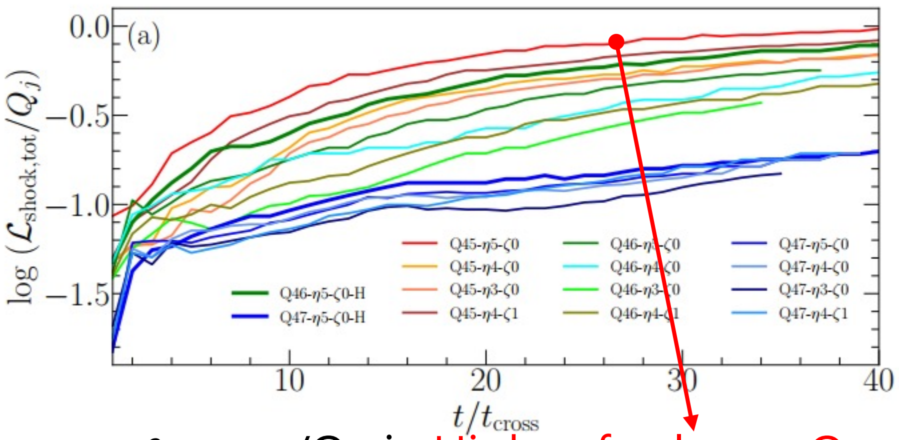

$\mathcal{L}_{\rm shock}/Q_j$ is Higher for lower Q_j

$\mathcal{L}_{\rm shock}/Q_j$ is Higher for lower $\dot{M}$

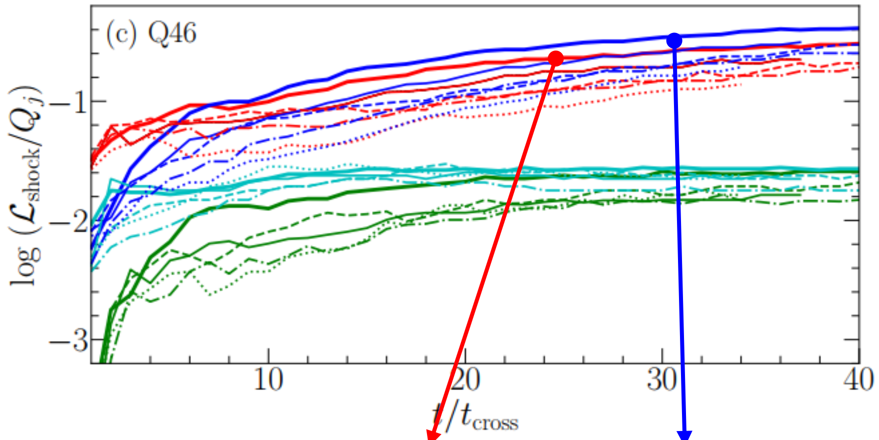

Shocks in the jet flow and backflow are most important in energy dissipation

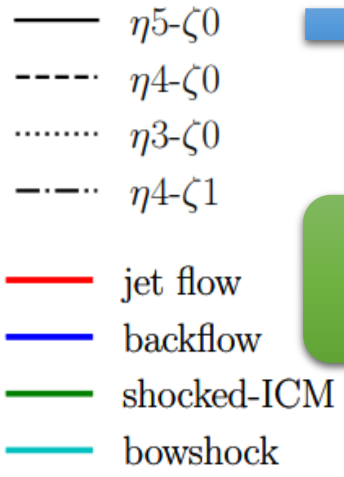

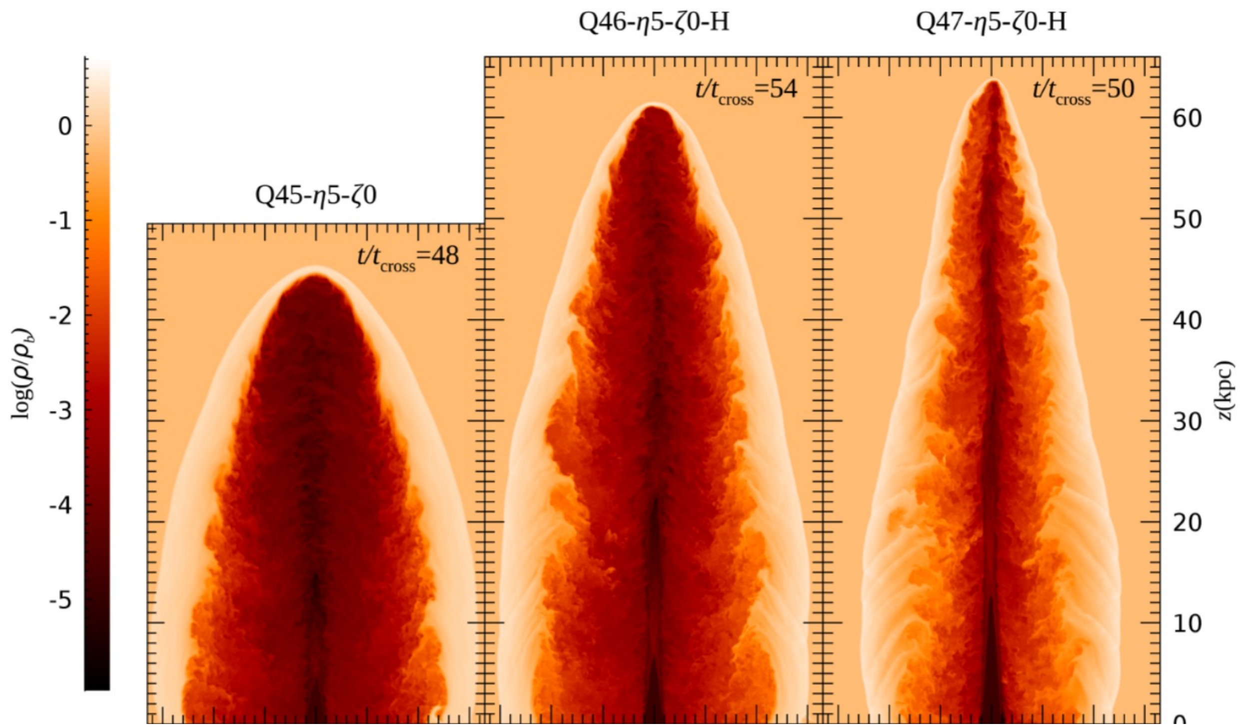

Higher Q_j, Lower $\mathcal{L}_{\rm turb}/Q_j$

Lower energy dissipation rate induces narrower cocoon

$$Q_j = \pi r_j^2 u_j \left(\Gamma_j^2 \rho_j h_j - \Gamma_j \rho_j c^2\right)$$

Turbulence energy dissipation rate

$$\mathcal{L}_{\rm turb} \approx \varphi \frac{E_{\rm turb}}{\tau_{\rm cascade}},$$

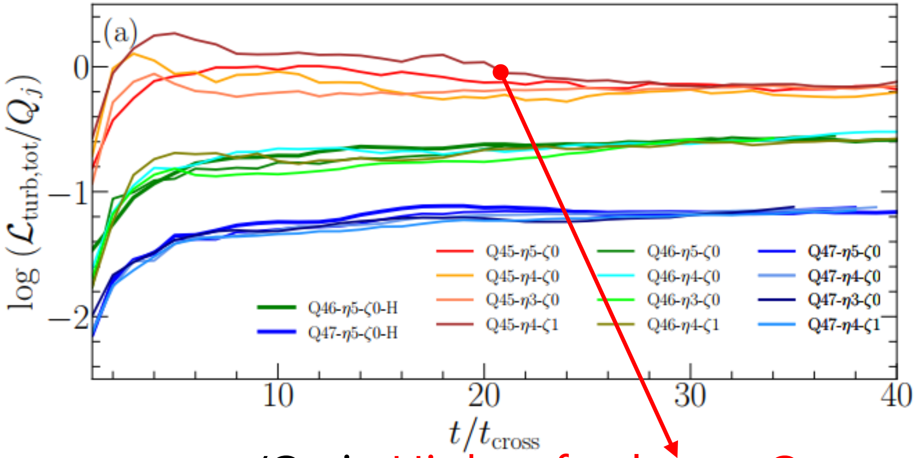

$\mathcal{L}_{\rm turb}/Q_j$ is Higher for lower Q_j

$\mathcal{L}_{\rm turb}/Q_j$ is hardly depends on $\dot{M}$

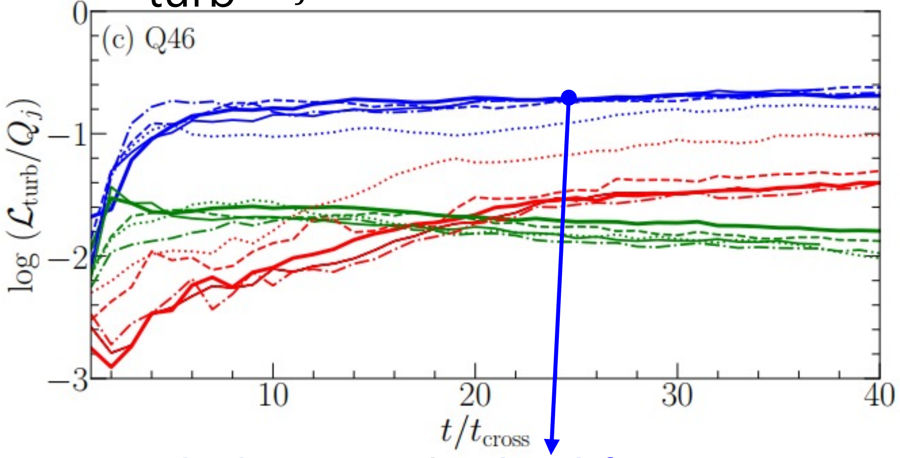

Turbulence in the backflow are most important in energy dissipation

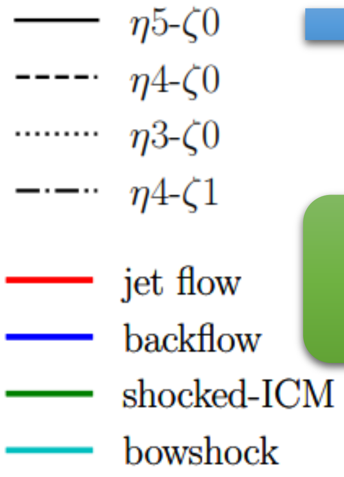

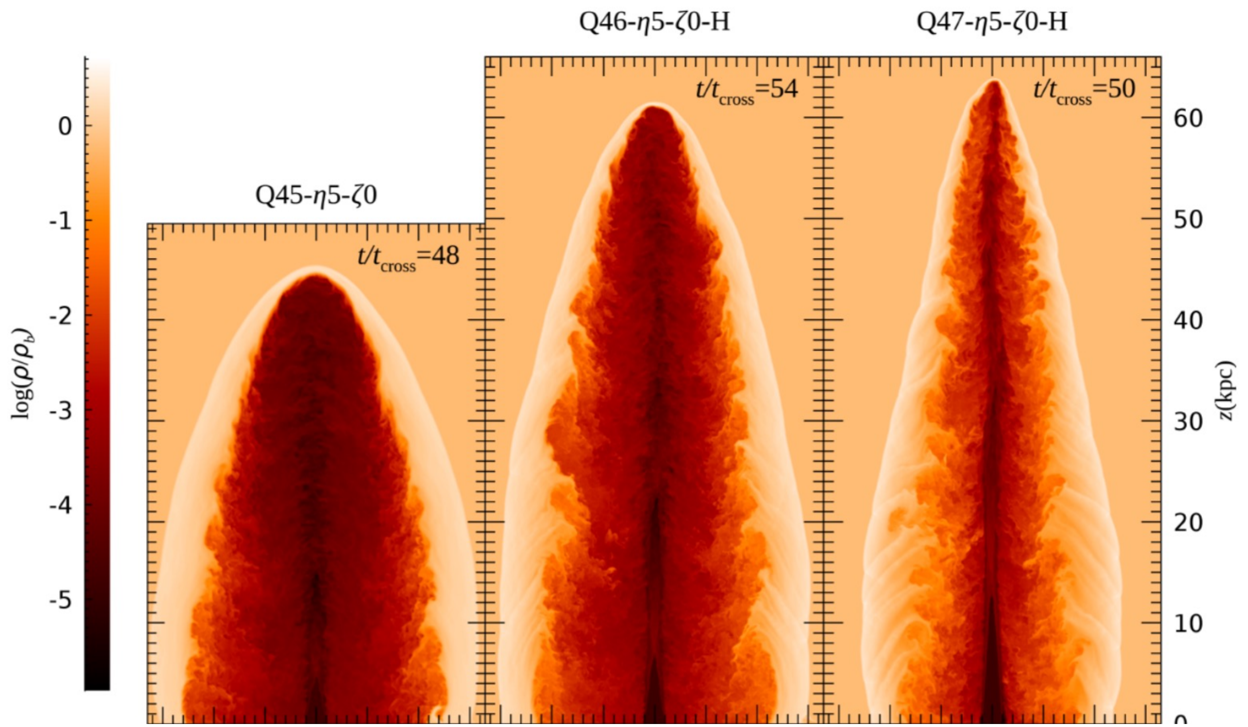

Higher Q_j, Lower $\mathcal{L}_{\rm turb}/Q_j$

Lower energy dissipation rate induces narrower cocoon

$$Q_j = \pi r_j^2 u_j \left(\Gamma_j^2 \rho_j h_j - \Gamma_j \rho_j c^2\right)$$

FR-II

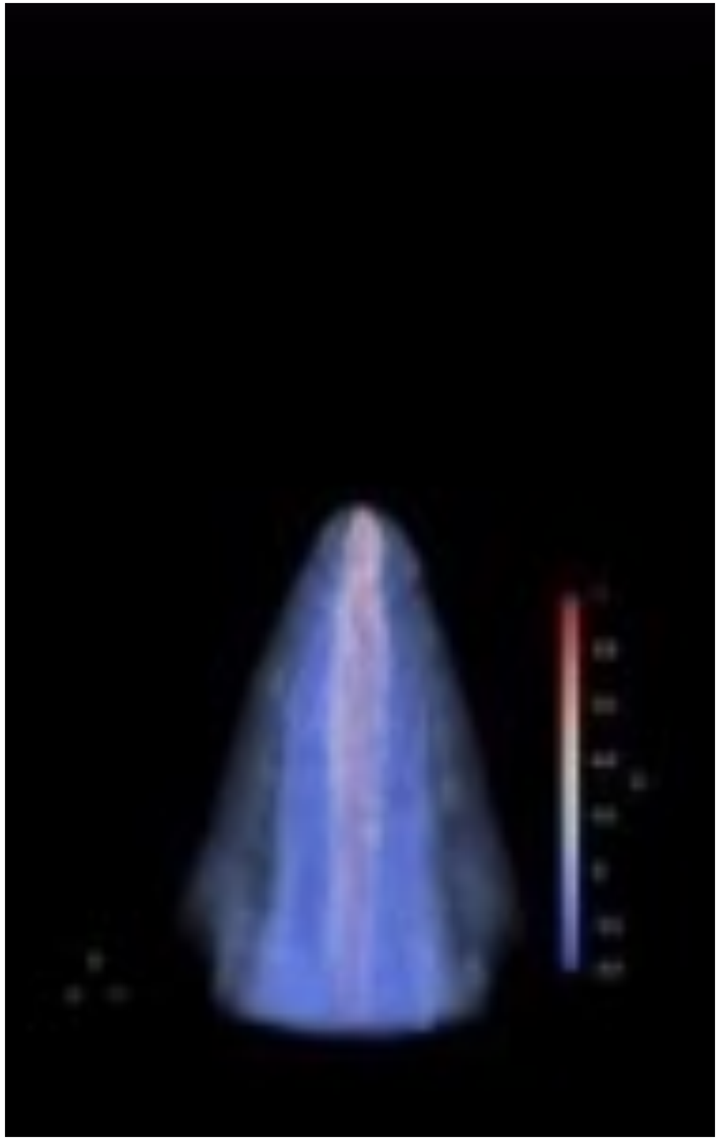

FR-I

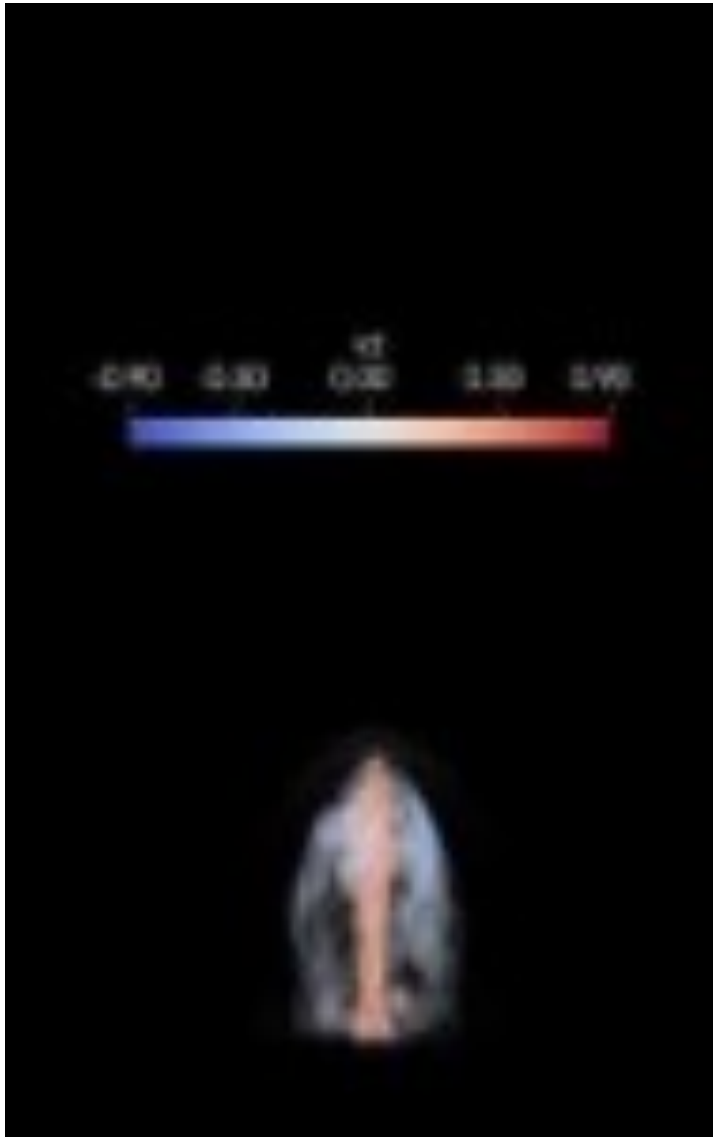

Synchrotron radiation modeling

$$\mathcal{N}_e'(\gamma') = \mathcal{N}_0'\gamma'^{-\mathcal{P}}.$$

Cosmic ray electron distribution

$$j_{\nu'}' = \frac{1}{4\pi}\int \mathcal{N}_e'(\gamma')\mathcal{P}_{\nu'}'(\gamma')d\gamma'.$$

Synchrotron emissivity

$$j_\nu = \frac{j_{\nu'}'}{(\Gamma[1-\beta\mu])^2},$$

Doppler boosting

$$\frac{dI_\nu}{ds} = j_\nu - \alpha_\nu I_\nu.$$

Radiative transfer (optically thin, $j_\nu \gg \alpha_\nu$)

Bhattacharjee, Seo, Ryu and Kang, in prep

FR-I jet

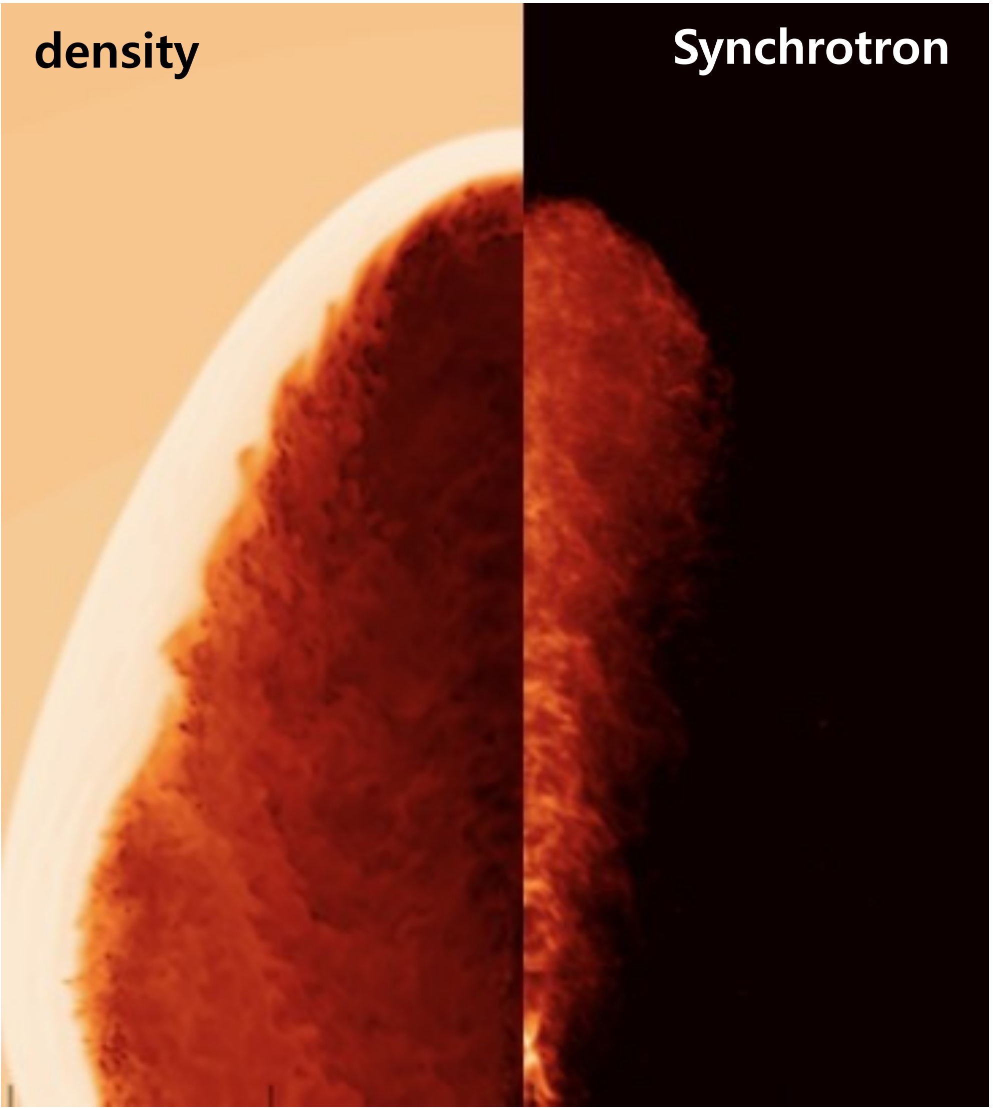

Result: Lower-power jets are more likely FR-I, higher-power jets are more likely FR-II

Bhattacharjee, Seo, Ryu and Kang, in prep

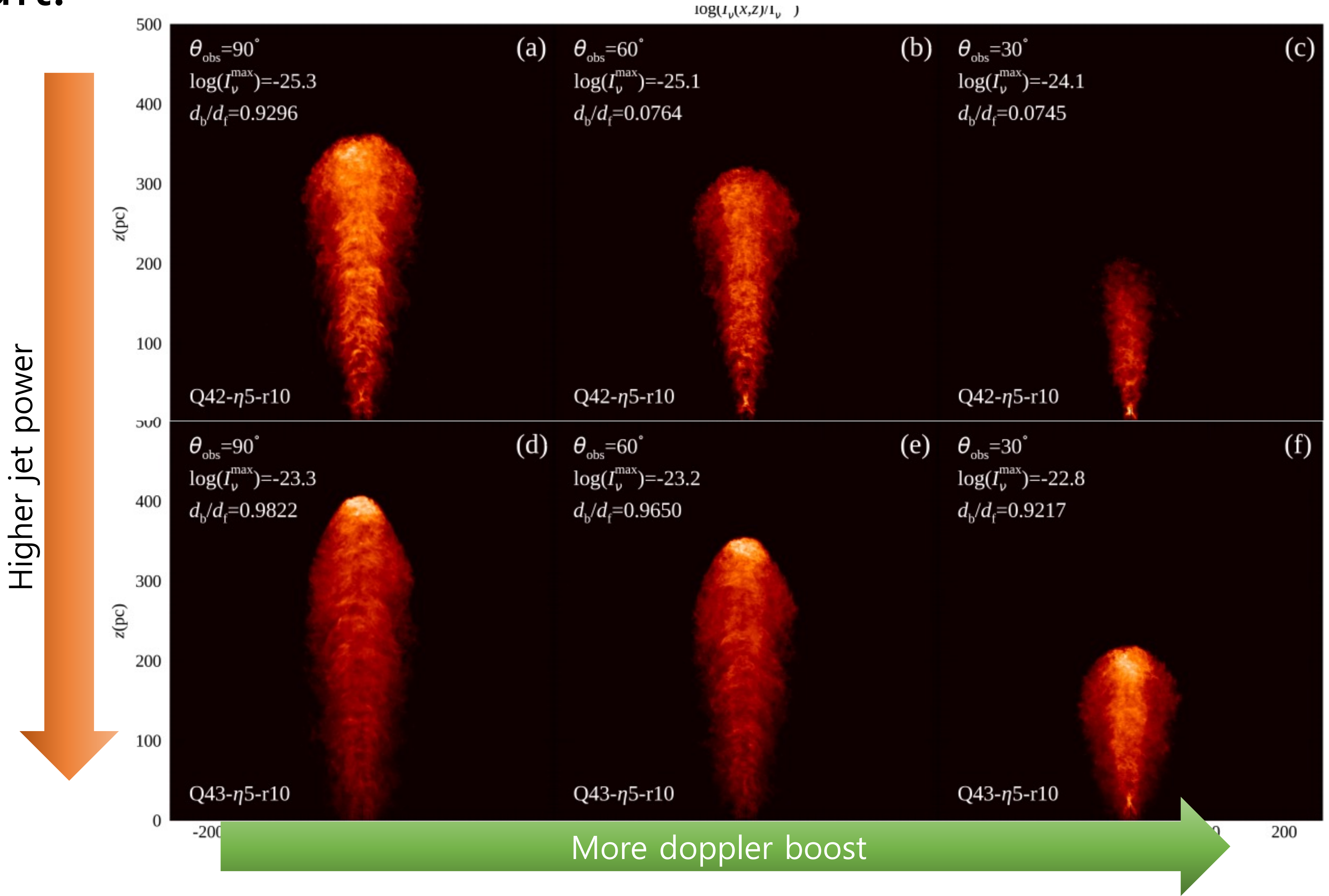

Step 3. Monte Carlo Simulations for CR acceleration, using simulated jets

Monte Carlo simulations for CR transport

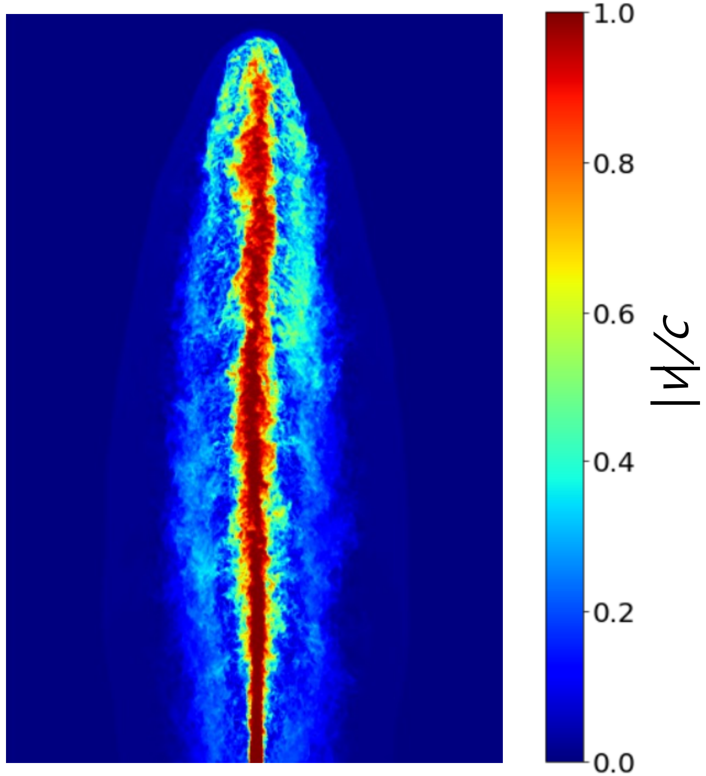

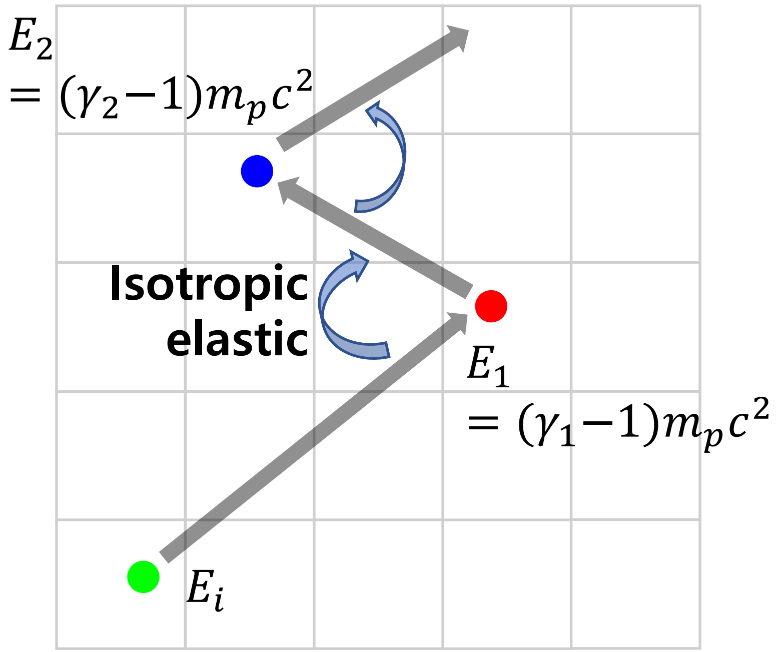

γ_n: Lorentz factor of the particle in n-th frame

Assumptions:

1. MHD waves are frozen into the background flow (in computational frame, $v_{fluid} = v_{MHD\,waves}$).
2. Particle scattering is isotropic and elastic in the rest frame of local fluid.
3. CRs gain/lose energy through scattering off MHD waves co-moving with the background plasma (obtained via Lorentz transformation of the field)

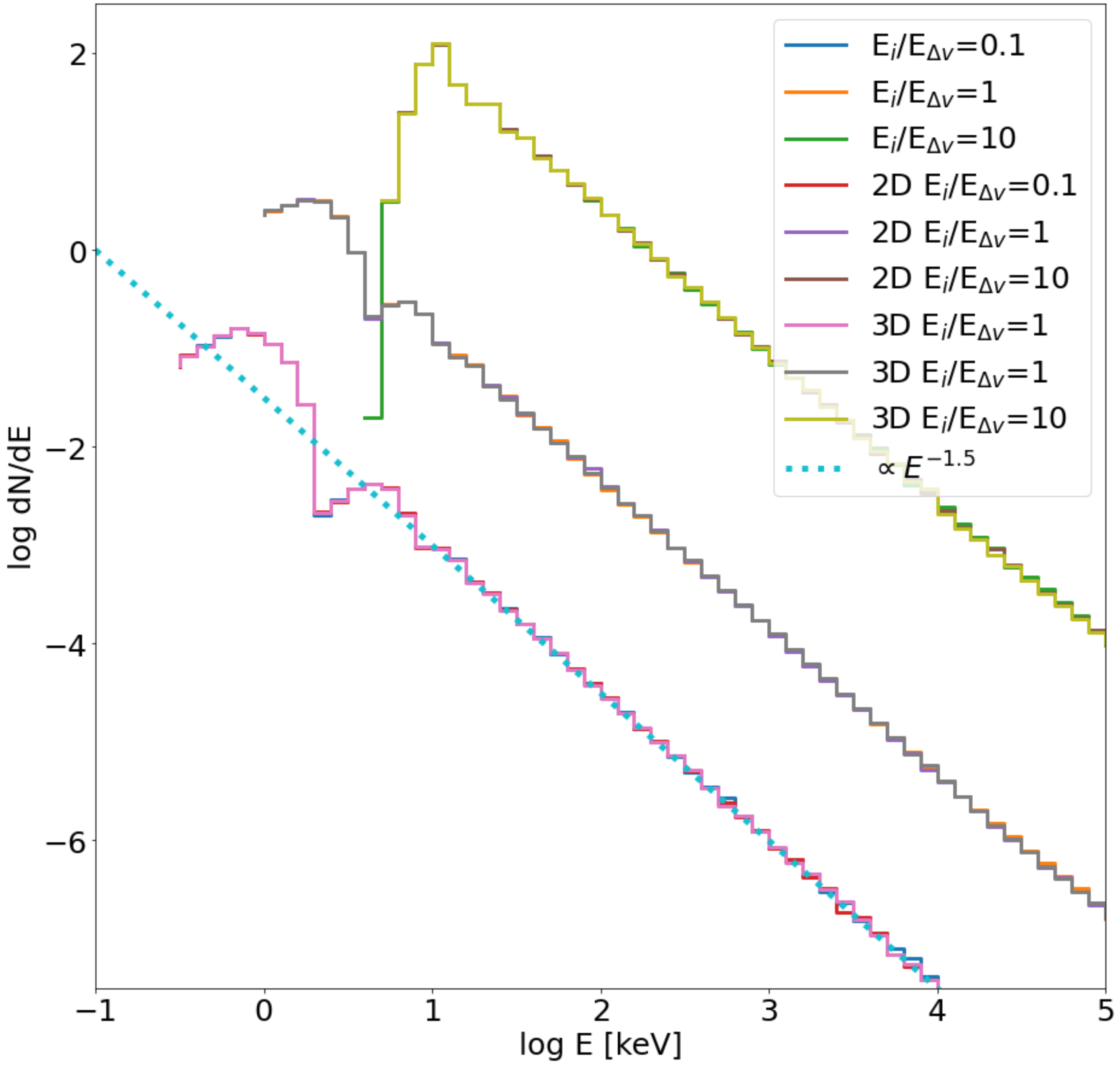

Vs = 500km/s **(non-relativistic shock)**

E_i : injection energy
$E_{\Delta v} = (\Gamma_{\Delta v} - 1)m_0c^2$

- Non-relativistic shock
- Non-relativistic particle ($\propto E^{-1.5}$)
- Initial Delta function distribution
- Relativistic terms are negligible

-2D shock velocity
V_{sx} = V_s/sqrt(2)
V_{sy} = V_s/sqrt(2)
V_{sz} = 0

-3D shock velocity
V_{sx} = V_s/sqrt(3)
V_{sy} = V_s/sqrt(3)
V_{sz} = V_s/sqrt(3)

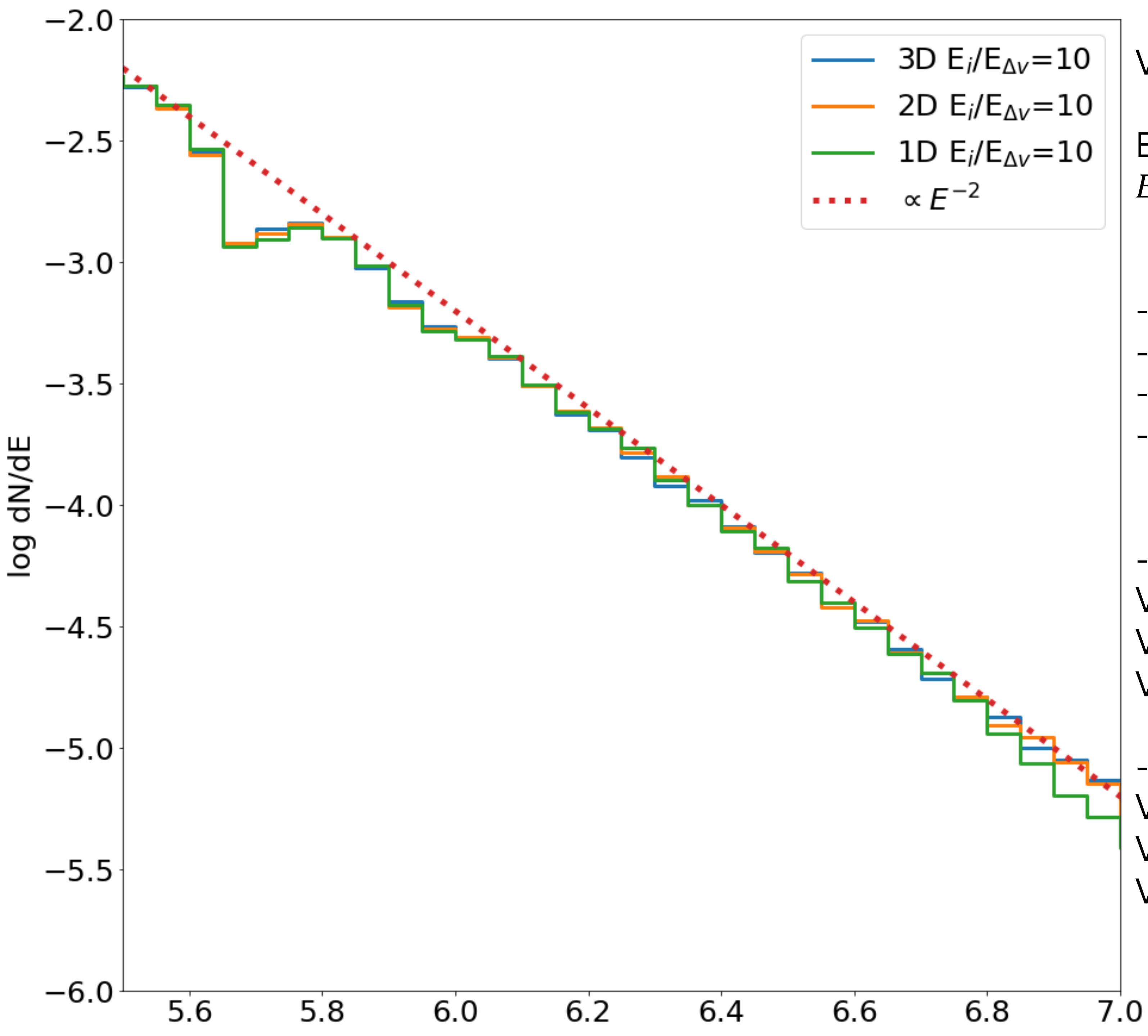

Vs = 0.3c **(sub-relativistic shock)**

E_i : injection energy

$E_{\Delta v} = (\Gamma_{\Delta v} - 1)m_0c^2$

- Sub-relativistic shock
- Relativistic particle ($\propto E^{-2}$)
- Initial Delta function distribution
- Relativistic terms are important

-2D shock velocity

V_{sx} = V_s/sqrt(2)

V_{sy} = V_s/sqrt(2)

V_{sz} = 0

-3D shock velocity

V_{sx} = V_s/sqrt(3)

V_{sy} = V_s/sqrt(3)

V_{sz} = V_s/sqrt(3)

Discrete shear acceleration

- Same setting of Ostrowski 1998

- v_j = 0.5c
- r (shock compression ratio) = 4
- v_c = 0

- 2 ways to accelerate particles

>> Particles accelerated at termination shock

>> Particles accelerated at jet-cocoon boundary

Cylindrical jet model

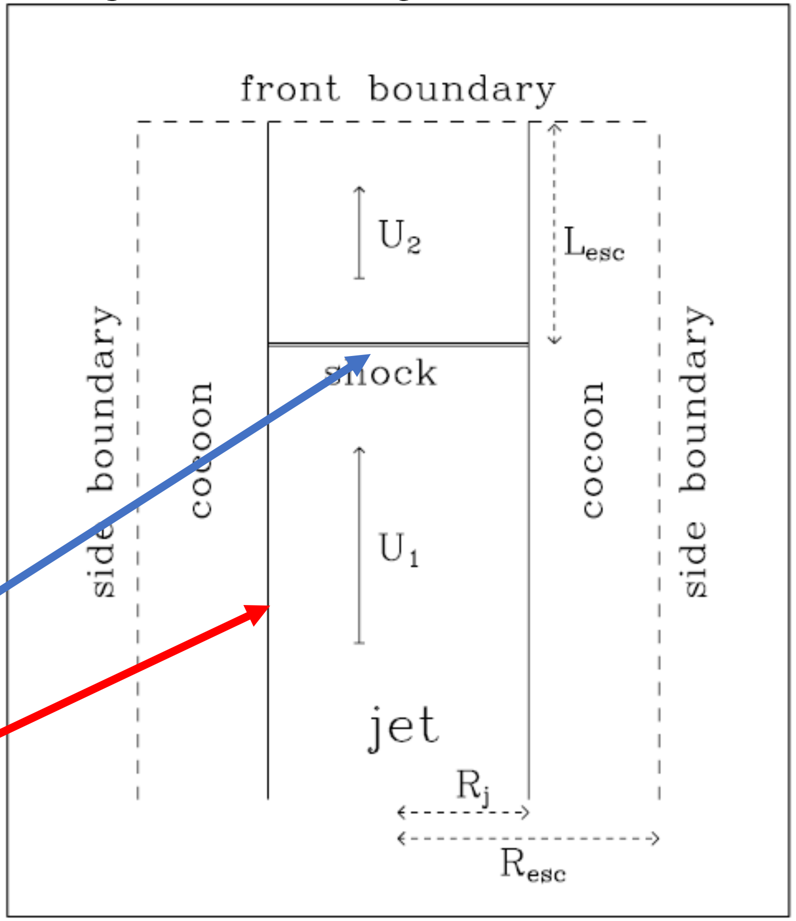

Fig. 1. A schematic representation of the terminal shock neighbourhood. The velocities and distances used in the text are indicated.

Discrete shear acceleration

- $\tau(p) = \tau_0 (\frac{p}{p_0})^{\delta}$ **mean scattering time**

✓ $\delta = 1$ **(Bohm diffusion)**

- ***Shear acc***

✓ $f(p) \propto p^{-(3-\delta)} \propto p^{-2}$

✓ $F(p) = \frac{dN(p)}{d \log p} \propto p^1$ for shear acc

- ***Shock acc***

✓ $f(p) \propto p^{-(3r/(r-1))}$

✓ $F(p) \propto p^{-\left(\frac{3r}{r-1}\right)+3}$ for shock acc

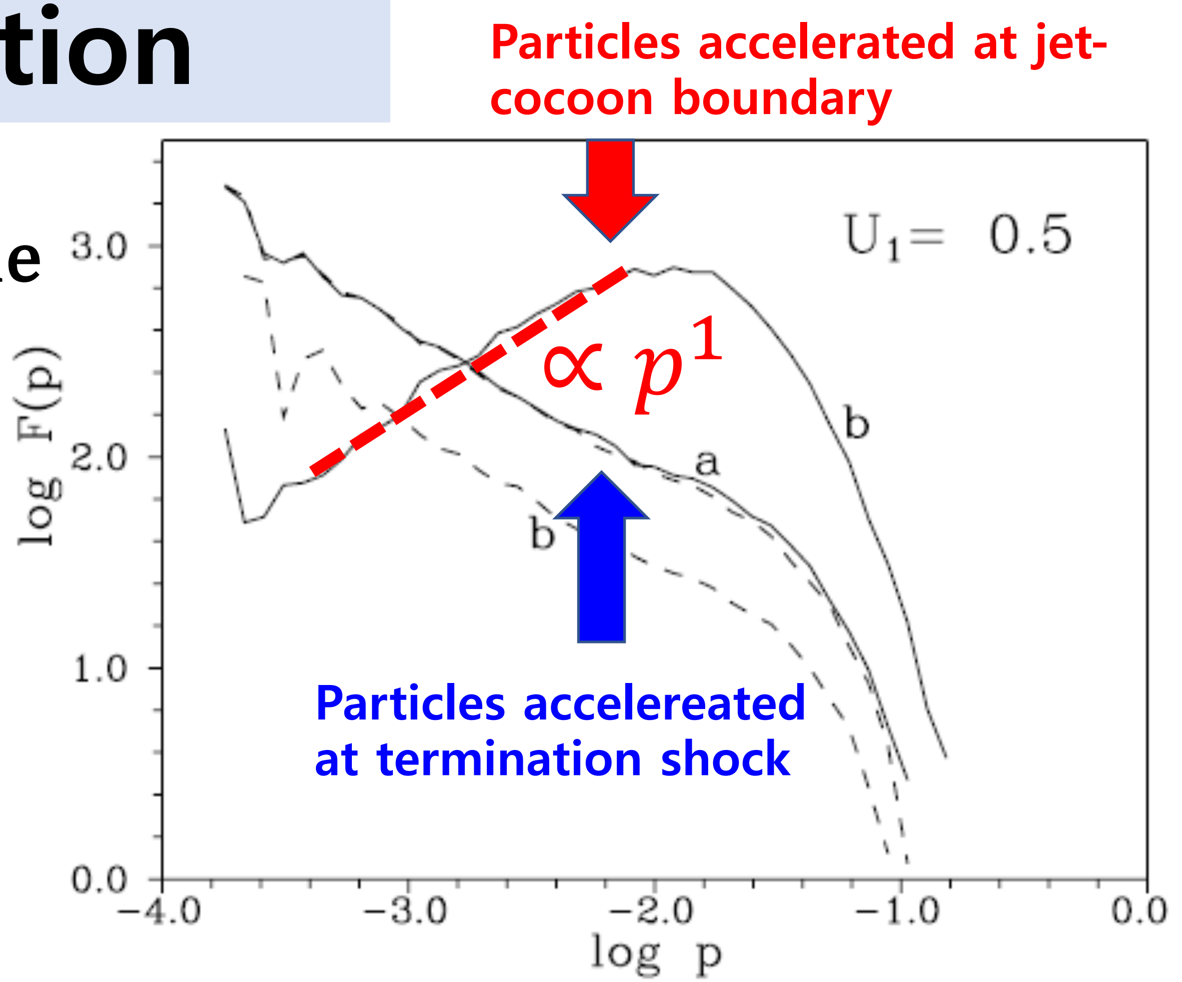

Fig. 5. The particle spectra formed with and without the jet boundary acceleration for $D = 0.97$. Spectra formed due to acceleration both at the jet boundary and at the terminal shock are presented with full lines, while the spectra for the neglected boundary acceleration are given with dashed lines. The results are presented for $R_{esc} = 2.0$, $L_{esc} = 1.0$ and a.) $z_{inj} = 0.0$ or b.) $z_{inj} = -1000.0$.

Discrete shear acceleration

- $\tau(p) = \tau_0(\frac{p}{p_0})^\delta$ **mean scattering time**

✓$\delta = 1$ **(Bohm diffusion)**

- ***Shear acc***

✓$f(p) \propto p^{-(3-\delta)} \propto p^{-2}$

✓$F(p) = \frac{dN(p)}{d \log p} \propto p^1$ for shear acc

- ***Shock acc***

✓$f(p) \propto p^{-4} (r = 4)$

✓$F(p) \propto p^{-1}$ for shock acc

Our result

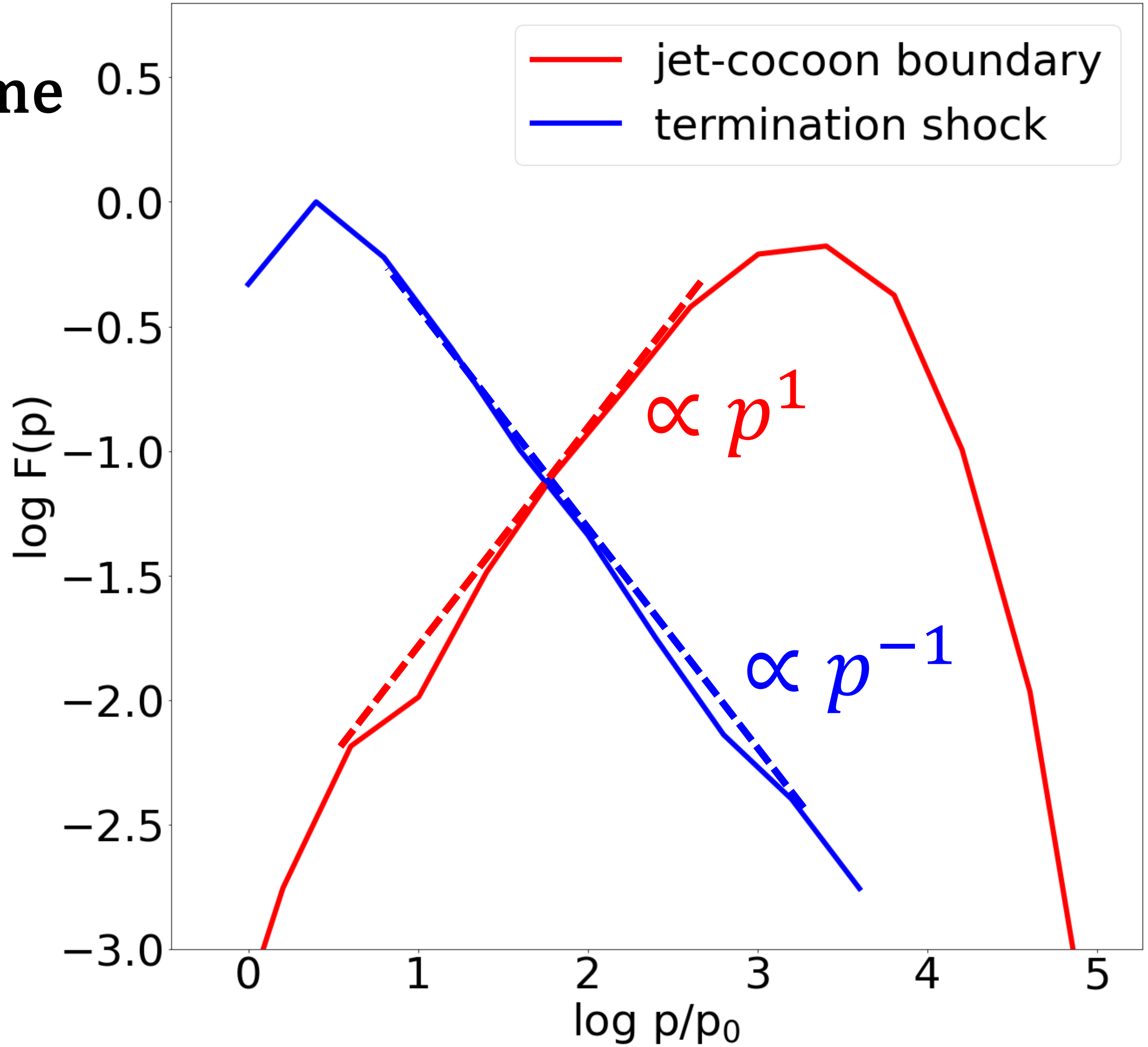

Non-relativistic gradual shear acceleration

Rieger & Duffy 2006

For impulsive injection with p_0 at $t = 0$ $\quad Q\delta(p - p_0)\delta(t).$

Time dependence solution

$$f(p,t) = \frac{Q p_0^{-(\alpha+1)}}{|\alpha|\Gamma\tau_0 t}\left(\frac{p_0}{p}\right)^{(3+\alpha)/2} \exp\left(-\frac{p^{-\alpha}+p_0^{-\alpha}}{\alpha^2\Gamma\tau_0 t}\right) \times I_{|1+3/\alpha|}\left[\frac{2}{\alpha^2\Gamma\tau_0 p_0^{\alpha} t}\left(\frac{p}{p_0}\right)^{-\alpha/2}\right], \qquad (14)$$

where $\tau_c(p) = \tau_0 p^{\alpha}$ $\quad \Gamma = \frac{1}{15}\left(\frac{\partial u_z}{\partial x}\right)^2$

$$\boldsymbol{u} = u_z(x)\boldsymbol{e}_z$$

normalized time, $t' = \frac{t}{t_c}$ where $t_c = \frac{1}{\Gamma\tau_0 p_0}$

- **linear shear** with a constant $\frac{\partial u_z}{\partial x} = 0.001(c/L_0)$
- no. of particles: N_p = 50000
- Injection momentum: p_0/mc=0.9
- In this time range, relativistic effect is not important

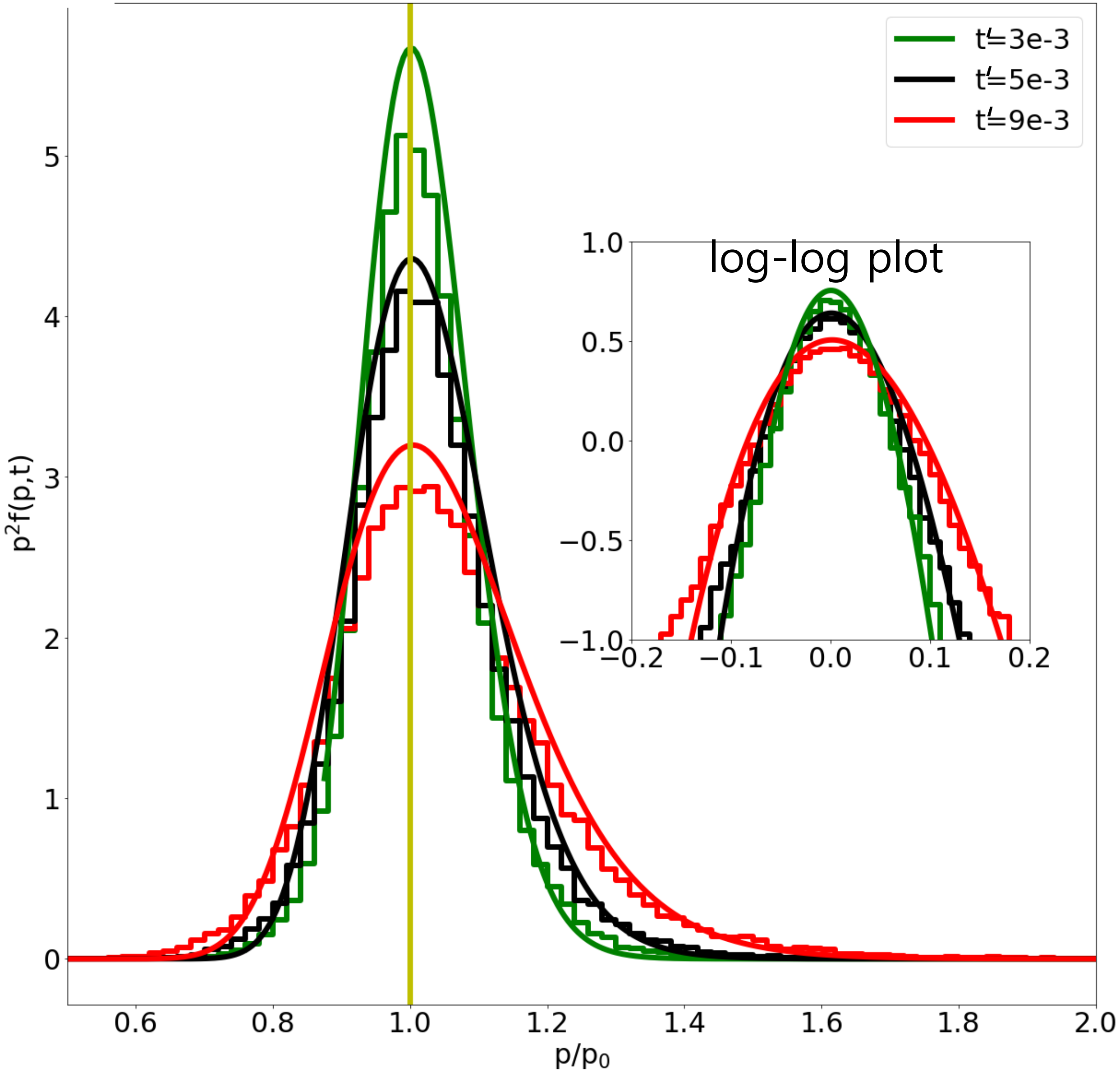

Relativistic Gradual Shear Acceleration

Velocity profile - **Rieger 2019**

$$\beta_z(r) = \beta_0[1 - \tanh(r)^2]$$

where $\beta(r) = u(r)/c$

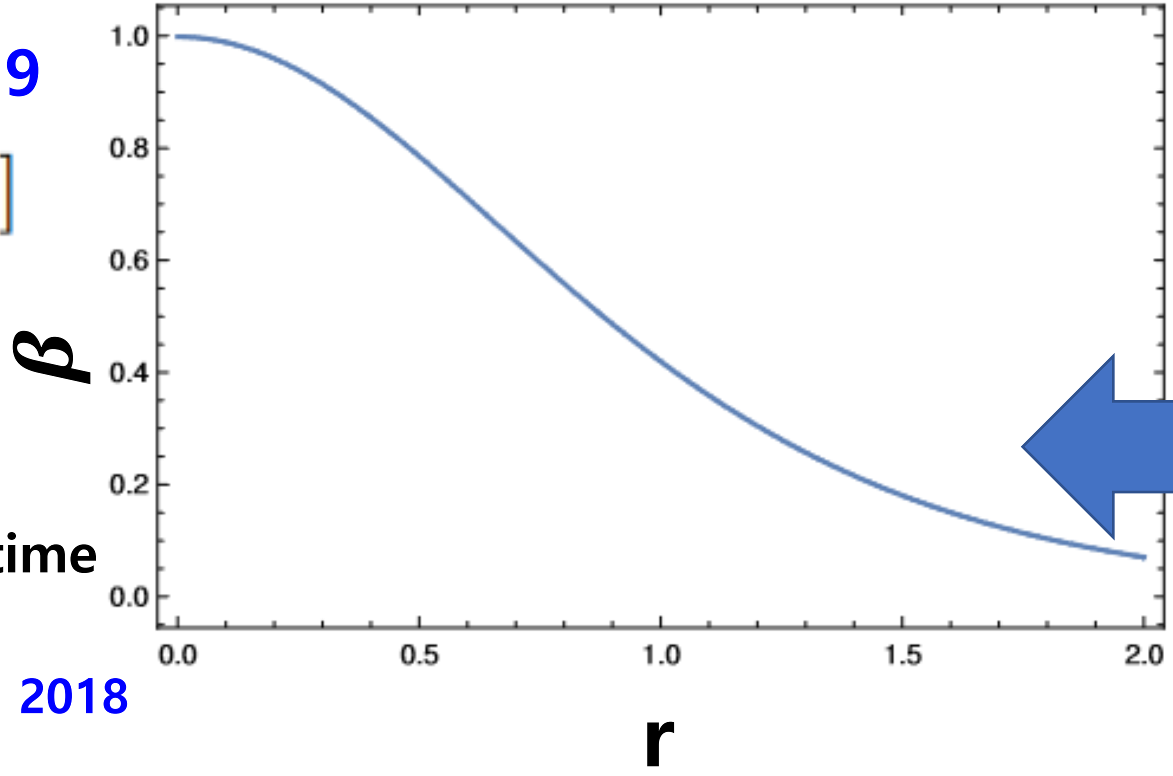

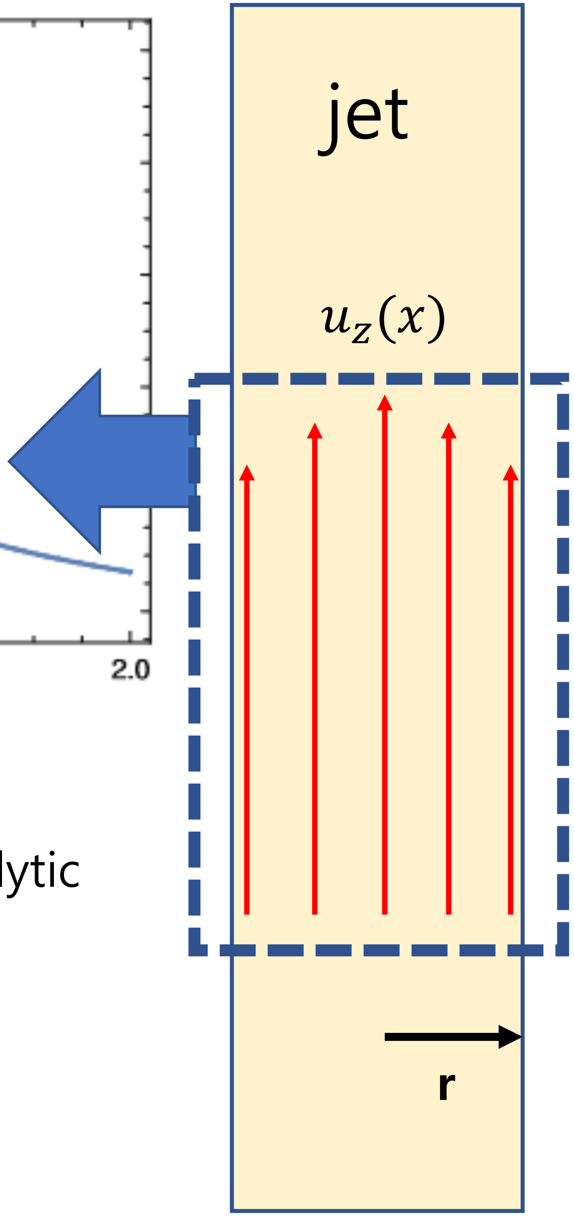

The model of Mean scattering time

$$\tau(r, p) =: \tau_0 \left(\frac{p}{p_0}\right)^{\alpha} \frac{r_1 \xi'(r_1)}{r \xi'(r)},$$ **Webb 2018**

$$\xi(r) = \frac{1}{2} \ln\left(\frac{1+\beta}{1-\beta}\right) = \tanh^{-1}(\beta),$$

Arbitrary function for getting analytic solution

$$\xi'(r) = \frac{-2\beta_0 \tanh(r)\,\mathrm{sech}^2(r)}{1 - \beta_0^2(1 - \tanh^2(r))^2}$$

Simulation Result

Rieger 2019 r: radial distance from the jet center

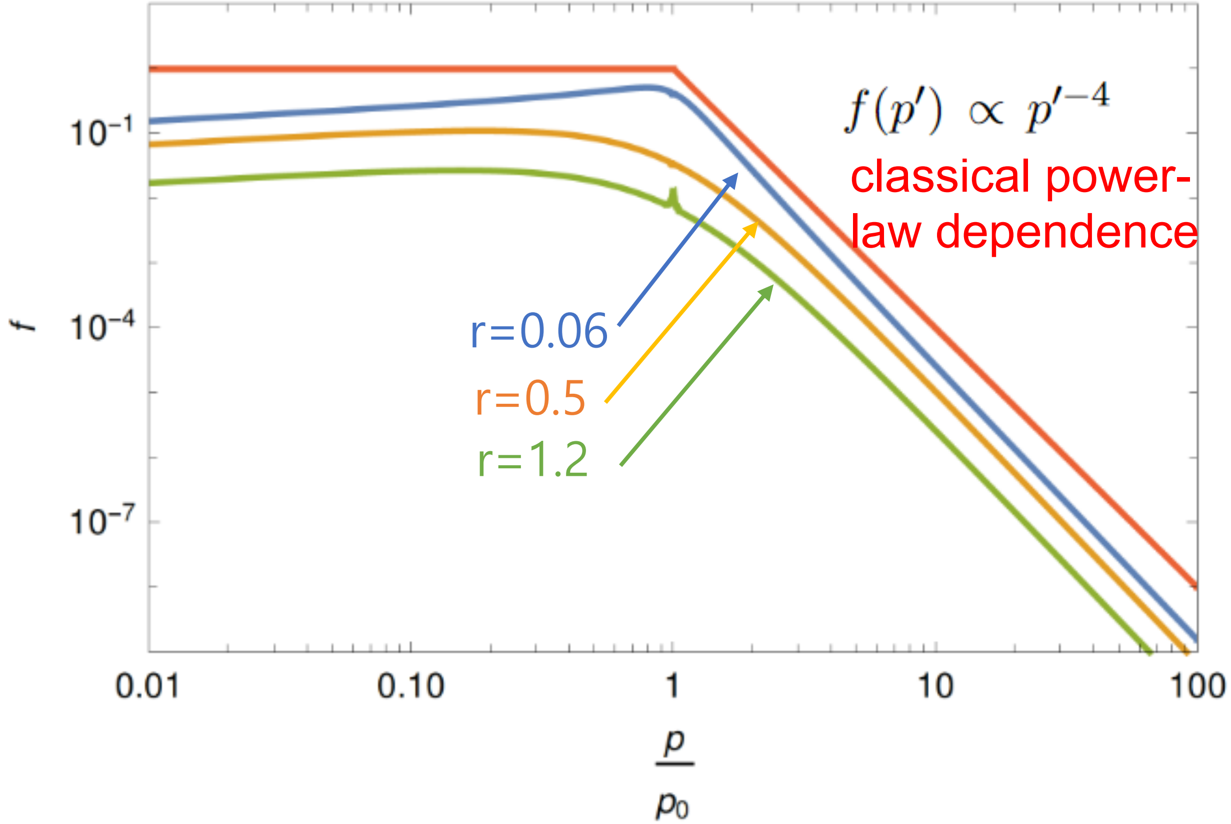

Steady state Solution from relativistic transport eq

$$\nabla_\alpha\left[cu^\alpha f_0 - \kappa\left(g^{\alpha\beta}+u^\alpha u^\beta\right)\left(\frac{\partial f_0}{\partial x^\beta} - \dot{u}_\beta \frac{(p^0)^2}{p'}\frac{\partial f_0}{\partial p'}\right)\right]$$

$$+\frac{1}{p'^2}\frac{\partial}{\partial p'}\left[-\frac{p'^3}{3}c\,\nabla_\beta u^\beta f_0 + p'^3\left(\frac{p'^0}{p'}\right)^2\kappa\,\dot{u}^\beta\left(\frac{\partial f_0}{\partial x^\beta} - \dot{u}_\beta\frac{(p'^0)^2}{p'}\frac{\partial f_0}{\partial p'}\right) - \Gamma\tau p'^4\frac{\partial f_0}{\partial p'}\right] = Q\,,$$

Our result

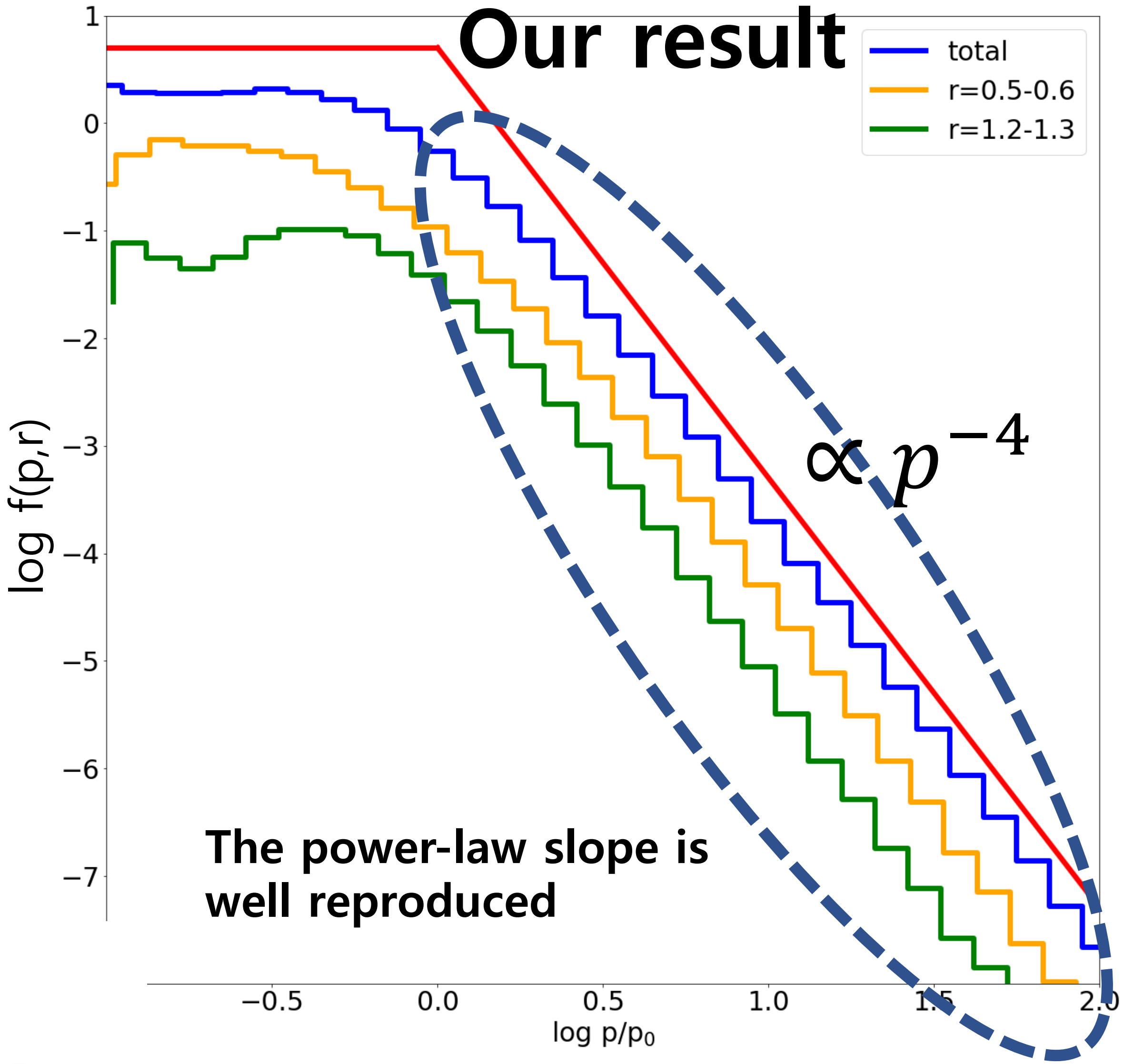

The power-law slope is well reproduced

Monte Carlo simulations for CR transport & acceleration

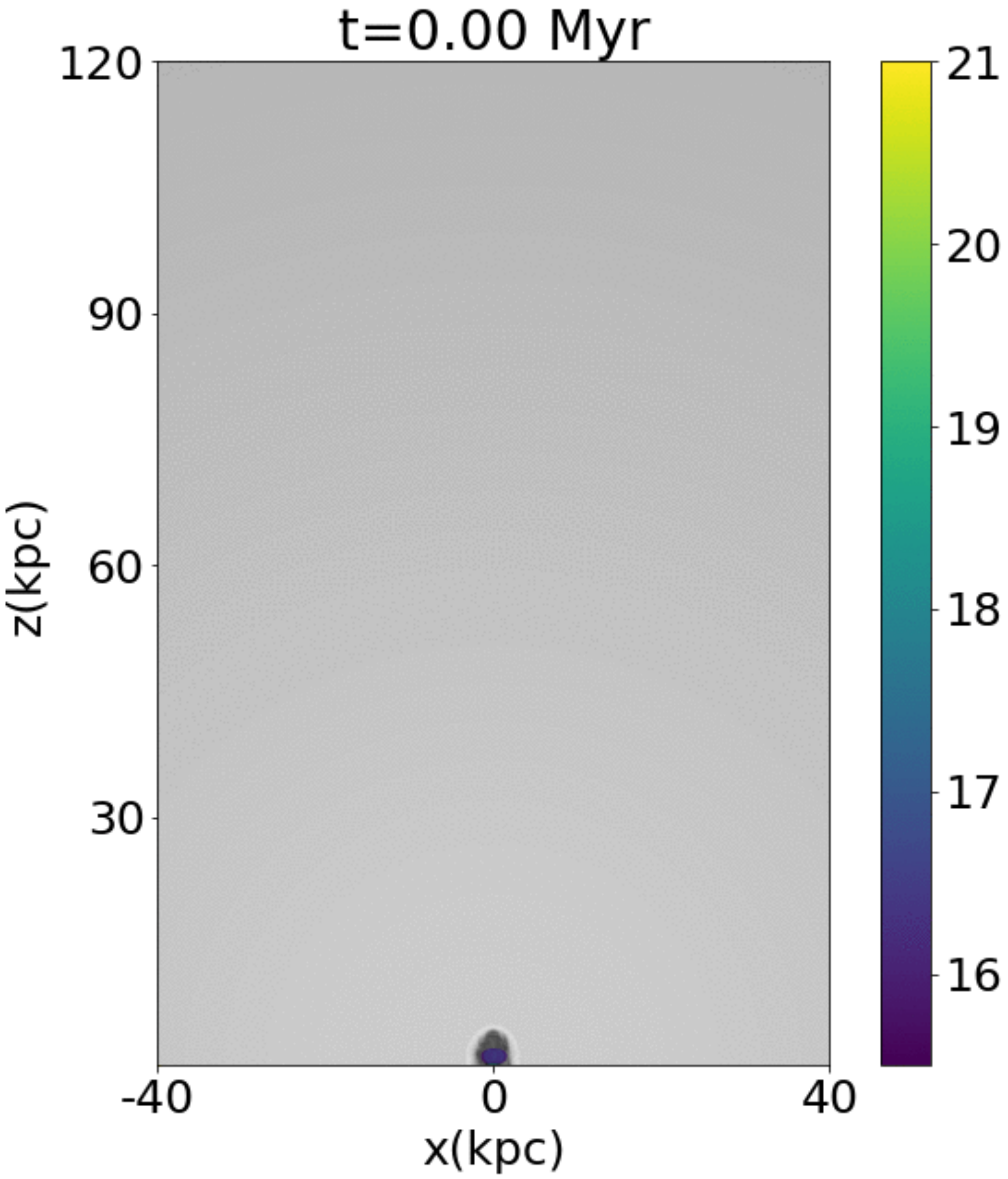

Seo, Ryu, & Kang 2023a, b

- seed CRs are injected from the host galaxy through the jet nozzle with r_j
- Initially, seed CRs : 10TeV-PeV(10^{13-15}eV) with a power-law spectrum $dN/dE \propto E^{-2.7}$.
- Particles are continuously advected and energized in the time-evolving jet flows

Galactic cosmic rays are advected with jet flow

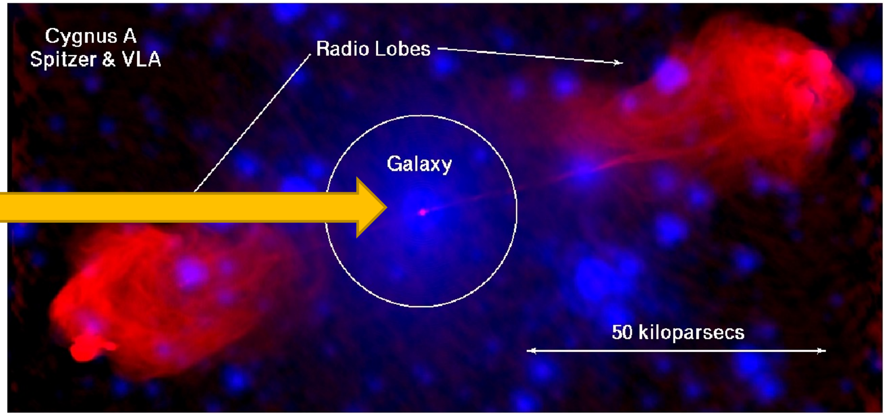

Model Prescriptions for Particle Scattering

mean free path: $\lambda_{mf} \propto E^{\delta}$

$\boldsymbol{E < E_{coh}}$: $E_{coh} = eZ_iBL_0$ (L_0 : characteristic scale of the turbulence)

Kolmogorov scattering

scattered with **MHD waves (with Kolmogorov spectrum)**

➔ $\lambda_{mf} \propto E^{\frac{1}{3}}$

Bohm scattering at shocks

scattered with **self-generated waves** near shocks.

➔ $\lambda_{mf} \propto E$

$\boldsymbol{E > E_{coh}}$: **Bohm scattering**

Comparison model

$\boldsymbol{E > E_{coh}}$: **Non-resonant scattering**

Mean free path is **larger** than **the scale of turbulence**.

➔ $\lambda_{mf} \propto E^2$

Restricted random walk model

Motivation

In a realist jet flow, **magnetic fluctuations** may not be **strong enough** to scatter in a random walk manner for **high energy particles**

$$\delta\theta_{max} = \pi \min[1, \psi \frac{L_0}{\lambda_f}] \quad \begin{cases} \delta\theta_{\max} \ll 1. & \lambda_f(E) \gg L_0 \\ \delta\theta_{\max} \approx \pi. & \lambda_f(E) \ll L_0 \end{cases}$$

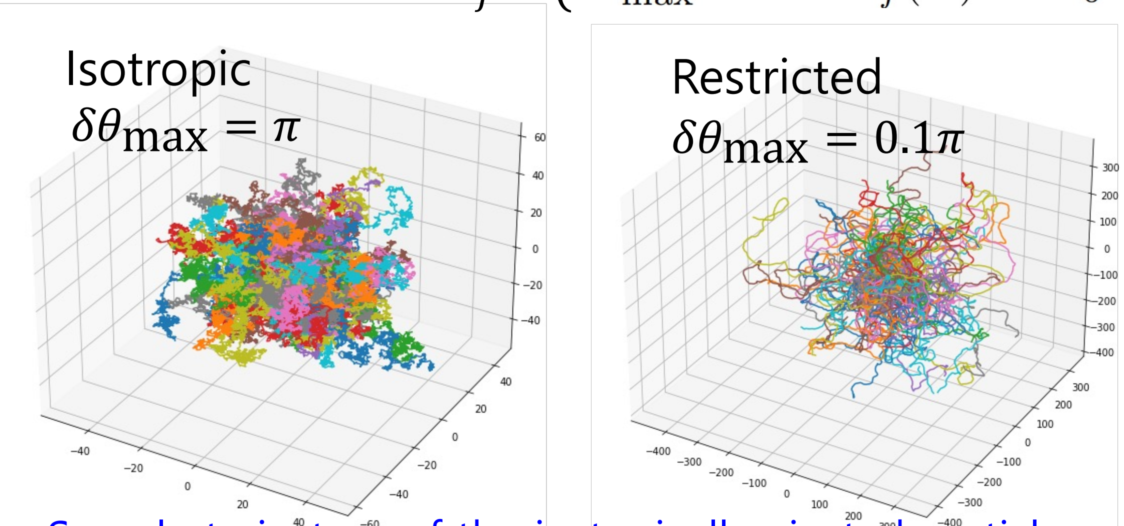

Sample trajectory of the isotopically ejected particles in a restricted random walk model

Model Prescriptions for magnetic field

- **Internal energy model**

$$\frac{B_p^2}{8\pi} = \frac{p}{\beta}.$$

- **Turbulence kinetic energy model**

$$\frac{B_{turb}^2}{8\pi} \approx KE_{turb}$$

- **Shock amplification model**

$$\frac{B_{Bell}^2}{8\pi} \approx \frac{3}{2}\frac{v_s}{c}P_{CR} \approx \frac{3}{2}\frac{v_s}{c}(0.1\rho_1 v_s^2)$$

$$B_{\rm comov} = \max(B_p, B_{\rm turb}, B_{\rm Bell})$$

$B_{\rm obs} \approx \Gamma B_{\rm comov}$ in the computational frame

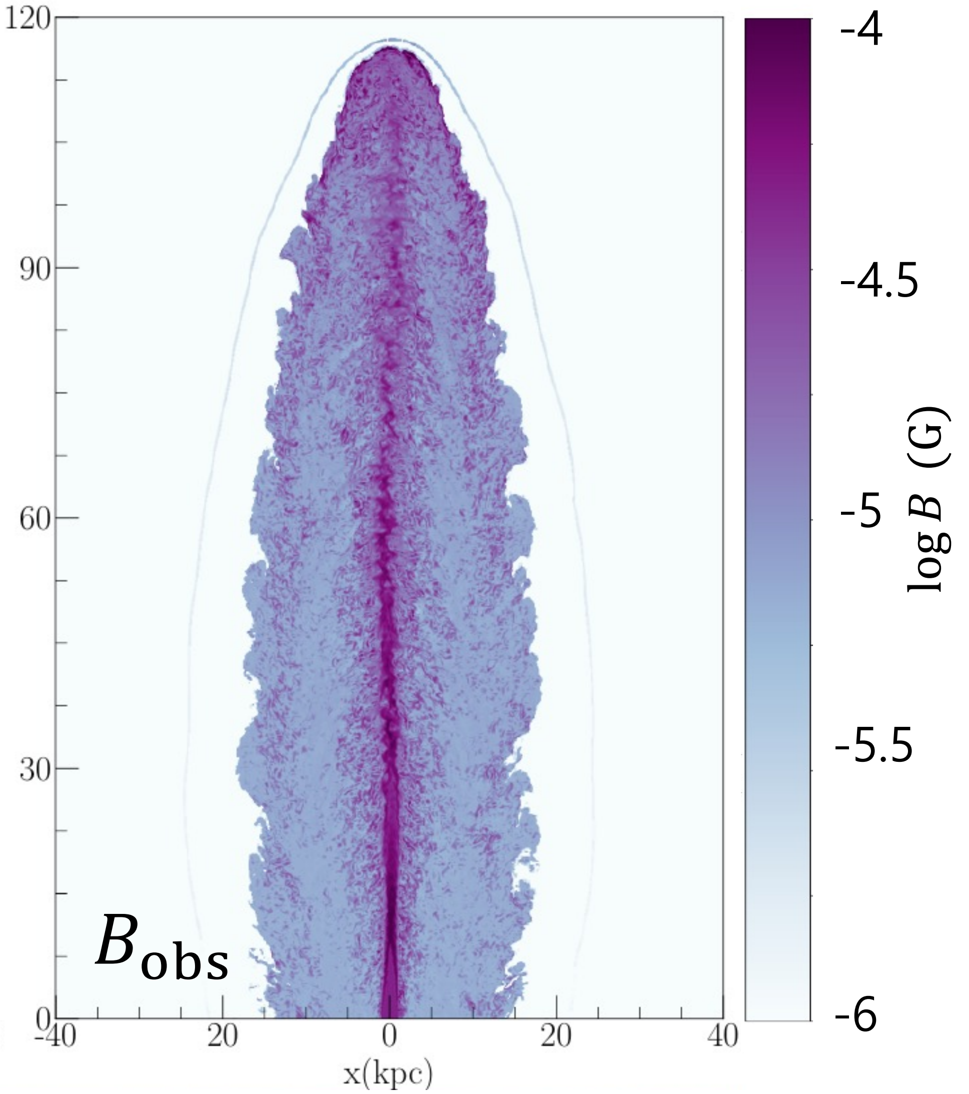

in the computational frame

Jet: B ~ 100μG

Backflow: B ~10μG

ICM: B ~1μG

Three Main Particle Acceleration Mechanisms

Diffusive Shock Acceleration

Shock Mach no.

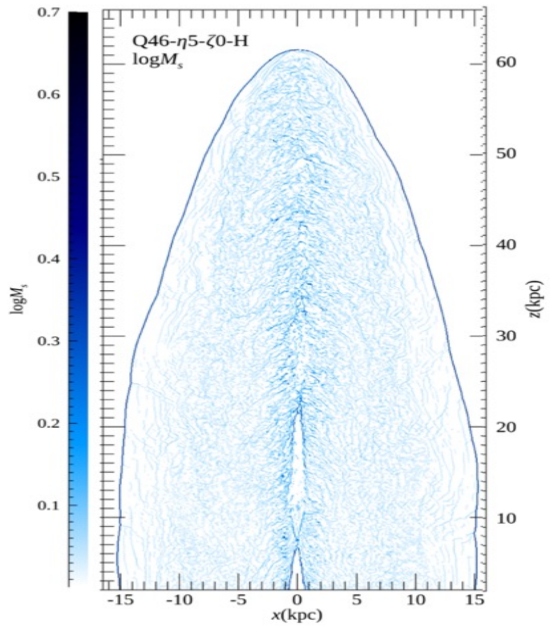

steep spectrum

$dN/dE \propto E^{-\sigma} \quad \sigma = (\chi+2)/(\chi-1)$

$\chi = \rho_2/\rho_1$ compression ratio of the shock

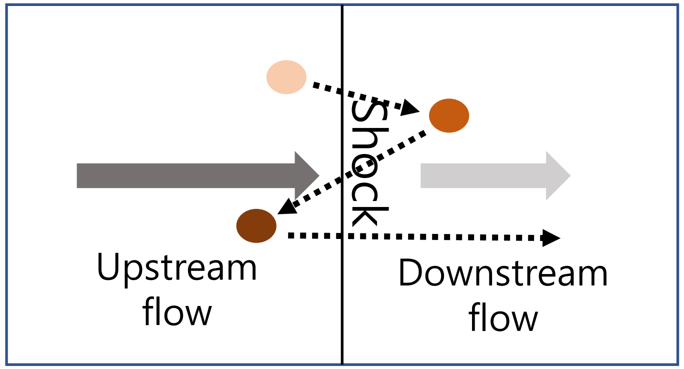

Shear Acceleration

Relativistic shear coefficient

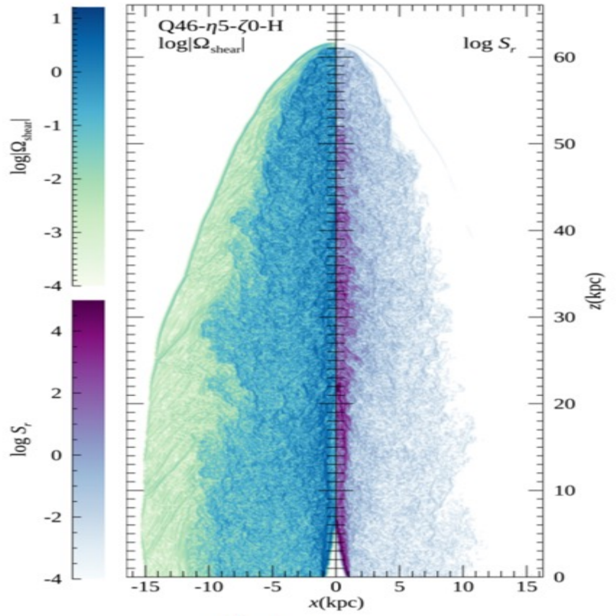

$\mathcal{S}_r = \frac{\Gamma_v^4}{15}(\frac{\partial v_z}{\partial r})^2,$

flat spectrum

$dN/dE = 4\pi p^2 f(p) \propto E^{-1+\delta}. \quad \tau(p) \propto p^{\delta}$

$dN/dE \propto E^0$ for the Bohm diffusion

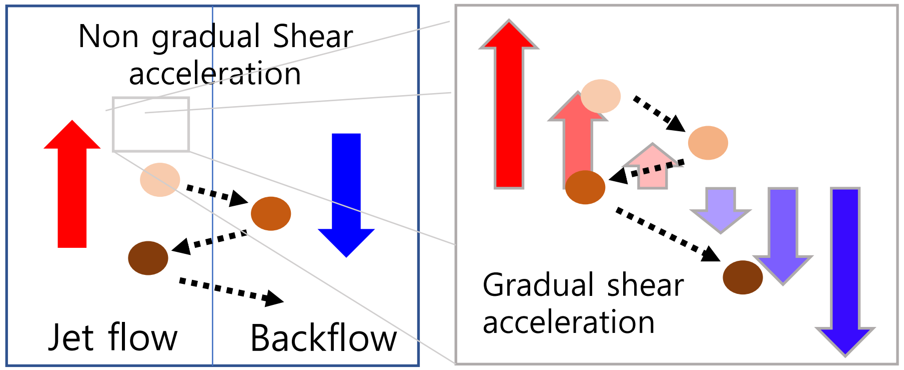

Turbulent Acceleration

Vorticity = turbulence

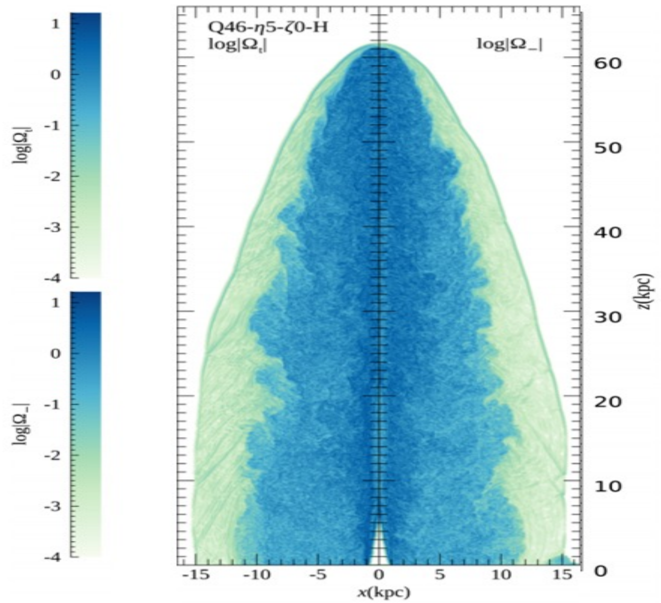

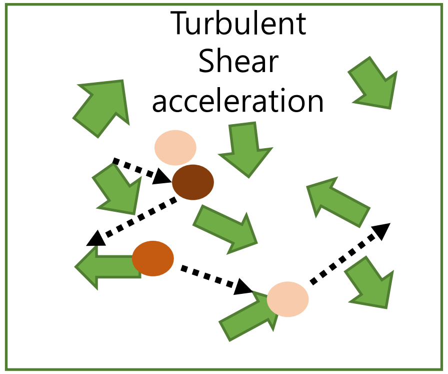

Contribution of acceleration process (AP):
acceleration time scales

DSA (shock)

$$t_{\mathrm{DSA}} = 3.52\times10^{3}\mathrm{yr}\,\frac{\chi(\chi+1)}{\chi-1}\left(\frac{v_s}{c}\right)^{-2}\left(\frac{E}{\mathrm{EeV}}\right)\left(\frac{B}{1\mu\mathrm{G}}\right)^{-1}$$

Drury 1983

Gradual Shear Acc

$$t_{\mathrm{GSA}} = 4.90\times10^{4}\mathrm{yr}\,\frac{1}{(4+\alpha)\gamma^4}\left(\frac{\Omega_{shear}}{c/r_j}\right)^{-2}\left(\frac{\lambda_f(p)}{\mathrm{kpc}}\right)^{-1}$$

Webb et al 2018

Turbulent Shear Acc

$$t_{\mathrm{TSA}} = 2.88\times10^{4}\mathrm{yr}\,\left(\frac{L_0/\gamma}{1\mathrm{kpc}}\right)^{\frac{2}{3}}\left(\frac{|v_{tur}|}{c}\right)^{-2}\left(\frac{\lambda_f(p)}{\mathrm{kpc}}\right)^{1/3}$$

Ohira 2013

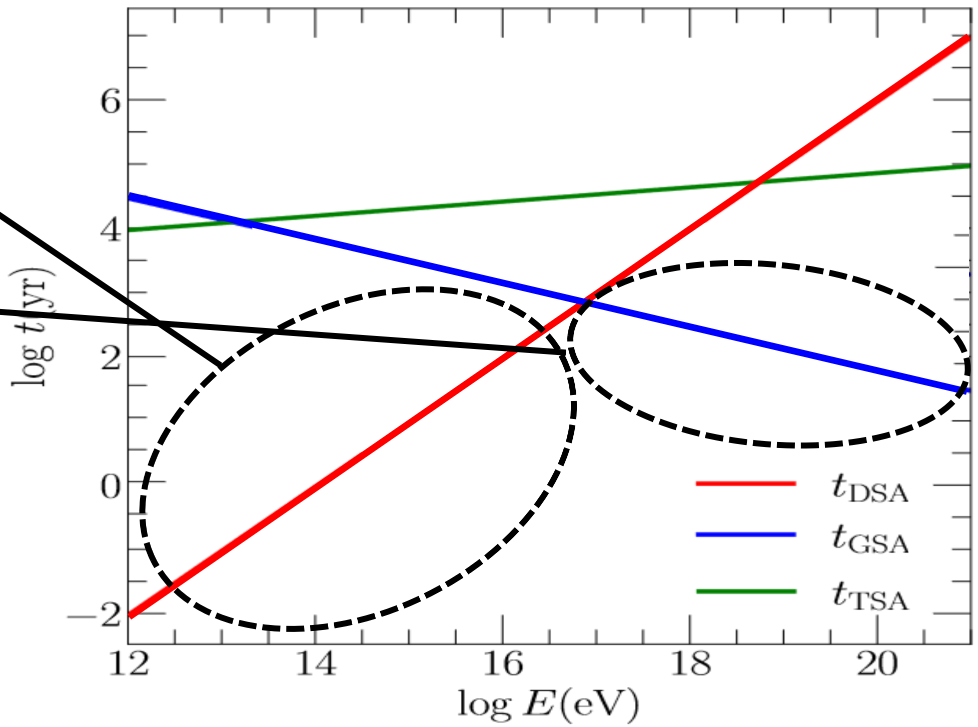

Acceleration time scales for different processes in typical jet flows

$$\varepsilon_{\mathrm{AP}}(E) = \frac{\sum_{\log E}^{\log E + d\log E} \xi_{\mathrm{AP}}\Delta E}{\sum_{\log E}^{\log E + d\log E} \Delta E}$$

The relative contribution of acceleration process (AP) in the bin $[\log E, \log E + d\log E]$

$\xi_{\mathrm{AP}} = t_{\mathrm{AP}}^{-1} / \sum_{\mathrm{AP}} t_{\mathrm{AP}}^{-1}$: weight function of acceleration time scale

Relative importance of three acceleration processes

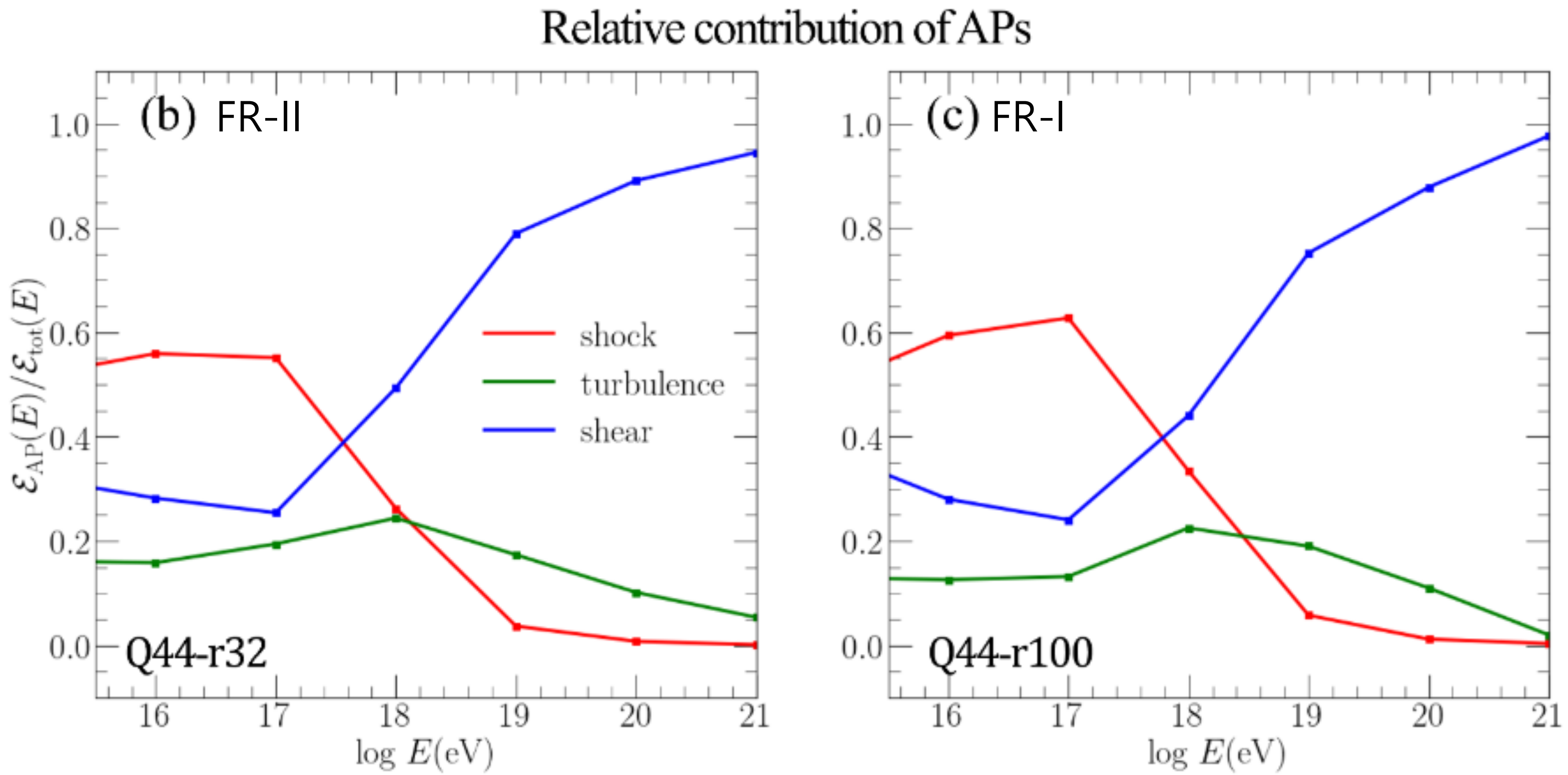

- **Shear acceleration** is the primary mechanism to generate UHECRs of $E >$ ~EeV; regardless of whether relativistic or mildly relativistic jet flows.
- **Shock acceleration** is the main process for the acceleration of particles with $E <$ ~EeV.
- **Turbulence acceleration** plays a secondary role.

Energy spectrum of accelerated particles: $\frac{dN(t)}{dE}$

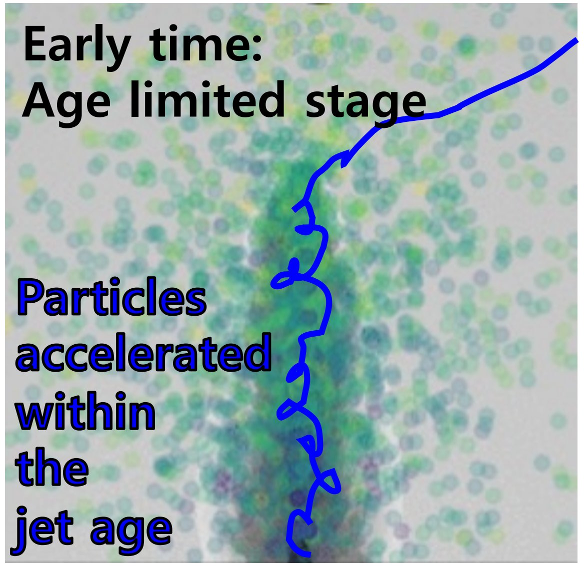

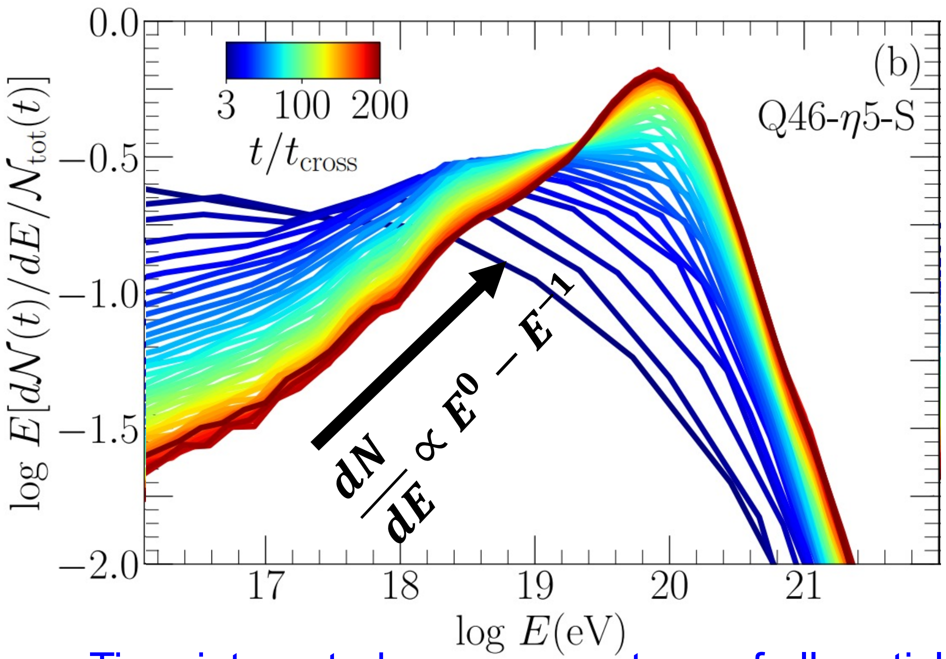

Time-integrated energy spectrum of all particles escaping from the system up to a given time

- Escaped particles have a **power-law** spectrum with a cutoff, E_{max}
- For $E < E_{max}$, the power-law is $\frac{dN}{dE} \propto E^0 - E^{-1}$, depending on time.
- In the **early stage**, maximum energy is determined by the **age of the jet**, while in the **late stage** the particle confinement by the **cocoon width** becomes important, the spectrum approaches to a **time-asymptotic form.**

Particle escape: Hillas condition

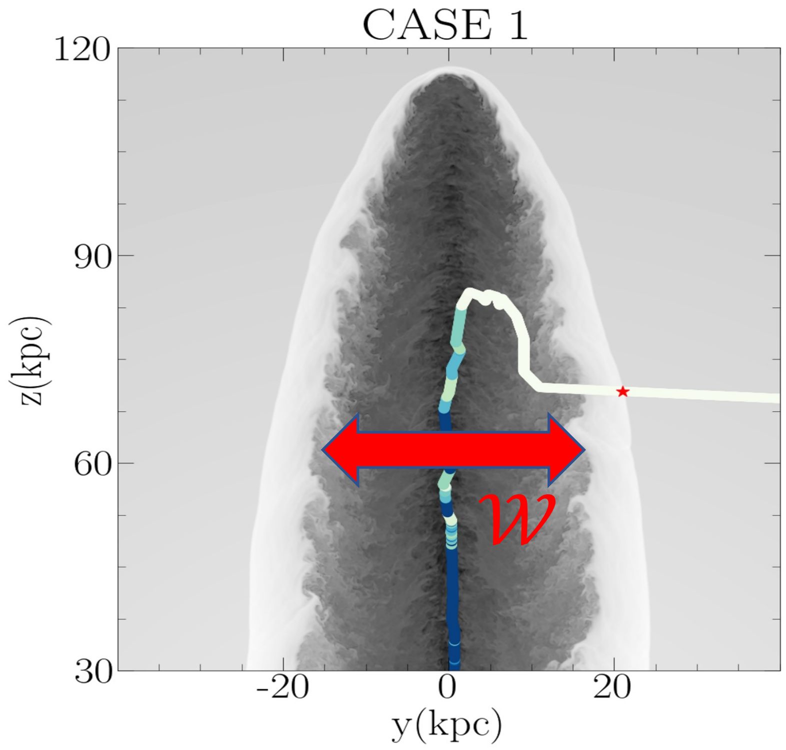

Particles gradually gain energy, and when their **mean free path is larger than cocoon radius**, $\lambda_f > \mathcal{W}/2$, they can escape the cocoon.

This process determine the **maximum energy** of the energy spectrum.

$$\lambda_f(E) \sim \mathcal{W}/2$$

$$\begin{aligned} E_{\max} &\approx E_{H,L_0}\left(\frac{\mathcal{W}}{2L_0}\right) \\ &\approx 0.9\ \mathrm{EeV}\cdot Z_i \boxed{\left(\frac{B}{1\ \mu\mathrm{G}}\right)\left(\frac{r_j}{1\ \mathrm{kpc}}\right)\left(\frac{\mathcal{W}}{2r_j}\right)} \end{aligned}$$

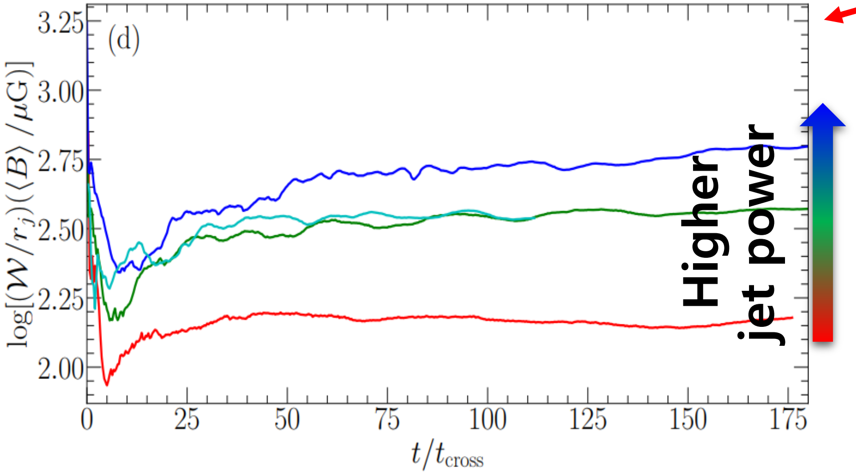

E_{max} is governed by **jet power:**
$E_{max} \propto Q_j^{1/3}$.

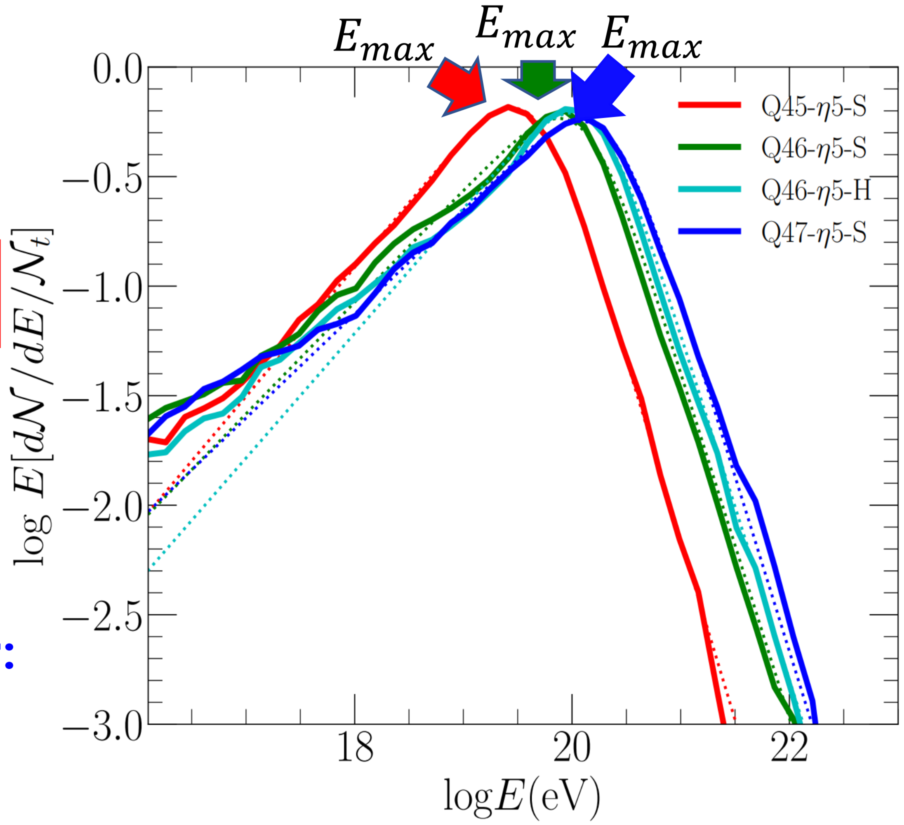

Time-asymptotic energy spectrum

Particle escape : acceleration of particles re-entering the jet-spine flow

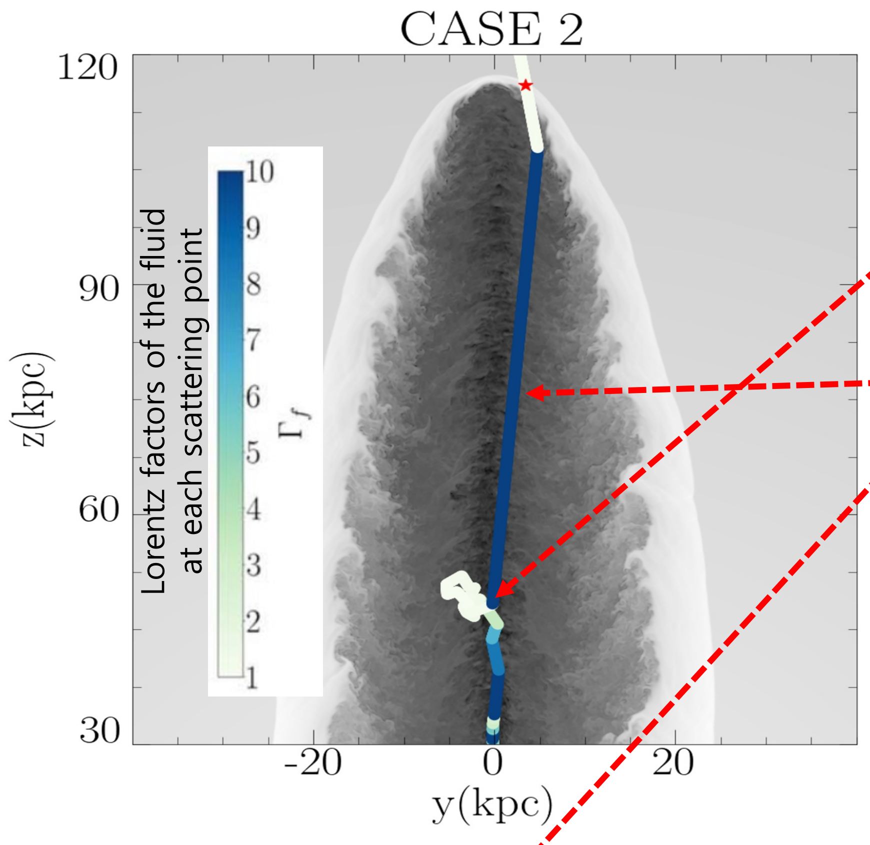

When the particle **re-enters the jet-spine flow**,

It gains huge energy ($\left\langle\frac{\Delta E}{E}\right\rangle \sim \Gamma^2$).

Hence, It has **large mean free path**.

Therefore, they can escape cocoons with a **large longitude angle**.

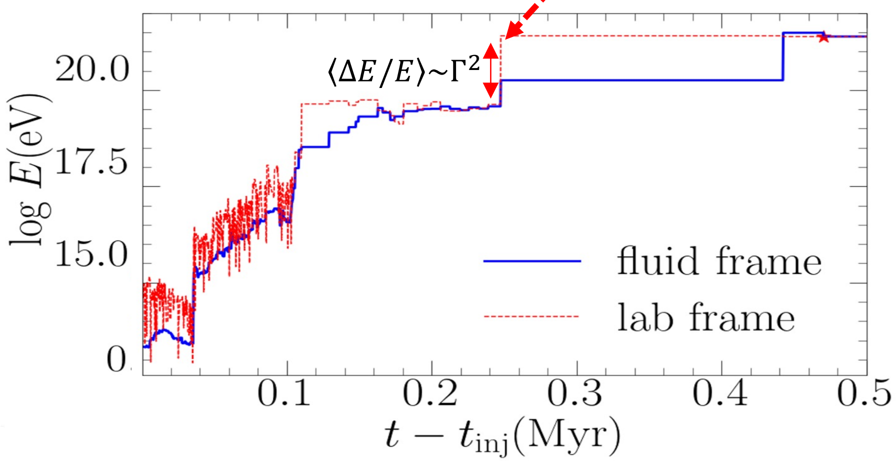

Confinement condition for cylinder

$$dN/d\phi = r^2 \sin\phi \, d\theta$$

$$\lambda = \frac{r}{\cos\phi}$$

$$\frac{dN}{d\phi} = r\sin\phi / cos^2\phi$$

$$dN/d\lambda = \frac{r cos^2\phi}{2\pi} \propto \lambda^{-2}$$

$$\left(\frac{dN}{d\log E} \propto E^{-1}\right)$$

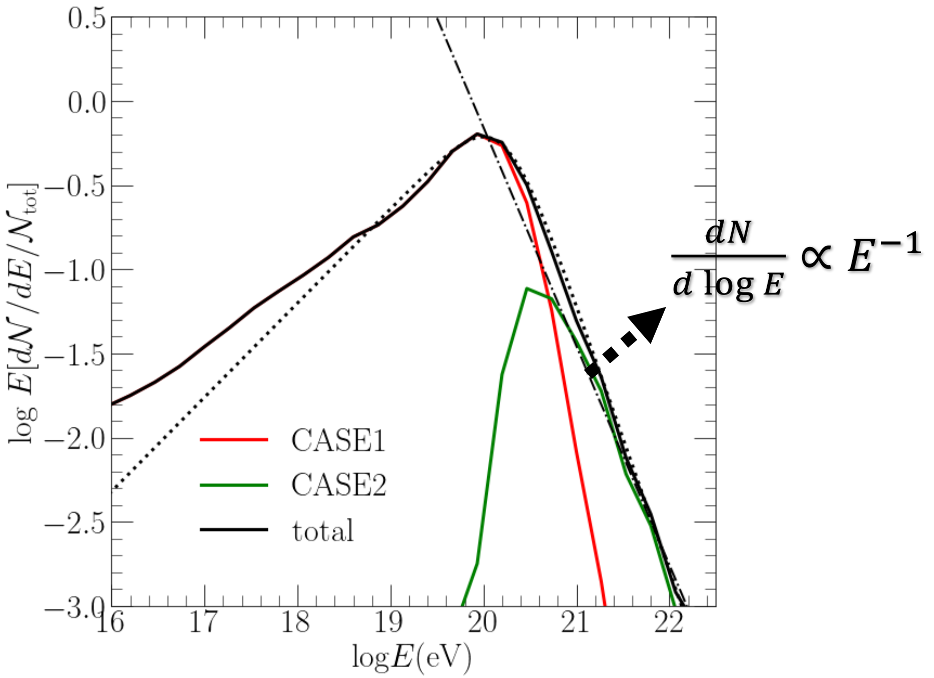

Energy spectrum of escaping particles: double power-law

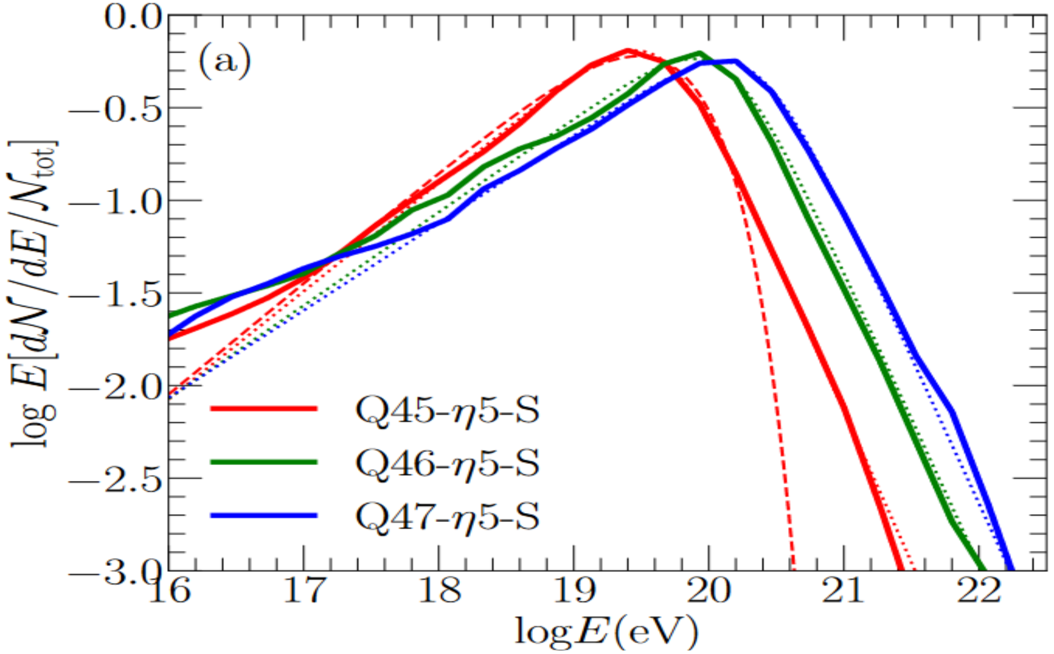

$$\frac{E\,dN}{dE} \propto \left(\left(\frac{E}{E_{\rm break}}\right)^{-a} + \left(\frac{E}{E_{\rm break}}\right)^{b}\right)^{-1}$$

Model name	a	b	$E_{\rm break}$(eV)	$E_{\rm max}$(eV)[1]
Q45-η5-S	0.59	1.64	4.5E19	7.0E19
Q46-η5-S	0.51	1.58	1.3E20	1.6E20
Q47-η5-S	0.47	1.60	2.2E20	2.8E20

$$E_{break} \sim E_{max}$$

Dependences on different modeling are only marginal.

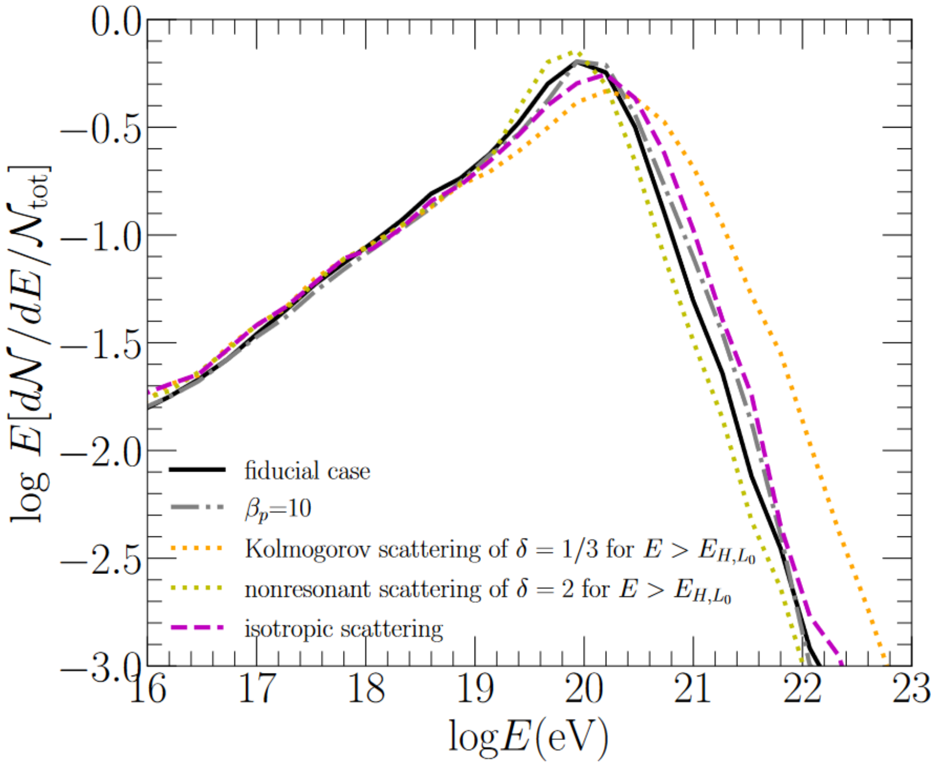

Energy spectrum of escaping particles with different modeling for magnetic field and MC simulation

The characteristic of the energy spectrum :

1) E_{max} : governed by the jet power
2) $E < E_{max}$: harder than E^{-2} due to shear acceleration
3) $E > E_{max}$: controlled by the cocoon confinement

Energy spectrum of escaping particles

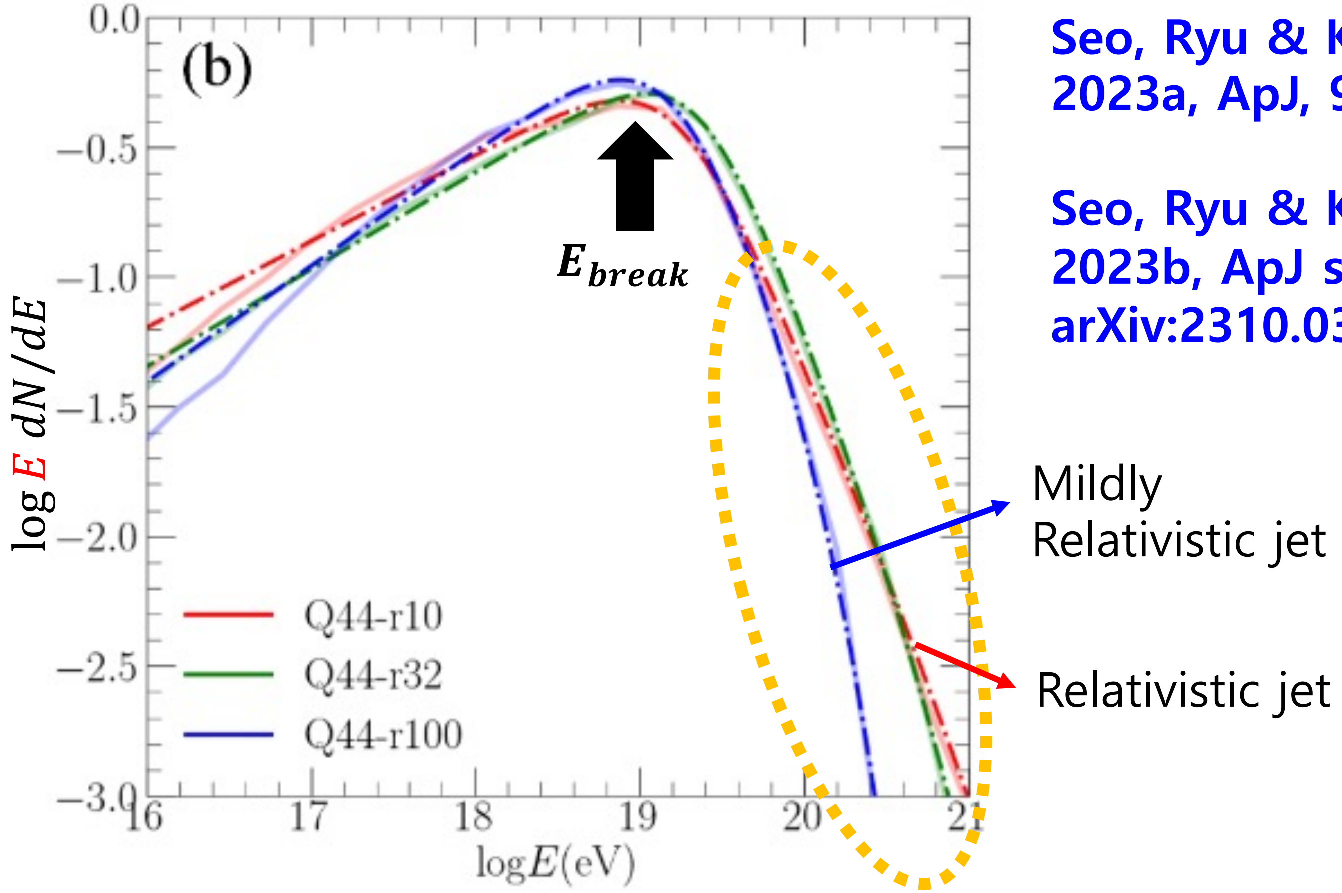

Seo, Ryu & Kang, 2023a, ApJ, 944, 2

Seo, Ryu & Kang, 2023b, ApJ submitted, arXiv:2310.03231

➔ double power-law with extended exponential cutoff

$$\frac{dN}{dE} \propto \left(\left(\frac{E}{Z_i E_{break}}\right)^{-a} + \left(\frac{E}{Z_i E_{break}}\right)^{-b}\right)^{-1} \times \exp\left(-\frac{E}{Z_i E_{break}\Gamma^2}\right)$$

- $E < E_{break}$: $dN/dE \propto E^{-0.5}$ due to shear acceleration
- $E > E_{break}$: $dN/dE \propto E^{-2.6}$ controlled by the elongated cocoon confinement

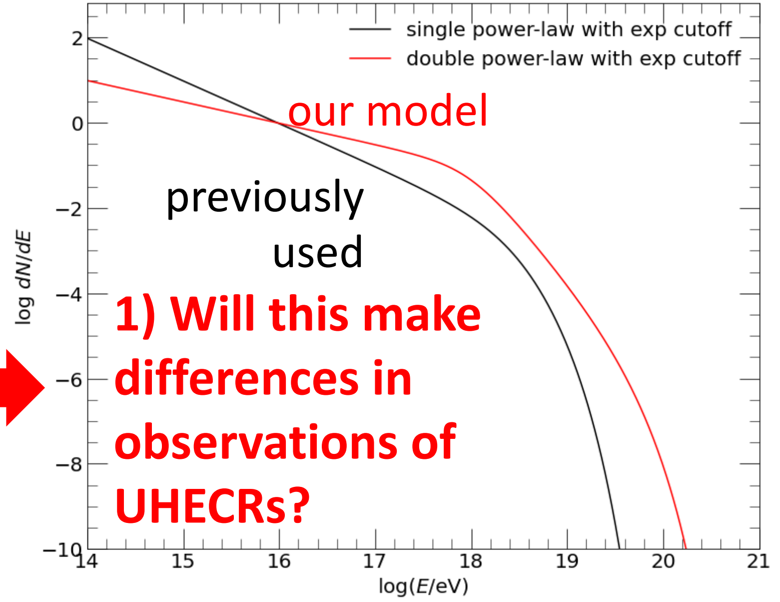

1) Will this make differences in observations of UHECRs?

- E_{break}: **depends on the jet power**
- Exponential cutoff at $E_{break}\Gamma^2$: Γ is the Lorentz factor of the jet spine

2) Will our model for UHECRs help resolve the differences between Auger & TA observations?

Step 4. Estimation of observed flux and mass composition through UHECRs propagation simulation.

Simulations for energy spectrum of UHECRs arriving at Earth

Seo et al. 2023 in preparation

In **CRPropa3** simulations, we include the following modules:

- photo-pion Production
- photodisintegration
- electron pair production
  by CMB and extragalactic background light (Gilmore et al. 2012)
- redshift (adiabatic energy loss)

Modeling the contribution from radio galaxies (RGs)

- The total energy of escaped CR particles is proportional to the luminosity of galaxies.

Comparison of UHECRs coming from relativistic and mildly relativistic jet

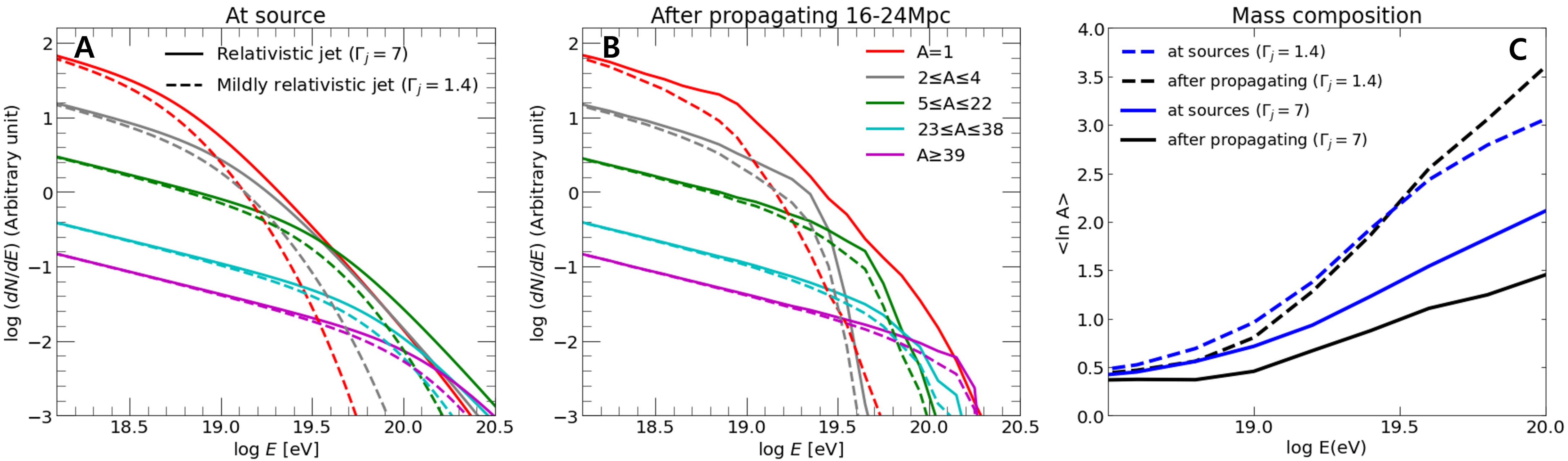

UHECR source spectrum

$$\frac{dN}{dE} \propto \left(\left(\frac{E}{Z_i E_{break}}\right)^{-s_1} + \left(\frac{E}{Z_i E_{break}}\right)^{-s_2}\right)^{-1} \times \exp\left(-\frac{E}{Z_i E_{break} \Gamma^2}\right)$$

→ **Relativistic jet generates more UHECRs flux at the high energy, E>10EeV**

→ **UHECRs from relativistic jets have a smaller mass composition**

$Q_{jet} = 2.5\times10^{43}$ erg/s, $E_{break} = 5.0$EeV

$s_1 = -0.6, s_2 = -2.6$

Can the differences of Auger and TA observations be explained with our UHECR source model?

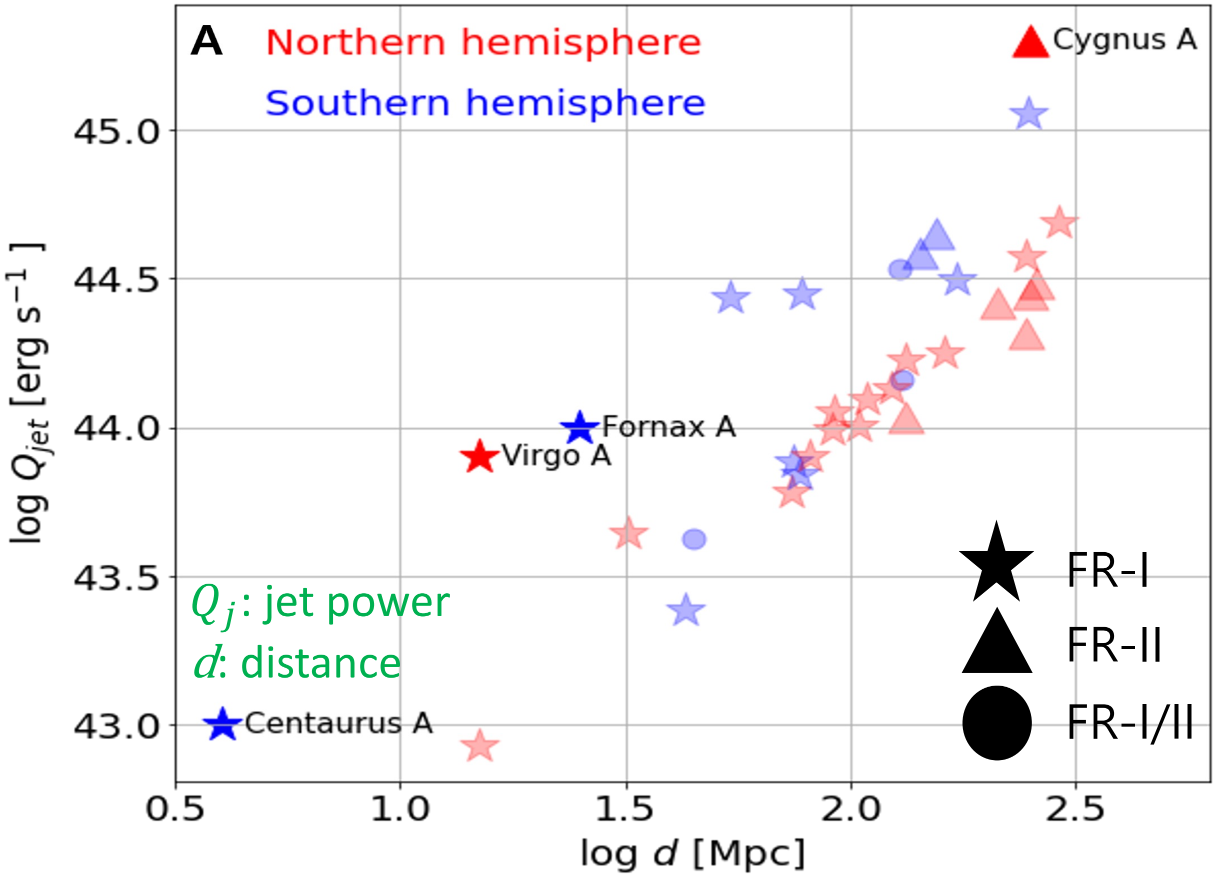

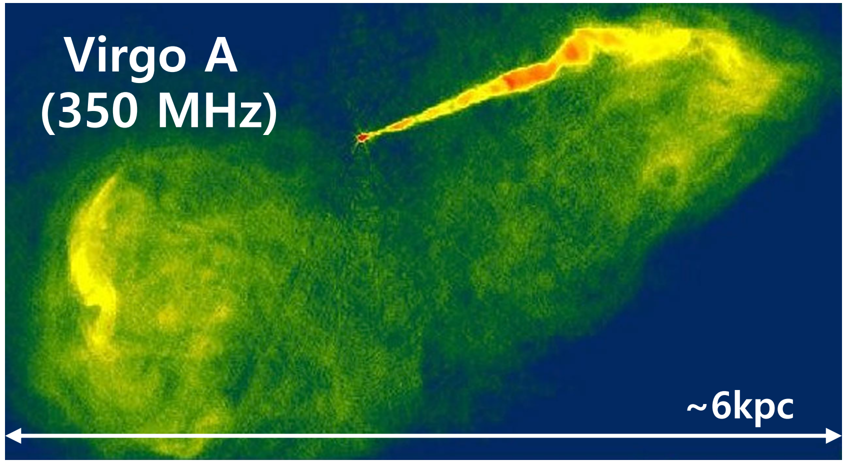

TA: dominant source of northern sky → Virgo A

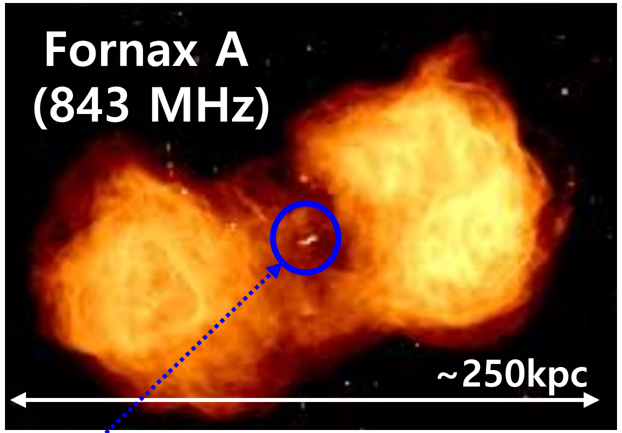

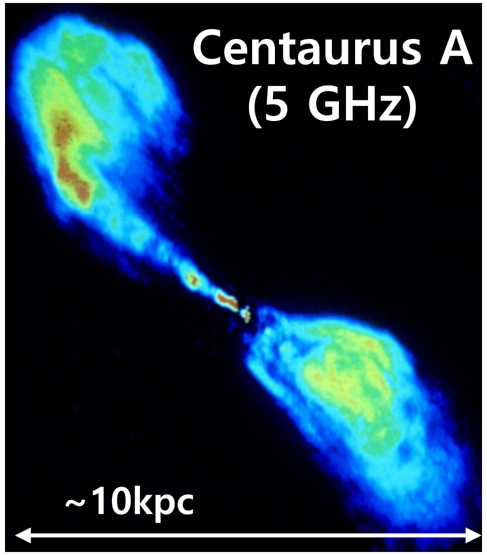

Virgo A shows a relativistic jet that looks single-sided & relativistically boosted ($\Gamma_{jet} \gtrsim 6$, e.g., Biretta et al 1999)

Fornax A shows well developed cocoons, but inner jets implying recent low-power jet activity (e.g., Geldzahler & Fomalont 1984; Maccagni et al. 2020)

Centaurus A looks one-sided, but may not be powerful enough ($\Gamma_{jet} \sim 1.2-2$ e.g., Wykes et al. 2019; Snioset al. 2019b1999)

Auger: important sources of southern sky → Centaurus A & Fornax A

Modeling of Auger and TA observations with our UHECR source model

See also Eichmann et al. 2018 & 2022

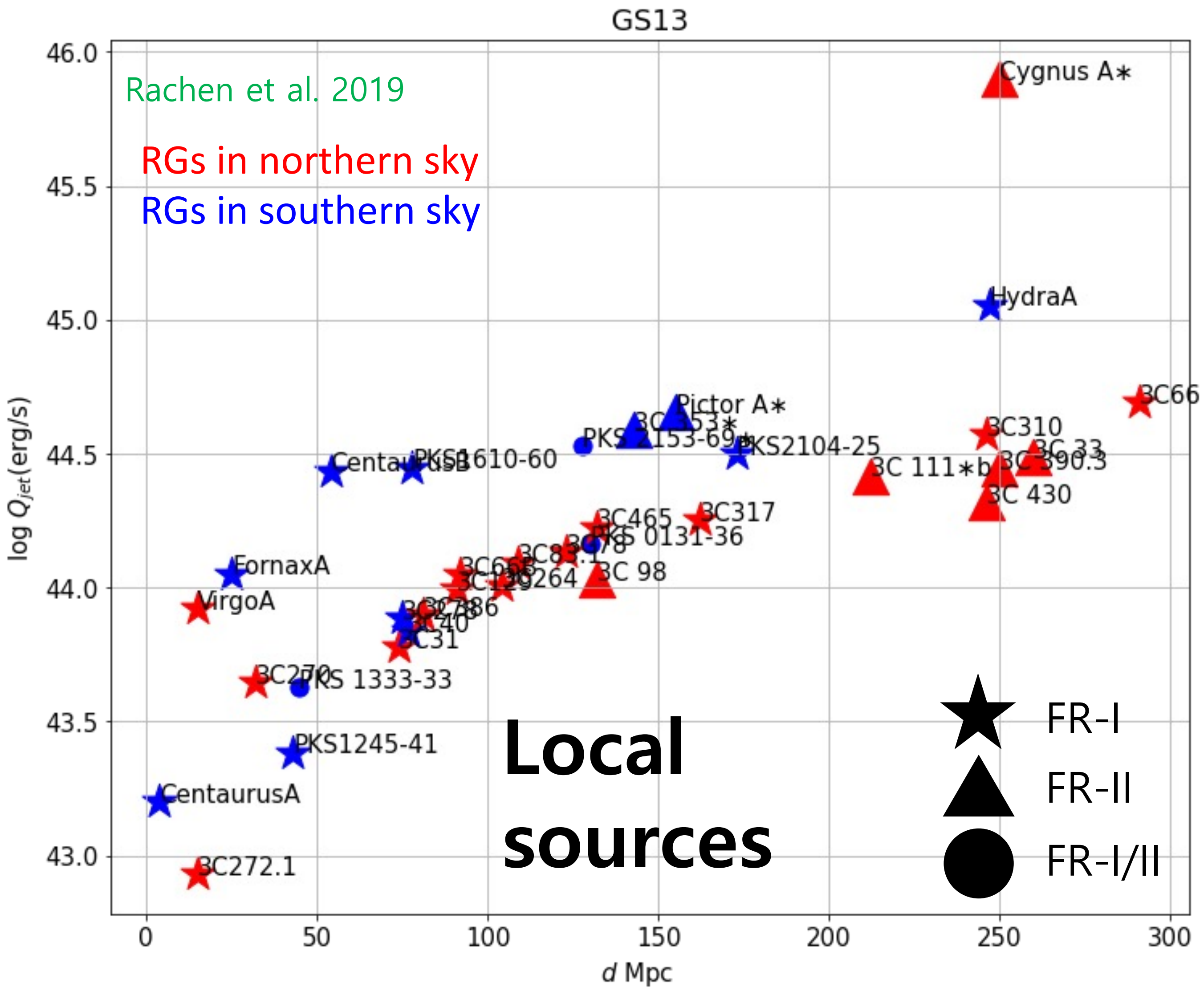

For local RG population

Virgo A & FR II RGs → collimated jets

FR I RGs → decollimated jets

Cosmological RG population in 0.1<z<1

- redshift distribution from Mingo et al 2019
- jet power distribution from Hardcastle et al 2019

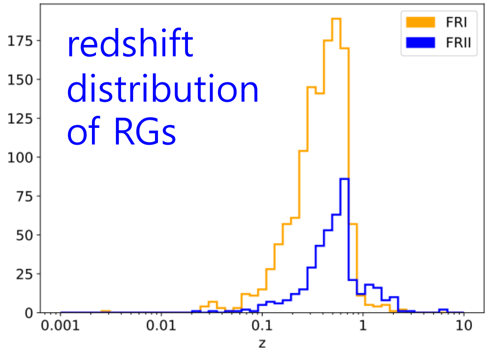

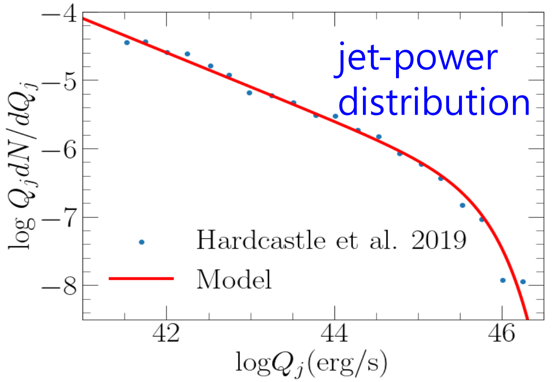

UHECR source spectrum

$$\frac{dN}{dE} \propto \left(\left(\frac{E}{Z_i E_{break}} \right)^{-a} + \left(\frac{E}{Z_i E_{break}} \right)^{-b} \right)^{-1} \times \exp\left(- \frac{E}{Z_i E_{break} \Gamma^2} \right)$$

Flux and mass composition of UHECRs from radio galaxy jets

- Assuming that Virgo A is a relativistic jet with $\Gamma \sim$ several, it could contribute a substantial fraction of the UHECRs observed at TA.
- UHECRs from Virgo A reduce the mass composition observed at TA.
- Whether the jet of major sources is relativistic or mildly relativistic is the key to explaining the discrepancy.

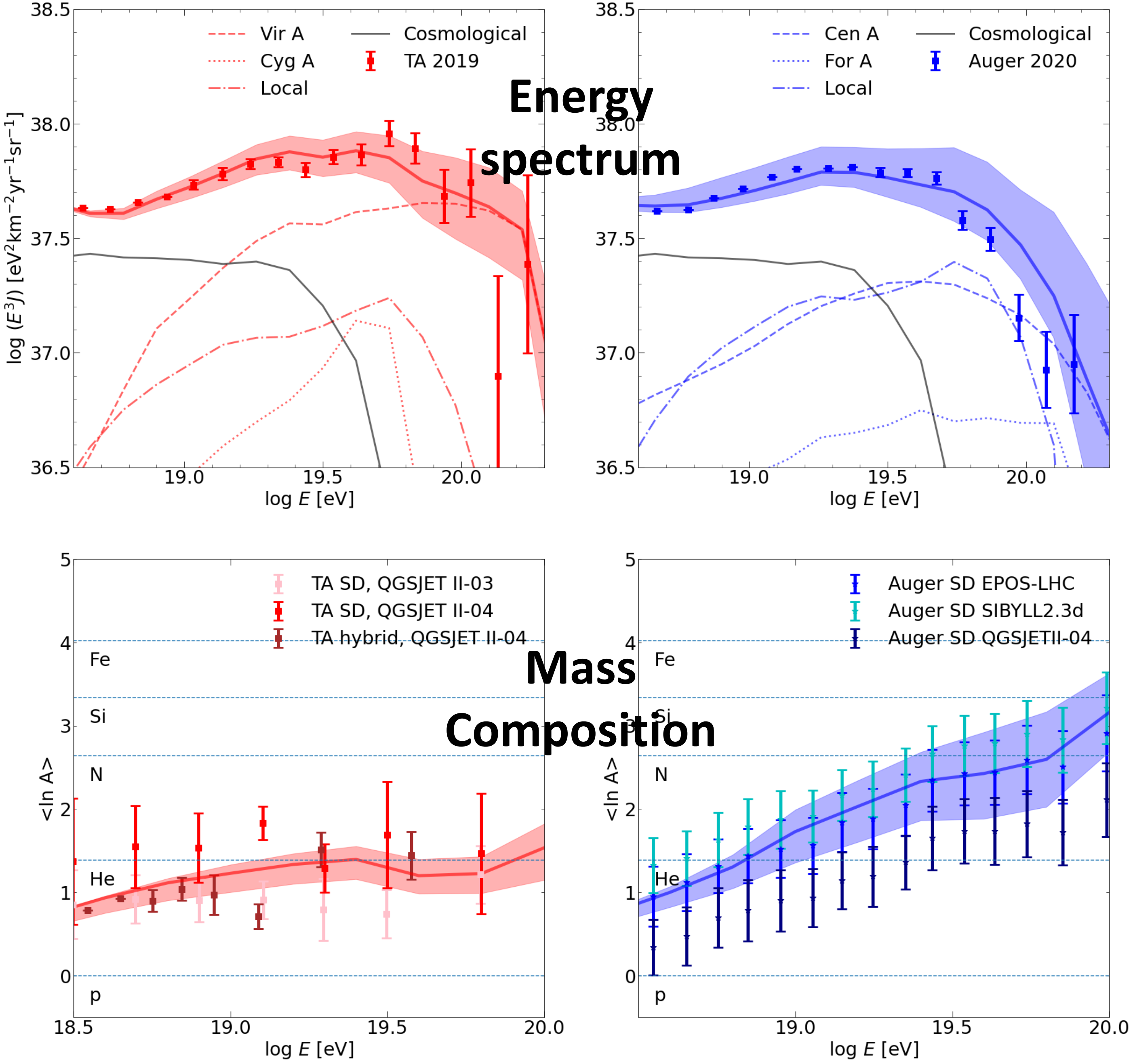

Summary

- The energy spectrum of the UHECRs produced at radio galaxies (RGs) could be modeled as a double power-law with an extended exponential cutoff.
- Relativistic jets generate a higher flux of UHECRs and a lower mass composition at high energy.
- Assuming that Virgo A is a relativistic jet with $\Gamma \sim$ several, it could contribute a substantial fraction of the UHECRs observed at TA.

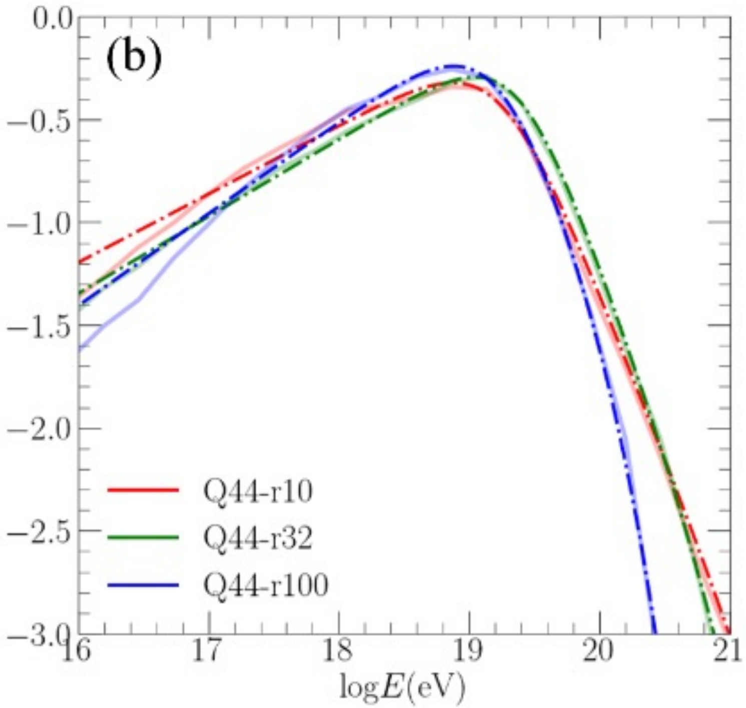

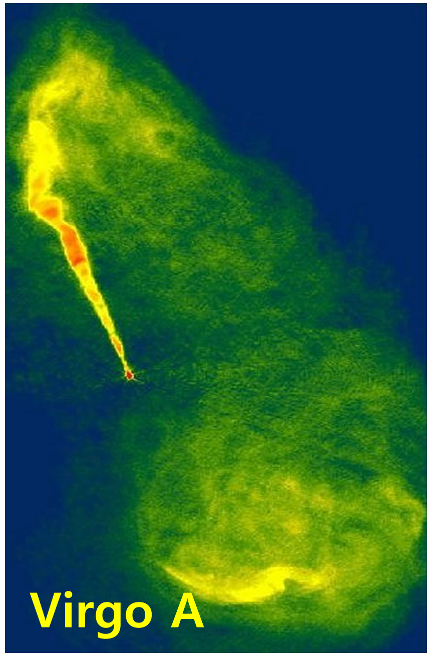

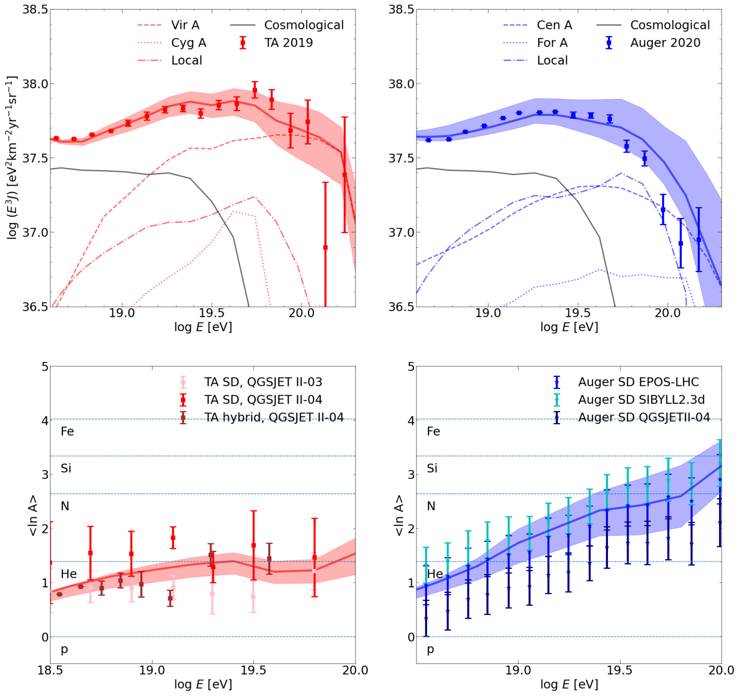

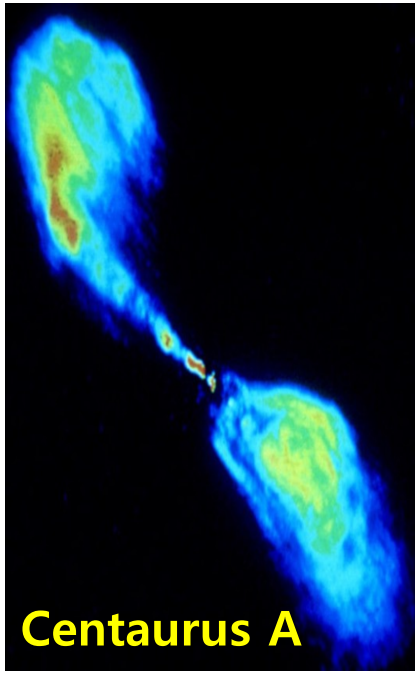

Backup slide

Comparison of double and single power law models for a source at 4 Mpc

Single power-law with exponential cutoff

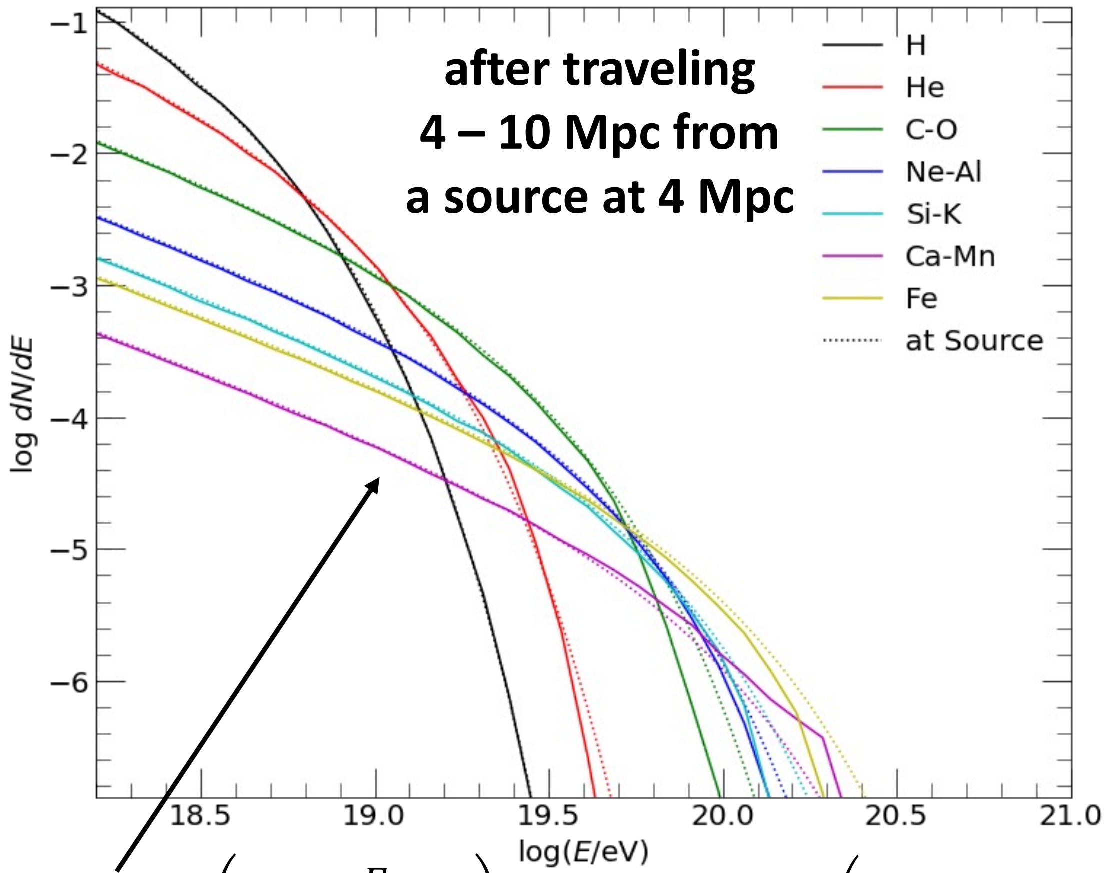

$$\frac{dN}{dE} \propto E^{a} \times \exp\left(-\left(\frac{E}{Z_i E_{Hillas}}\right)\right)$$

$$a = -1$$

Double power-law with extended exponential cutoff

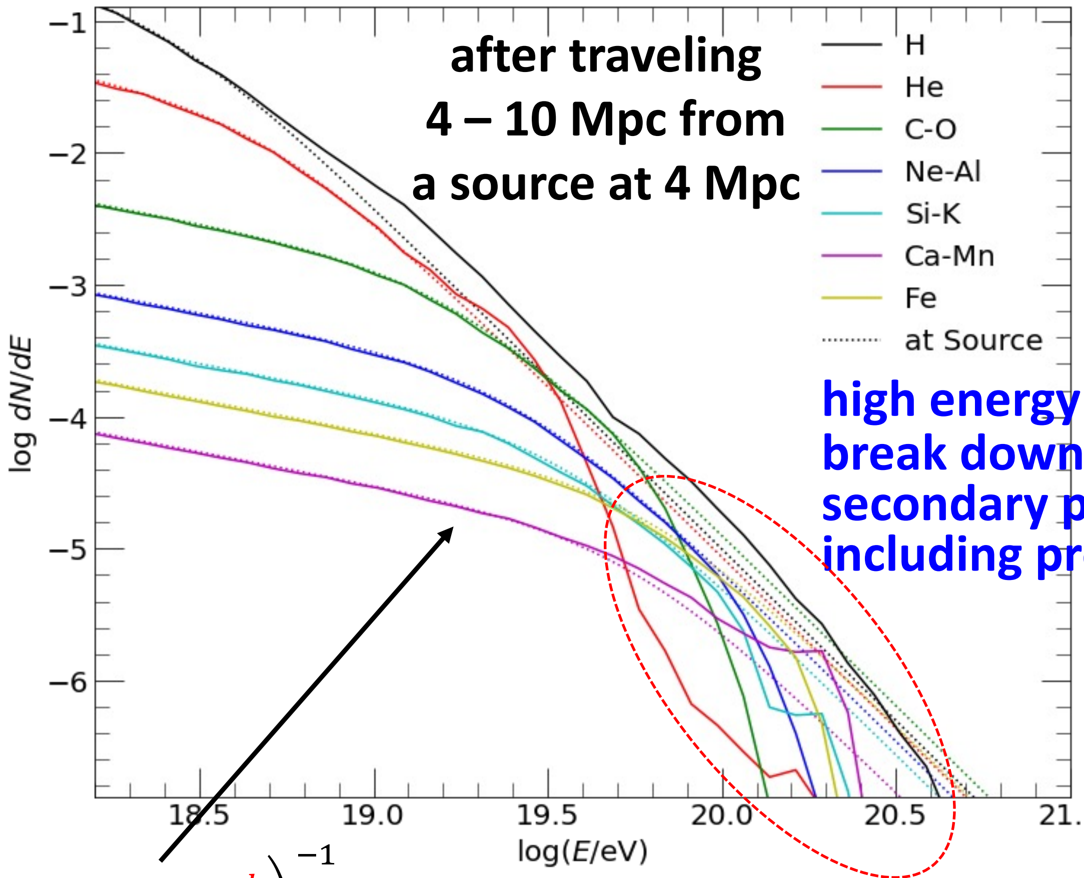

high energy nuclei break down to secondary particles including protons

$$\frac{dN}{dE} \propto \left(\left(\frac{E}{Z_i E_{break}}\right)^{-a} + \left(\frac{E}{Z_i E_{break}}\right)^{-b}\right)^{-1} \times \exp\left(-\frac{E}{Z_i E_{break} \Gamma^2}\right)$$

$$a = -0.5, b = -2.6, \Gamma = 7$$

In the double power-law model,

- **the observed spectrum extends into higher energies**
- **more secondary protons are produced, which in turn reduces <ln A>.**

Comparison of UHECRs coming from Fornax A and Virgo A

Assuming

Formax A → a decollimated jet

Virgo A → a collimated jet

UHECR source spectrum

$$\frac{dN}{dE} \propto \left(\left(\frac{E}{Z_i E_{break}} \right)^{-a} + \left(\frac{E}{Z_i E_{break}} \right)^{-b} \right)^{-1} \times \exp\left(-\frac{E}{Z_i E_{break} \Gamma^2} \right)$$

Fornax A:

$Q_{jet} = 10^{44.2}$ erg/s ,

$a = -0.5, b = -2.6,$ $\Gamma \sim 1.4$

Virgo A:

$Q_{jet} = 10^{43.9}$ erg/s ,

$a = -0.5, b = -2.6,$ $\Gamma \sim 7$

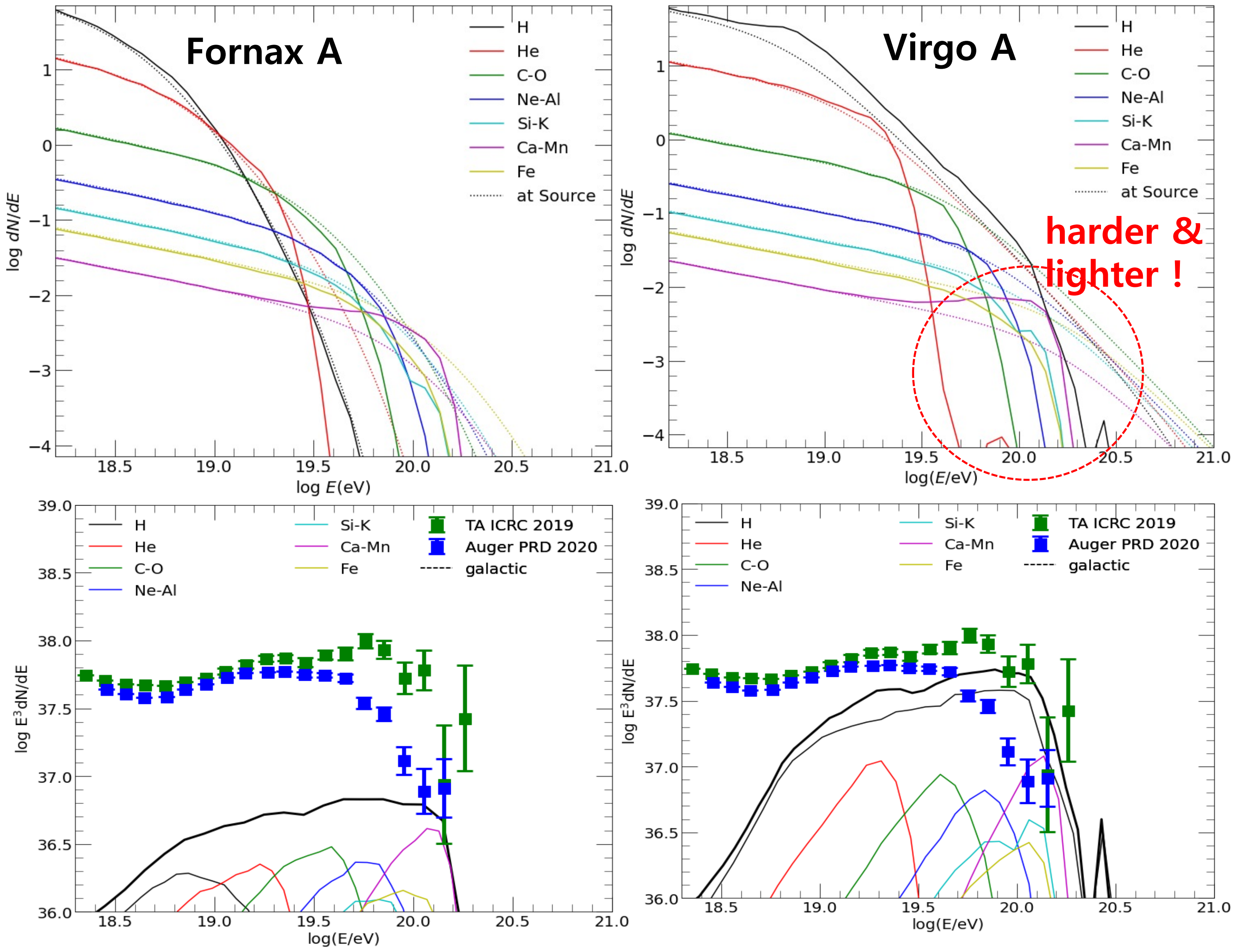

Modeling of observed UHECRs from radio galaxy jets